HIGH THROUGHPUT PROTOTYPING AND MULTISCALE INDENTATION CHARACTERIZATION OF METALLIC ALLOYS

A Dissertation
Presented to
The Academic Faculty

by

Ali Khosravani

In Partial Fulfillment
Of the Requirements for the Degree
Doctor of Philosophy in the
George W. Woodruff School of Mechanical Engineering

Georgia Institute of Technology

May 2019

HIGH THROUGHPUT PROTOTYPING AND MULTISCALE INDENTATION CHARACTERIZATION OF METALLIC ALLOYS

Approved by:

Dr. Surya R. Kalidindi, Advisor
George W. Woodruff School of Mechanical Engineering
Georgia Institute of Technology

Dr. Hamid Garmestani
School of Materials Science and Engineering
Georgia Institute of Technology

Dr. Richard W. Neu
George W. Woodruff School of Mechanical Engineering
Georgia Institute of Technology

Dr. Raja K. Mishra
General Motors Research and Development Center

Dr. Antonia Antoniou
George W. Woodruff School of Mechanical Engineering
Georgia Institute of Technology

Date Approved: Nov 19, 2018

Acknowledgements

First, I would like to express my sincere gratitude to Professor Surya Kalidindi for his support and supervision throughout my PhD study. I also thank my committee members; Prof. Hamid Garmestani, Prof. Richard Neu, Prof. Antoniou Antonia, and Dr. Raja Mishra for providing very helpful feedback and for serving on my thesis committee.

I greatly acknowledge the National Science Foundation (NSF) and National Institute of Standard and Technology (NIST) for supporting this research through Grant No. 1435237 and Grant No. 70NANB14H191 respectively. This research cannot be accomplished without materials support from our collaborators: Dr. Lutz Morsdof at Max Planck Institute, Prof. Cem Tasan at Massachusetts Institute of Technology (MIT), Dr. Douglas Hofmann at NASA Jet Propulsion Laboratory (JPL), Dr. Rene Diaz and Prof. Naresh Thadhani from Materials Science department at Georgia Institute of Technology.

I am very lucky to meet and work with several kind colleagues and true friends during my Ph.D. I wish to thank Dr. Jordan Weaver, Dr. Ahmet Cecen, Ms. Sepideh Parvinian, Mr. Berkay Yucel and many others from whom I learn many.

Words are not enough to convey my deepest gratitude to my family for their unconditional love and support.

Table of Contents

List of Tables

List of Figures

Summary

Accelerating discovery and deployment of advanced material systems requires moving away from traditional sample prototyping, testing methods, and microstructure characterization techniques. In addition, the hierarchical multiscale structure of advanced materials holds the key to improving their performance characteristics. In order to understand and characterize microscale constituents, and length scale effects, novel high throughput approaches are necessary to explore mechanical responses from nano to meso, and macro scale. Several different techniques exist for testing materials at small length scale, including, microtension, micro-pillar compression, micro-bending, and nanoindentation. Among these, spherical nanoindentation is the most efficient and most reliable one. This high throughput mechanical protocol is capable of capturing local mechanical responses at different length scales in polycrystalline metals in the form of indentation stress-strain curves. These responses can then be correlated to local material structure using modern data-driven approaches.

In this work, we are seeking two main goals. First, exploring the viability of high throughput experimental assays for establishing PSP linkages in structural metals, while utilizing small sample volumes and leveraging some of the recent advances described earlier (i.e., spherical microindentation stress-strain protocols and the framework of 2-point statistics). Second, providing detailed insights on mechanical characterization of hierarchical materials and understanding the underlying length scale effects in each constituent phase. For this purpose, the development of the protocols is extended to two advance groups of structural materials with higher levels of microstructural complexity, one represents multiphase polycrystalline group and the other represents composite materials. The multiphase polycrystalline were chosen to be dual-phase (DP steels) where both existing phases, martensite and ferrite, are crystalline but different crystal structures. The composite material is a Ti-based bulk metallic glass matrix composites (BMG-MCs) in which dendrites of a crystalline phase exist in a matrix of amorphous phase. We have selected

these alloys in this dissertation because of their importance to several advanced technologies, owing to their excellent combination of high tensile strength and good ductility.

The work will have a profound impact on speeding up the process of developing new structural materials by reducing the time and energy spent in mechanical characterization at different length scales and establishing PSP linkages.

Chapter 1 Introduction

A great deal of attention in materials innovation is now focused on the accelerated deployment of advanced materials in commercial products [1-6]. An important strategy for realizing this ambitious goal is the development, validation, and adoption of high throughput assays for rapid exploration of the extremely large materials and process design spaces involved. Indeed, significant effort in recent years [7-21] has been aimed at extracting high value (most useful for a selected application) process-structure-property (PSP) linkages [22-34] using a variety of approaches (including multiscale experiments, multiscale models, and data analytics).

1.1. Structural hierarchy in advance materials

Most structural materials have microstructural hierarchy that can be manipulated by undergoing different processing steps to improve their performance in order to be used in advance applications. The term microstructural hierarchy refers to existence of different salient microstructural features at different length scales, starting with arrangements of atoms in each constituent phase, different types of lattice defects, and the arrangements of constituent phases (volume fraction, size, distribution, orientation relationship). A good example of hierarchical microstructure can be seen in dual phase steels known as DP steels (illustrated in the Figure 1.1). The illustration shows levels of structural hierarchy from arrays of atoms in unit cell, the dislocation network formed within lath martensite, different morphology of martensite (laths, blocks) that results in different types of interfaces, and finally a mixture of ferrite and martensite phases at larger length scales. These microstructural features at each length scales are linked to different strengthening mechanisms, hence the design of new alloys for better performance relies on understanding these phenomena by means of multiscale characterization tools.

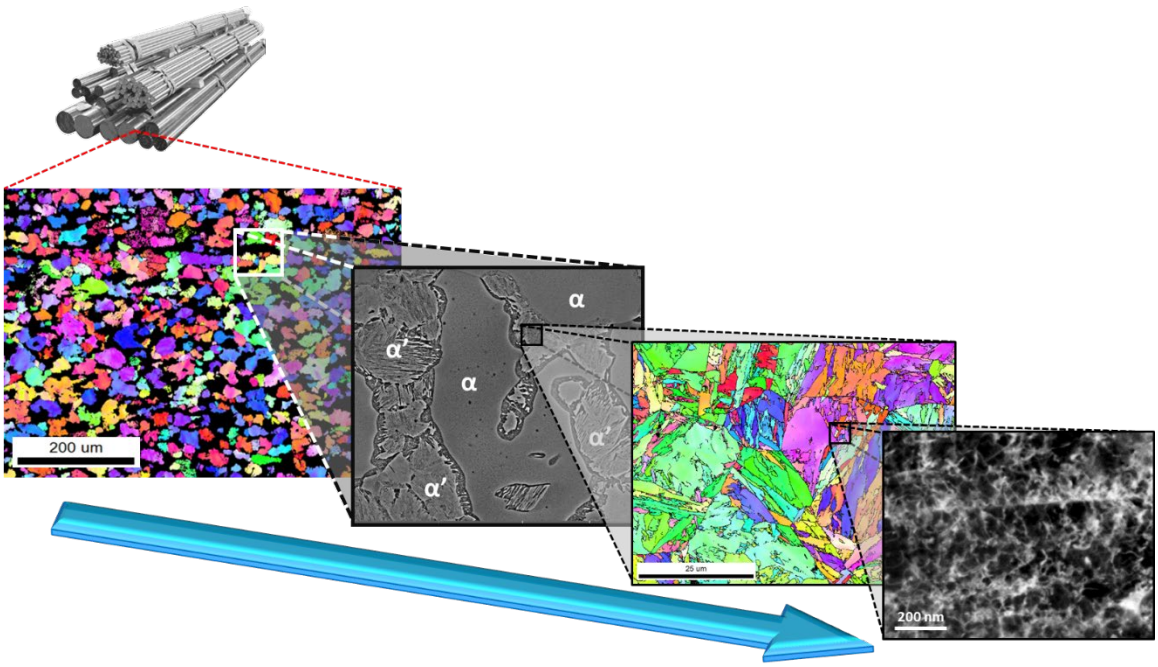

Figure 1.1: Illustration of hierarchical microstructure in dual phase steels

1.2. High throughput mechanical testing characterization

Our focus in this dissertation will be on two related subjects; first on the protocols needed for the accelerated experimental exploration of PSP linkages in multiphase structural metals and alloys, and second on the size-effect investigation using the same protocol at small length scales to study the mechanical responses of the individual microscale constituents present in such multiphase structural metals. The processing histories employed on these materials typically involve a sequence of thermo-mechanical treatments, whereas the main properties (or performance characteristics) of interest are largely related to the plastic response of the material. Since one typically employs standard tensile tests [35] for evaluating the plastic properties of the material, it becomes necessary to make relatively large quantities of material samples with statistically homogeneous microstructures throughout the gage section (of the sample used in the tension test) for each combination of material chemistry and process path studied. This requirement drives up the cost and effort substantially, as is evident from some of the recent innovative efforts in this

direction [12]. In other words, if it were possible to measure reliably the plastic response of the material in very small volumes, it would become possible to reduce dramatically the cost and effort involved in rapid screening of large design spaces in material chemistry and process histories. In addition, it is impossible to standardized tensile tests when the mechanical behavior of individual constituent of a material is of interest. The procedure of sample preparation in the proposed small-scale testing protocols, such as micro pillar testing, not only requires costly advanced tools (which limit the throughput of such measurements) but may also introduce damage to the material during sample preparation.

Indentation has been employed extensively in prior literature [36-52] for evaluating the mechanical response of materials in small volumes. However, the use of this technique has been restricted largely to estimation of modulus and hardness. Only recently, it has been shown that it is possible to extract meaningful indentation stress-strain (ISS) curves directly from spherical indentation through a rigorous set of data analyses protocols. These new protocols have thus far been demonstrated mainly at the very small length scales (indentation zones much smaller than a single grain) [53-60]. There is, however, substantial promise for their application at the meso-length scales (where the indentation zone covers several grains [61]).

1.3. Materials informatics in quantifying the microstructure

Beyond the measurement of mechanical response in small volumes, the next major impediment in extracting PSP linkages in advanced structural metals comes from the lack of a rigorous, yet practical, framework for the statistical quantification of their rich microstructures. Most of the currently employed approaches [38, 45, 47, 48, 51, 62-67] are based on highly simplified measures such as elemental compositions, phase volume fractions, average grain sizes of constituent phases, and the orientation distribution function (ODF). Clearly, the number of distinct microstructures one can reconstruct while meeting specific targets on these measures is extremely large, suggesting that this set of measures is likely to be inadequate for capturing all of the salient features of the microstructure. More formally, one might recognize most of the measures

listed above (except the average grain size) as 1-point statistics of the microstructure in that they do not capture the morphological attributes of the microstructure. Indeed, one can employ the more advanced 2-point statistics (formally called the 2-point spatial correlations) [30, 31, 68-75] to arrive at a more rigorous quantification of the material microstructure. However, most of the prior examples of the application of the framework of 2-point statistics have been limited to multiphase materials, with only a few focused on the application to polycrystalline materials [76-78]. The main difficulty of applying the 2-point statistics measures to polycrystalline samples arises from the very large number of local states present (for example, each distinct grain orientation encountered in the sample needs to be treated as a distinct local state), and the fact that the corresponding number of the distinct 2-point statistics is exceedingly large. In addition to being multiphase and polycrystalline, the microstructures of advanced alloys such as DP steels exhibit grain-scale heterogeneity in the spatial distribution of the dislocation densities (see Figure 1.1). Not surprisingly, a rigorous quantification of these complex microstructures is not readily accomplished with the currently available toolsets. Clearly, one needs to make suitable simplifications in order to establish practically useful PSP linkages for advanced structural metal alloys.

In this work, we are seeking two main goals. First, exploring the viability of high throughput experimental assays for establishing PSP linkages in structural metals, while utilizing small sample volumes and leveraging some of the recent advances described earlier (i.e., spherical microindentation stress-strain protocols and the framework of 2-point statistics). Second, providing detailed insights on mechanical characterization of hierarchical materials and understanding the underlying length scale effects in each constituent phase.

In this dissertation the development of the protocols is extended to two advance groups of structural materials with higher levels of microstructural complexity, one represents multiphase polycrystalline group and the other represents composite materials. The multiphase polycrystalline were chosen to be dual-phase (DP steels) where both existing phases, martensite and ferrite, are crystalline but different crystal structures. The composite material is a Ti-based bulk metallic glass

matrix composites (BMG-MCs) in which dendrites of a crystalline phase exist in a matrix of amorphous phase. We have selected these alloys in this dissertation because of their importance to several advanced technologies, owing to their excellent combination of high tensile strength and good ductility.

Chapter 2 covers the background details on spherical indentation stress-strain analysis protocols as a high throughput mechanical characterization technique at different length scales. The Chapter 3 focuses on the microstructure characterization using 2-point statistics and establishing PSP linkages.

Chapter 4 and 5 make following advances in multi length-scale property measurements and high throughput PSP linkages by demonstration of their utilities on DP-steel and Ti-based BMG-MCs for the first time from experimentation. Each chapter contains two sub-section. In the Section 4.1, the lath martensite is studied systematically at different length scales using spherical nanoindentation stress-strain protocols and conventional tensile testing protocol. These were used to measure the contribution of lath interfaces and internal C content on mechanical response of lath martensite. In the Section 4.2, the microindentation protocols were developed to capture mechanical bulk response in dual phase steel where both ferrite and martensite exist in the microstructure. Nine different processing paths are selected to produce different microstructures. The linkages for processing-structure-property were then established using data science approaches after the corresponding indentation microstructures were quantified by 2-point statistics. In the Section 5.3, spherical nanoindentation stress-strain protocols are utilized to capture mechanical responses of individual constituents (amorphous and crystalline) in four Ti-based bulk metallic glass matrix composites (BMG-MCs). In addition, the measurements have extended to microindentation stress-strain analysis to capture bulk property in these four Ti-BMG-MCs where different amount of amorphous phase exists in the microstructure. Since the deformation mechanisms in amorphous phase are entirely distinct from the one in crystalline materials in absence of long range atomic orders, the more focus will be on mechanical responses of the

amorphous phase from nanoindentation tests. In the Section 5.4, the microstructures of all these alloys are quantified by 2-point statistics, and then processing-structure-property linkages in these alloys are established from the microstructure quantification technique and the collected microindentation properties from previous section.

Finally, the main conclusions from this dissertation and the possible future work are presented in Chapter 6.

Chapter 2 Multi-length scale and high throughput mechanical characterization

As mentioned in previous chapter, most of structural materials have hierarchical microstructure. These structural materials are rarely made of a single phase to achieve a good combination of desired properties. It is very common to select a combination of manufacturing processes that results in a secondary phase (or more) in the material microstructure to increase both strength and toughness. Identifying how the processing parameters influence the overall bulk as well as each individual constituent's properties remains the main question in the material science. This requires different mechanical characterization methods capable of testing materials at different length scale.

Given the rich heterogeneity of material structure at smaller length scales (microns and sub-micron), it is only natural that a larger number of mechanical measurements are needed to fully capture the natural variance in these measurements. This is because the material microstructure is inherently heterogeneous (with variations in local features such as phase/precipitate size and shape, grain orientations, grain/phase boundaries, dislocation densities). Therefore, it is essential to develop assays that allow sampling of a large number of mechanical responses in advanced materials at the lower length scales within reasonable effort and cost. Only then, it would be feasible to confidently assess the mechanical responses of the material at hierarchical length scales, and explore systematically the underlying length-scale dependent correlations in these measurements.

The currently employed characterization protocols have limitations in mechanical testing of very small volumes (submicron). First, many of the sample preparation techniques introduce some form of surface damage [79-88]. Since it is often difficult to correct the measurements for the presence of the damaged surface layer, the reliable extraction of intrinsic material properties from these tests becomes a significant challenge. Second, there is a strong interest in estimating the properties of the individual microscale constituents present in the microstructure. Since these constituents (e.g., single phase/grain regions) can be as small as few nanometers and they may

exhibit irregular shapes, it is not easy to produce samples with standardized geometries that allow an estimation of their individual properties using already established analyses protocols.

Recent advances in instrumented indentation offer a promising avenue for addressing many of the limitations described above. Taking advantage of the impressive resolutions of modern nanoindenters in measuring load, displacement, and stiffness, our research group has developed and demonstrated novel protocols [57, 89] that are capable of extracting meaningful spherical indentation stress-strain curves by tracking the local mechanical response from the linear elastic regime to the elastic-plastic regime with small amounts of plastic strain. These protocols have been validated on a broad variety of materials systems and length scales ranging from about 50 nm to about 500 μm to study the contributions of the local deformation [58, 59, 90, 91], the composition [92], and crystal orientations [56, 58-60, 91, 93] on the local mechanical properties. The measurements at the bigger length scales were performed in an instrumented microindenter with customized test protocols [94, 95]. In addition to recovering the mechanical responses in the form of meaningful indentation stress-strain curves, protocols have also been developed to extract intrinsic material properties from these stress-strain curves [96-98].

2.1. Indentation testing

Among various methods exist in mechanical testing at the macro and nanoscale, nanoindentation and micropillar testing are the most common ones. However, the micropillar testing has its own disadvantages. First, it requires highly sophisticated facilities (e.g. FIB and etching) that make this method not a time and cost effective protocol. Second, it has been reported several times that these preparation techniques either are not applicable to all material or they introduce some damage to the material during fabrication and as a result alters the materials mechanical responses. On the other hand, nanoindentation becomes more attractive due to simple equipment and sample preparation procedures.

Even though, indentation method has been utilized for about a century [99], the recent advances in instrumentation and analysis have turned it into a high throughput method and hence become very attractive to multi-scale measurements. Additionally, In contrast with traditional mechanical testing methods (e.g. tensile, compression) where large quantities of a materials need to be prepared and processed in order to obtain few mechanical data points, the indentation testing can provide results from a small volume of a material and therefore several tests can be performed easily on a small single sample. Compared with other testing methods, the sample preparation for indentation test is the same as conventional metallography procedures. In other words, once a sample is ready for microstructure characterization, no extra effort is required to obtain indentation results. An example of time and cost effectiveness in using high throughput protocol can be found in [100] summarized in the Figure 2.1 where aging process of aluminum 6061 was studied using both conventional tensile and high throughput (microindentation in conjunction with a sample library) testing protocols. For conventional method, 3 different aging temperatures were chosen and after sample preparation and heat treatment, 3 tensile tests were performed in accordance with ASTM Standard E8-13a [101]. In the high throughput method, a single bar was heat treated such that a gradient of temperature is applied along its length. This way, a sample library was produced and its mechanical properties were obtain using microindentation on the middle section after polishing. For the purpose of comparison, the time spent in each method were recorded starting from as-received material. Both methods show very similar results, however, because of the thermal gradient applied on the sample in the high throughput method, we were able to investigate 28 aging temperatures by the microindenter in a single sample. The comparison between two protocols shows that the high throughput method is more efficient compared with the conventional method. (Approximately 7.5 times faster and 13 times less cost).

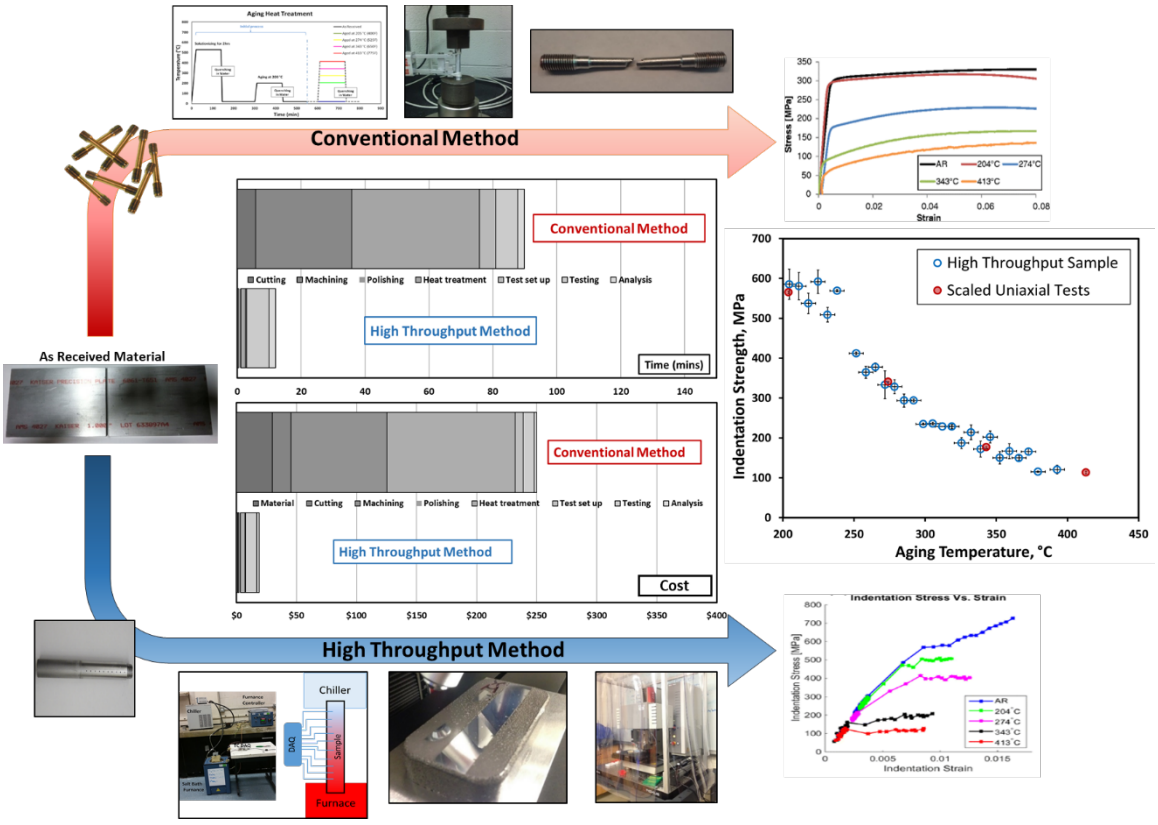

Figure 2.1: Time and money saving by utilizing high throughput techniques

2.2. Nanoindentation testing protocols

As was mentioned earlier, a large area on the sample can quickly be prepared using standard metallography procedure and that provides large enough surface to conduct many indentation tests depending on the tip size and geometry. There exist several types of tip geometries in testing protocol: spherical, three-sided pyramid (Berkovich), wedge, cube corner, four-sided pyramids (Vickers), etc. Among these tip geometries, only spherical tip is capable of providing elastic and elastic- plastic transition and plastic responses of the studied materials (this will be expanded ion next section). Using other geometries, the tested materials start deforming even at small indentation depth and load because of high stress concentration at the sharp indenter's tip (see Figure 2.2). The other differences in the sharp tip protocols related to the analysis. Most of these protocols reporting hardness as a measure of material resistant to deformation at large strains

where the hardness value is calculated as a normalized maximum load in indentation by the indentation impression area measured after the load is removed. This measured hardness value is a single point as an effective stress and very sensitive to the indenter shape, size, and the imposed load level which make the hardness data a comparative measure of material strength . In modern instrument, the indentation device is equipped with continuous stiffness measurements (CSM) that eliminates the necessity of unloading in order to measure elastic modulus and hardness. Nevertheless, only spherical tip in new indentation instrument is capable of capturing property information of the virgin material (without plastic deformation).

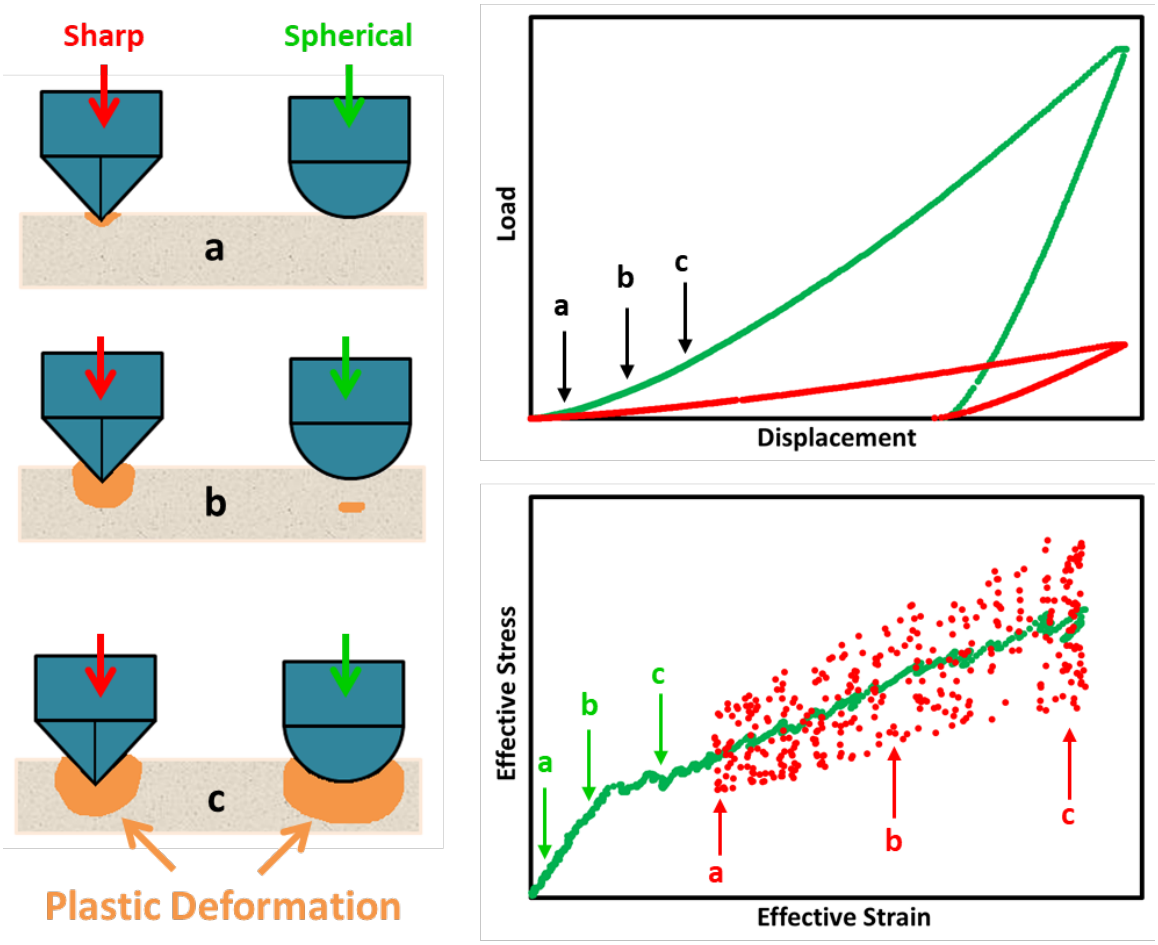

Figure 2.2: Schematic of comparison between sharp and spherical indentation. The indentation load-displacement responses for both and their corresponding effective stress-effective strain

2.3. Indentation Stress-Strain analysis protocols

Despite all advantages of indentation, the analysis of the data is not a trivial task because of a highly heterogeneous stress field (as oppose to uniaxial stress state in micropillar testing) exists under the indenter. Many efforts have been made to calculate an effective stress in indentation testing by normalizing the applied load on the area of the indentation. In following some of these approaches are summarized.

The first standardized hardness test was proposed by J. A. Brinell in 1900 [99]. It uses a hard ball as an indenter and the applied load changes from a weight of 0.5 or 3000 kg. The indentation is applied on a standard time (30 seconds) and then the Brinell hardness (BHN) are expressed as the load (P) divided by the surface area of the indentation as:

$$BHN = \frac{P}{\left(\pi \frac{D}{2}\right)\sqrt{(D - D^2 - d^2)}} \tag{2.1}$$

where D, d, and t are diameter of the ball, diameter of the indentation, and the depth of the impression in millimeter respectively. Meyer [102] suggested that the mean pressure between indenter and ample surface is equal to the applied load to the projected area of the indentation. And this mean pressure is referred to as the Meyer hardness:

$$Meyer\ Hardness = \frac{Load}{Projected\ area\ of\ indentation} = \frac{4 \times P}{\pi d^2} \tag{2.2}$$

There exist other protocols for indenters with pyramidal geometries. Vickers and Knoop protocols use a square-base diamond pyramid and are defined by the applied load divided by the surface area of the indentation. In practice, a microscope is used to measure the lengths of the diagonals of the indentation and then, the Vickers hardness number (VHN) is expressed as:

$$VHN = \frac{2P \sin\left(\theta/2\right)}{L^2} = \frac{1.854P}{L^2} \tag{2.3}$$

where θ and L are the angle between faces of the diamond (136° for Vickers indenter) and average length of measured diagonals (mm) respectively. As one may notice all these protocols depend

heavily on personal experience in measuring indentation impression using a microscope. To overcome this issue, Rockwell hardness was introduced which uses indenter depth under a constant load as a measure of hardness. Applying an initial load of 10 kg followed by the additional load minimized the effect of surface quality in the Rockwell hardness testing. The penetration of the indenter when the second load is applied is taken as a measure of hardness. Nevertheless, in this protocol the measured hardness value is still depends on the applied load. One reason for this effect is related to the hardening process of the materials under the indenter as a result of plastic deformation.

2.3.1. Tabor's ISS protocol

To eliminate applied load and indentation depth effect, Tabor suggested running spherical indentation at different load levels and plot all together [103]. He selected copper and steel that have different hardening rates and utilized the Meyer protocol in hardness measurements. Then he plotted the measured hardness values respect to a non-dimensional parameter of $\frac{d}{D}$ where d and D are the diameter of the indentation impression and the indenter respectively. The resultant curve from this approach is very similar to the stress-strain curves from uniaxial test. Then Tabor performed uniaxial compression tests on the same materials and showed a very good agreement between indentation hardness plot and the uniaxial curve by applying scaling factors of 2.8 and 0.2 on uniaxial true stress and uniaxial true strain respectively.

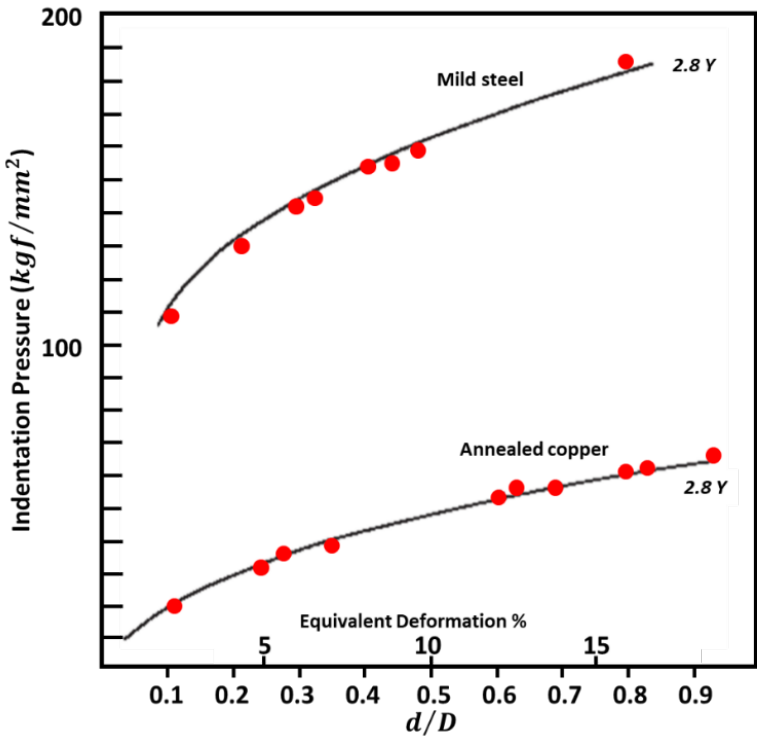

Figure 2.3: Tabor's plot showing the changes of indentation pressure with the ratio d/D for mild steel and copper as red points. The solid curves are scaled uniaxial compression results.

2.3.2. Field and Swain's ISS protocol

One may notice that Tabor's approached requires conducting multiple indentation tests at different depths and locations in order to build an indentation curves. In addition, Meyer's protocol is used to calculate the indentation hardness by measuring the residual indentation impression which highly depends on personal experience. With advances in instrumentation, continuous recording of load and displacement values become possible with high accuracy and therefore a different analysis method is needed. Field and Swain [104, 105] developed a protocol that contains multiple unloads to 50% of maximum load and uses Hertz Theory [106] to analyze the unloading segments. Hertz theory [106] provides the relationship between the indentation load (P) and the elastic indentation depth (h_e) based on the effective modulus (E_{eff}) and the effective radius (R_{eff}).

The theory was defined for contact between two isotropic, elastic, frictionless contact of axisymmetric surfaces as:

$$P = \frac{4}{3} E_{eff} \sqrt{R_{eff} h_e^3} \tag{2.4}$$

$$\frac{1}{E_{eff}} = \frac{1 - v_i^2}{E_i} + \frac{1 - v_s^2}{E_s} \tag{2.5}$$

$$\frac{1}{R_{eff}} = \frac{1}{R_i} + \frac{1}{R_s} \tag{2.6}$$

$$a = \sqrt{R_{eff} h_e} \tag{2.7}$$

E_i , v_i and E_s , v_s are Young's modulus and Poisson ratio for the indenter and the sample, respectively. The a is the contact radius at each level of indentation using which Field and Swain define the indentation stress and the indentation strain as it was defined by Tabor:

$$\sigma_{ind} = P/\pi a^2 \tag{2.8}$$

$$\varepsilon_{ind} = a/R_i = d/D \tag{2.9}$$

As it was mentioned, several unloading is needed to complete an indentation stress-strain curve. In new instrumentation with CSM (continuous stiffness measurement) a small oscillatory signal (many unloads) is superimposed on the monotonic loading sequence. With this new technology, Oliver and Pharr [107, 108] defined a similar contact radius as Field and Swain as:

$$a = \sqrt{R h_c - h_c^2} \tag{2.10}$$

where h_c is the contact depth determined from the unloading stiffness, S:

$$h_c = h - \frac{3}{4} \frac{P}{S} \tag{2.11}$$

The contact radius a from both Equations (2.7) and (2.10) are the same in the elastic regime. Once plasticity occurs, these two equations yield to different values. Similar approaches were taken by Basu [109] and Herbert [110] in which CSM measurements were used instead of

partial unloading. All these approaches also using similar definition for indentation stress and indentation strain as indicated in Equations (2.8) and (2.9) respectively.

2.3.3. Kalidindi and Pathak's ISS protocol

In the previous indentation stress-strain analysis protocols the obtained indentation curves elastic regimes is not very clean and a high amount of noise exists at the beginning of the curve mainly because of an error in surface detection in current devices (see Figure 2.4). In non-CSM devices, the surface detection is done by the changes in the slope of load-displacement data. In CSM machine, various signals are checked for finding the first contact including, the harmonic contact stiffness (S; the same as the elastic stiffness defined earlier), the harmonic load, the harmonic displacement and the phase angle. The one that shows an abrupt change upon initial surface touch is used as the surface detection criteria. Finding the initial contact is very crucial in estimating contact radius that later is used to calculate indentation stress and indentation strain (Equation (2.8 and (**2.9**)

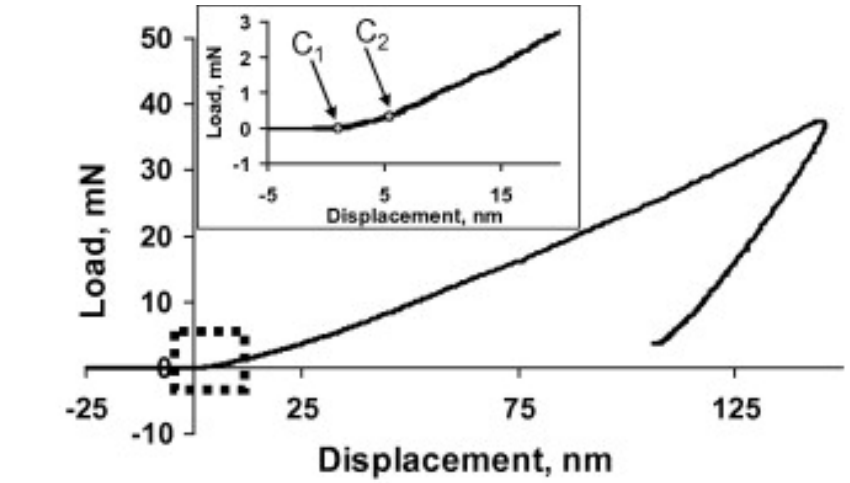

(a) Load-displacement curve for tungsten.

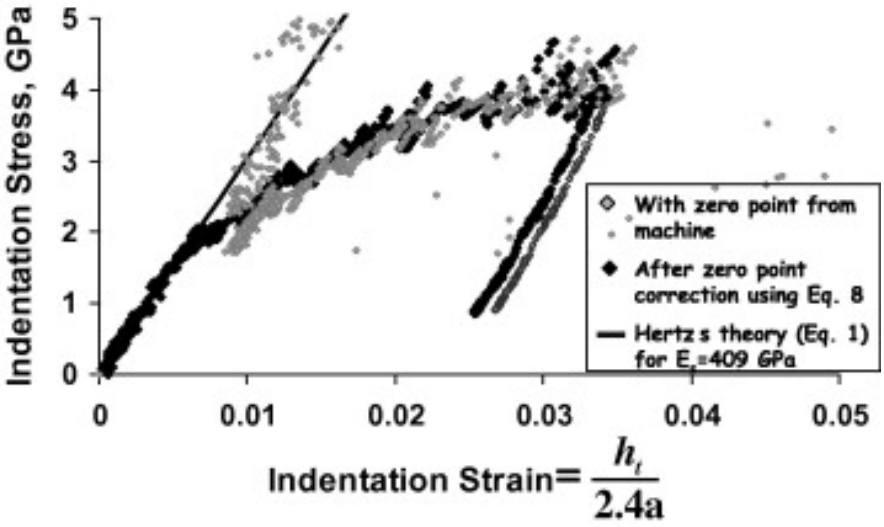

(b) Indentation stress-strain curve for tungsten.

Figure 2.4: The measured load–displacement curve (a) is shown from a tungsten sample. The corresponding indentation stress–strain curves (b) are extracted for the case when the zero-point established by the machine (C1) and when the effective zero-point (C2) are determined using Kalidindi and Pathak's protocol. In the first analysis, an unexplainable spike appears in the initial elastic loading portion of the curve while the new method results in a much better indentation stress–strain curve.

In Kalidindi and Pathak's ISS protocol [89] the analysis contains two steps. First step is accurately finding the effective point of the initial contact (zero-point correction) which is crucial

in order to deal with any artifacts at the initial contact caused by imperfections in indenter shape or unavoidable surface conditions such as oxide layer and roughness. The second step is extracting indentation stress-strain curves from the corrected data using new definition for indentation stress, σ_{ind}, and indentation strain, ε_{ind}.

In the first step, the initial contact point (zero point) is determined by finding load and displacement corrections ($P^* \; and \; h^*$) from this equation:

$$S = \frac{3P}{2h_e} = \frac{3}{2}\frac{(\tilde{P} - P^*)}{(\tilde{h} - h^*)} \tag{2.12}$$

where S is the elastic unloading stiffness from the CSM, $\tilde{P}$ and $\tilde{h}$ are the load and displacement from the machine zeroed data. To find values of $P^* \; and \; h^*$, Equation (2.12) is rearranged to the following format and then and solved by linear regression between $\tilde{P} - \frac{2}{3}S\tilde{h}_e$ and S. Examples of the linear regression analysis to identify the correction values from spherical indentation on a pure aluminum and a pure titanium samples are shown in Figure 2.5:

$$\tilde{P} - \frac{2}{3}S\tilde{h}_e = -\frac{2}{3}h^*S + P^* \tag{2.13}$$

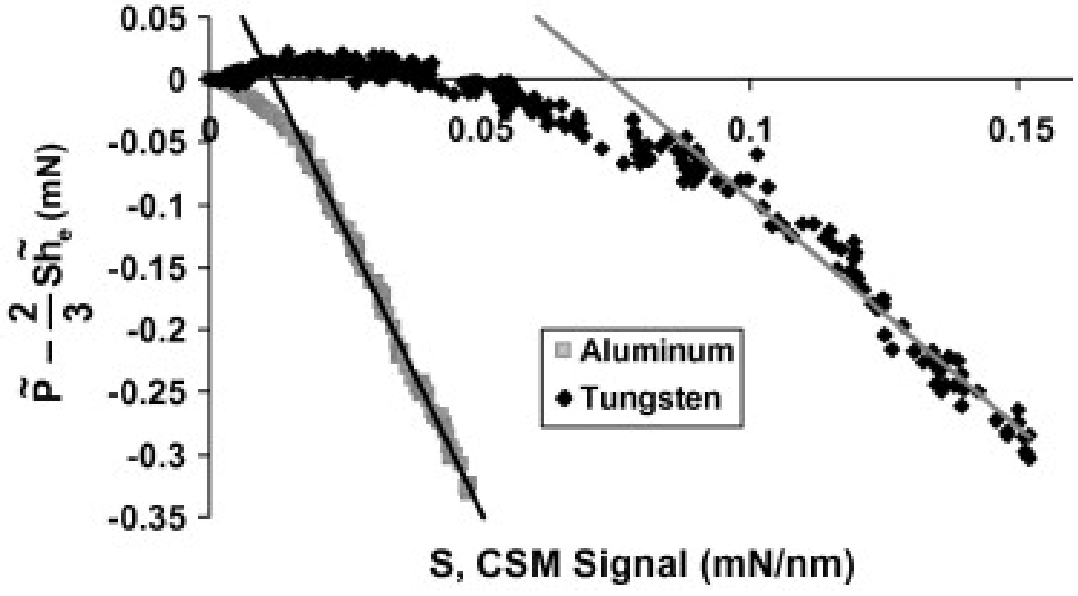

Figure 2.5: The identification of the effective zero-point by using linear regression between $\tilde{P} - \frac{2}{3}S\tilde{h}_e$ and S that make the data consistent with Hertz's theory [89].

Once the correction values of $P^* \; and \; h^*$ are found, the effective modulus can be determined by a linear regression of Equation (2.13) between P and $h^{3/2}$. Please notice that the Equation (2.4) is valid for the initial elastic loading data where the total displacement,h, is equal to elastic displacement, h_e. In addition, the effective radius in Equation (2.6) is the tip radius since the sample surface is flat at the initial contact.

$$R_{eff} = R_i \tag{2.14}$$

$$P = \tilde{P} - P^* \tag{2.15}$$

$$h = h_e = \tilde{h} - h^* \tag{2.16}$$

After plasticity occurs the total displacement is the summation of elastic and residual displacements defined as:

$$h = h_e + h_r = \left[\frac{3}{4}\frac{1}{E_{eff}}\frac{1}{\sqrt{R_{eff}}}\right]^{\frac{2}{3}} p^{\frac{2}{3}} + h_r \tag{2.17}$$

Also R_{eff} needs to be determined since the sample surface is no longer flat. The contact radius (a) at any point still can be calculated using Hertz's equations by analyzing the unloading stiffness from CSM measurements as:

$$a = \frac{S}{2E_{eff}} \tag{2.18}$$

Both harmonic contact stiffness, S, and the contact area radius, a, evolve continuously with increasing indentation load/depth. But the effective modulus which was measured from initial elastic loading remains constant. With accurate estimation of contact area radius, Kalidindi and Pathak [89] then adopted a new definition of the indentation strain and indentation stress as:

$$\varepsilon_{ind} = \frac{4}{3\pi}\frac{h}{a} \approx \frac{h}{2.4\,a} \tag{2.19}$$

In their work, using the finite element simulations, they showed that the size of the indentation zone approximately extends to a depth of about $2.4a$ with a span of $2a$. This provides more physical meaning to the new definition of indentation strain as equivalent to compressing a

cylinder with a diameter of $2a$ and a height of $2.4a$ (as an initial length) by total indentation depth,h_t (as of change in height). With this definition the Hertz's equations can be re-cast as:

$$\sigma_{ind} = E_{eff}\varepsilon_{ind} \quad \textbf{(2.20)}$$

$$\sigma_{ind} = \frac{P}{\pi a^2} \quad \textbf{(2.21)}$$

$$\varepsilon_{ind} = \frac{h}{2.4\ a} \quad \textbf{(2.22)}$$

Following this new indentation analysis in finding zero-point correction and using new definition of indentation stress and indentation strain, the analyzed results in a very reasonable looking indentation stress–strain curve shown in Figure 2.6. As one can see in this figure, the indentation elastic modulus, the indentation yield strength, and the indentation work hardening rate can be extracted from each measured indentation stress-strain curve. To determine the indentation yield strength, a small offset is required to find the initial flow stress insensitive form testing parameters. Similar to uniaxial testing protocol, a 0.002 plastic strain offset was employed to identify the indentation yield strength. This small offset is very useful eliminating uncertainties defining the initial flow stress in indentation stress-strain curves with absent of pop-ins. In the case of existing pop-in on indentation stress-strain curve, a different approach is used which will be explain in next sections. The indentation work hardening rate was extracted by fitting a line to the indentation stress-strain plot from the indentation yield point up to different indentation plastic strains.

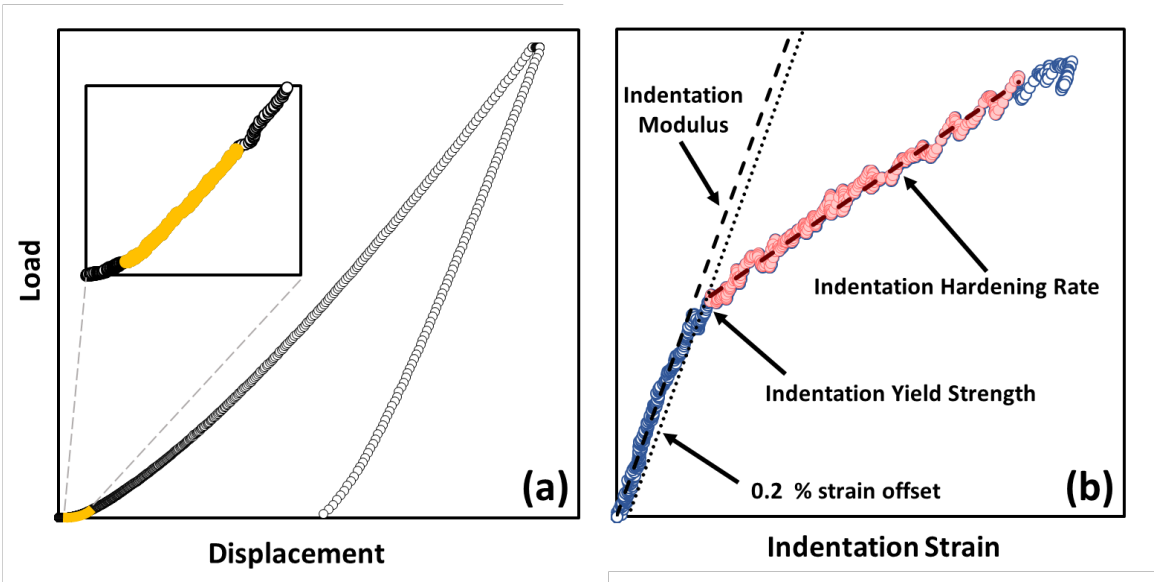

Figure 2.6: schematic example of indentation stress-strain curve from new analysis protocol

2.3.3.1 Indentation pop-in

In load control indentation tests, a feature called pop-in event occurs in loading. This phenomenon is an increase in penetration depth without any major increase (a sudden jump in displacement) in the applied indentation load. Pop-in phenomena has been studies in numerous studies: in well-annealed and large grains in the absence of dislocation source in the primary indentation zone (incipient pop-ins) [91, 111-113], at the vicinity of grain boundaries (GBs) where dislocations can be absorbed, transmitted or nucleated when there is a GB/interface exists in the primary indentation zone (GB pop-ins) [113-119], in the materials that show TRIP [120-122] and TWIP [123, 124] effects during which phase transformation or change in crystal orientation occurs in the primary indentation zone, in amorphous materials where localized deformation happens by forming shear bands [125-127] or severe deformation leads crack formation in low-symmetry crystals [128, 129]. An example of incipient pop-in events is presented in the Figure 2.7 showing two tests collected from the same grain orientation in a pure titanium sample. The green plot is the test after vibro-polishing and the black one is the same sample after electro-polishing. This example shows that incipient pop-in events can be suppressed by introducing very small deformed layer as

a result of mechanical polishing. The stress level that can be reached before an incipient pop-in has been estimated to be the theoretical limit of the material ($G/2\pi$, where G is the shear modulus) [130-136]. In these studies, also it has been reported that no pop-ins or small pop-ins are observed when larger indentation tip is used. This corresponds to higher chance of existence of dislocation/dislocation source in the primary indentation zone. The incipient pop-ins are very large that can be detected easily on the load-displacement curves (10-100nm displacement burst). As one can see, the stress-strain plots for both tests become very similar after the pop-in.

Other types of pop-ins have different mechanisms of formation. For example, grain boundary pop-in is observed in indentation tests conducted in vicinity of grain boundaries [113-119]. It is generally believed that these are caused by the pile-up of the dislocations produced in the primary indentation zone at the grain boundaries and their eventual transmission through the grain boundary. The characteristic of this type of pop-ins are much smaller displacement burst as well as stress required to activate a pop-ins.

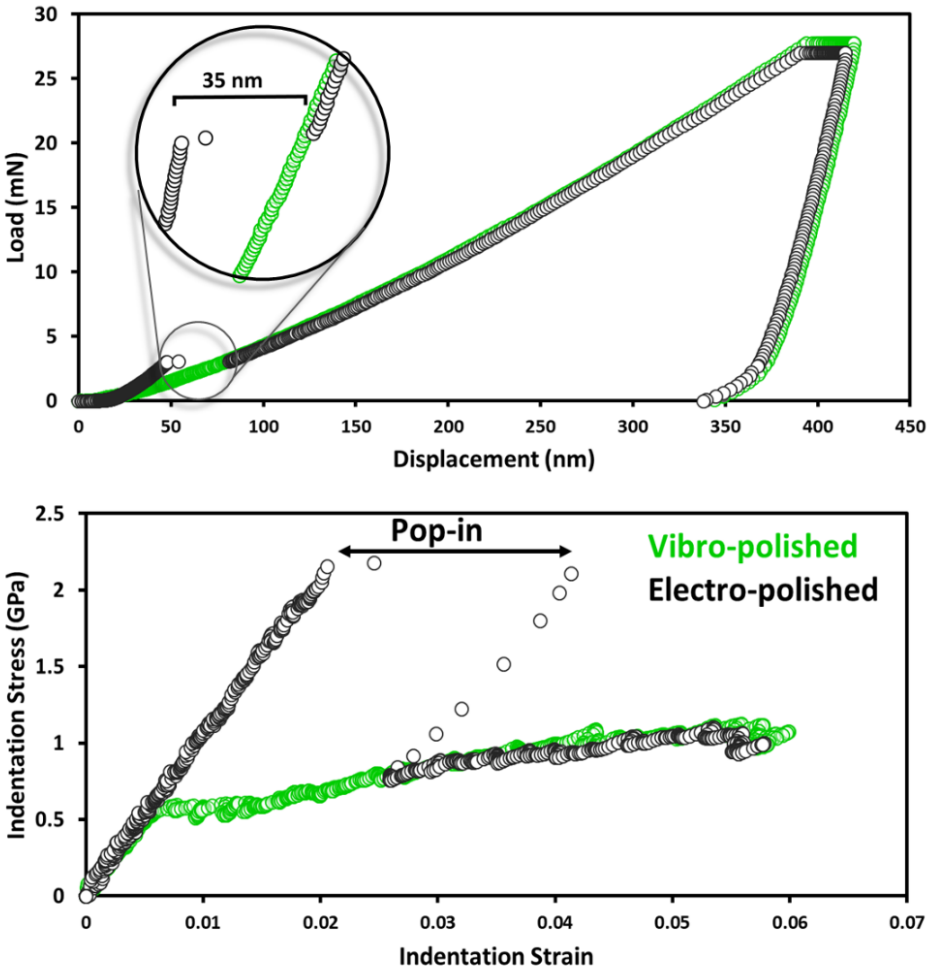

Figure 2.7: Pop-in events when a Ti sample is fully annealed vs some damage introduced to the surface during polishing

2.3.3.2 Size effect in ISS protocol

Large number of studies are investigating size effect phenomena observed in indentation testing. In most them higher hardness measurement at smaller indentation depth [137] or smaller (sharper) indenter tip [138, 139] is reported. The higher hardness values from shallow indentation have been related to a higher number of geometrically necessary dislocations (GNDs) because of large strain gradient under the indenter tip [137, 140]. Main sources for the observed high hardness values at small indentation depth have been reported to be related to the testing protocol and the

sample surface quality from polishing preparation which result in errors in estimation of contact area and the point of initial contact [139].

Using Kalidindi and Pathak's indentation stress strain analysis protocol, no size effect was observed for indentation yield strength. In this protocol, in case of occurrence of pop-in, back extrapolation of the post pop-in indentation stress-strain data is used to define indentation yield strength. Number of studies using indenter tip radius from range of 10-100 μm verify the accuracy of the back-extrapolation method [55, 58, 60, 92, 141, 142]. An example of using back extrapolation on post pop-in method is illustrated Figure 2.8. The figure shows two spherical indentation stress strain curves obtained from different tip radii, 100 μm (blue plot) and 16 μm (red plot) on a pure Ti sample. Tests were conducted on the same grain (same crystallographic orientation). As can be seen, smaller indenter tip results in a pop-in on the plot. To determine the indentation yield strength, a 0.2% strain offset is used on the indentation curve obtained with 100μm tip radius (Figure 2.8 (a)). In the case of 16 μm tip radius, the indentation yield strength for the test was determined from back extrapolating the post pop-in ISS data to a 0.2% strain offset (Figure 2.8 (b)). Using this method, the back extrapolated yield strength and a 0.2% offset yield strength form tests with and without pop-in, respectively, are very similar (Figure 2.8 (c)).

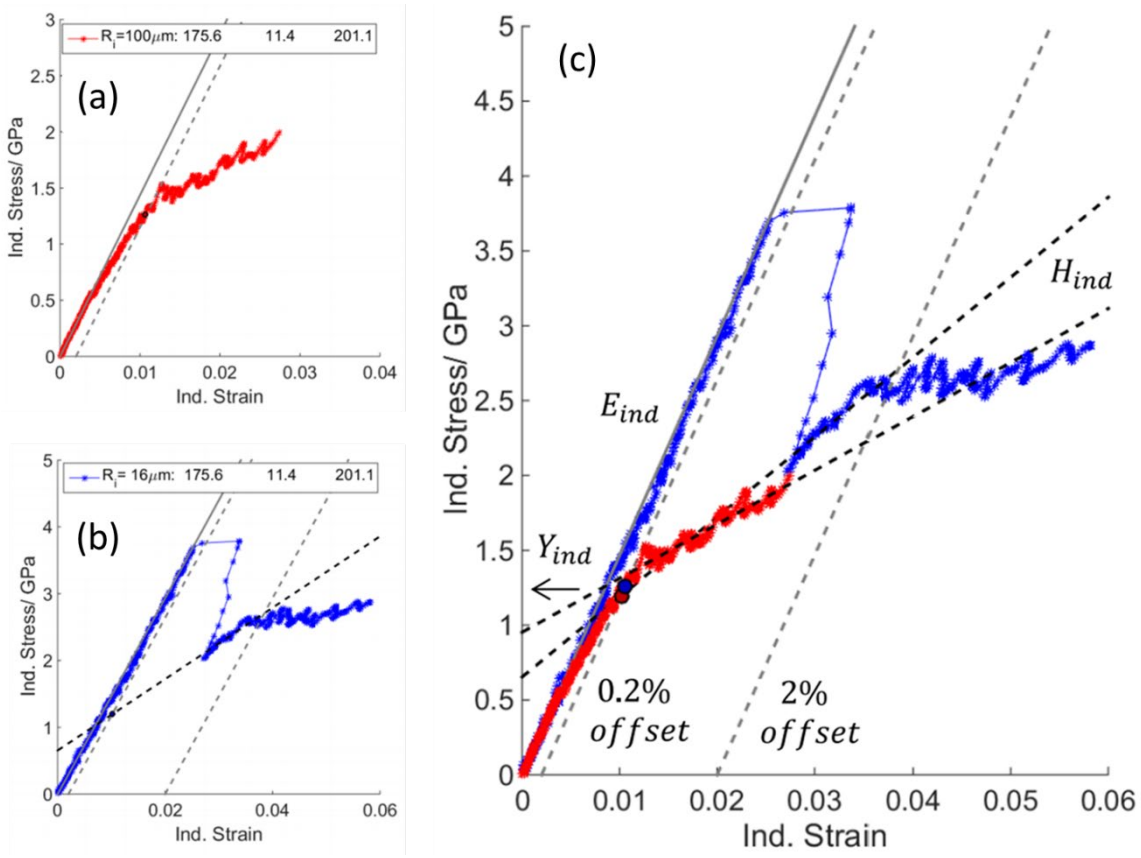

Figure 2.8: In the ISS analysis method, in the absence of pop-in (a), the indentation yield strength (Y_{ind}) is defined by 0.2% strain offset. In the presence of pop-in the back extrapolating the post pop-in ISS data to a 0.2% strain offset is used to determine the indentation yield strength (Y_{ind}). Taking this approach makes ISS analysis protocol insensitive to the indenter tip radius (c).

2.4. Microindentation stress-strain protocol

As mentioned earlier, most of the prior work on indentation stress-strain curves has been focused on evaluating the plastic response at length scales that were significantly smaller than the grain size [53, 55, 56, 58-60]. In order to characterize mechanical properties of hierarchical materials we need to have a tool capable of collecting mechanical properties at different scales. This can be simply done in spherical indentation tests by changing intender tip radius as illustrated in Figure 2.9. However, increasing tip radius required higher load capacity on the instruments. The current nanoindentation machine used in this study has a load capacity of $10N$. For larger tip radii

(referring as microindentation), a device with higher load capacities is required. For this purpose, we utilized a customized Zwick-Roell Z2.5 hardness tester with maximum load capacity of 2,500 N and two sizes of tungsten-carbide spherical tip with radius of $500\mu m$ and $6{,}350\mu m$.

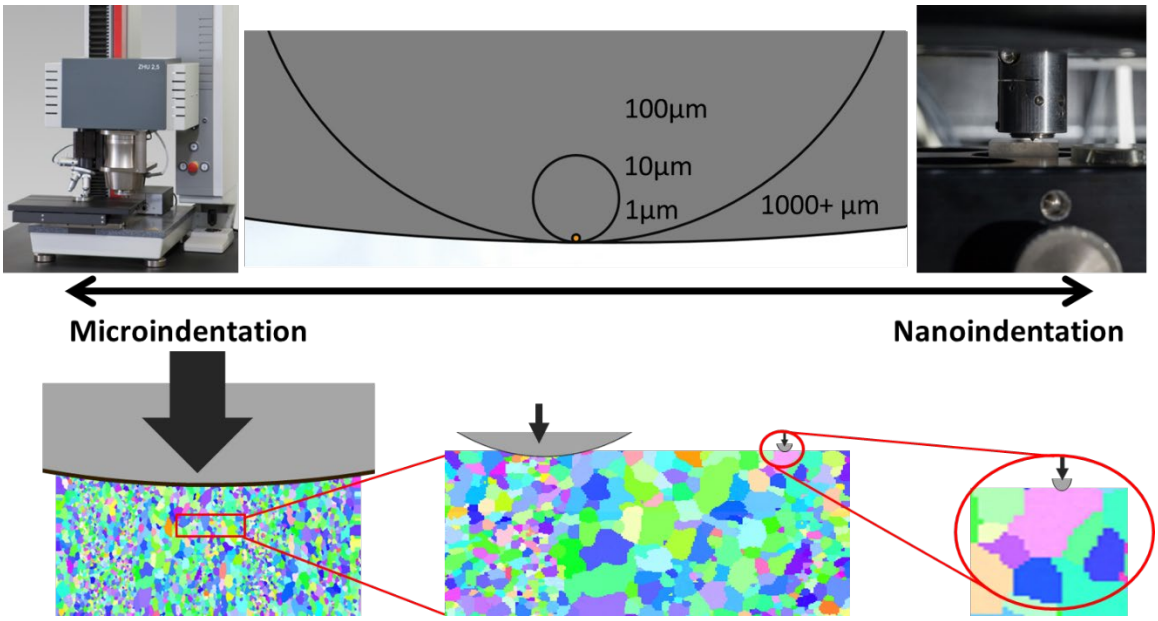

Figure 2.9: Spherical indentation with different indenter tip radius can measure mechanical properties at different scales from sub-grain to multi-grains.

One limitation of the current high load capacity indenter is the lack of CSM measurements. As described in the previous section, the conversion of load-displacement plot into indentation stress-strain curves needs the CSM measurement. Therefore, a new protocol was developed on microindentation that is capable of extracting indentation stress-strain curves without CSM [57, 100]. Consequently, the only way to estimate the contact radius reliably is to employ a multitude of unloading segments, and analyze them using Hertz theory [57]. Therefore, custom protocols were designed and implemented to allow a multitude of loading-unloading (corresponding to about 30-50% of the peak force) cycles (see Figure 2.10 (a)). Since each unloading segment produces one data point on the indentation stress-strain curve (Figure 2.10 (b)), the number and frequency of

the unloading segments has to be suitably adjusted to produce a meaningful and practically useful indentation stress-strain curve. In other words, to obtain a smooth indentation stress-strain curve at the elastic-plastic transition zone, the first unload should be chosen such that the material is barely deformed plastically. Therefore, most of the data points up to the first unload are still in the elastic regimes.

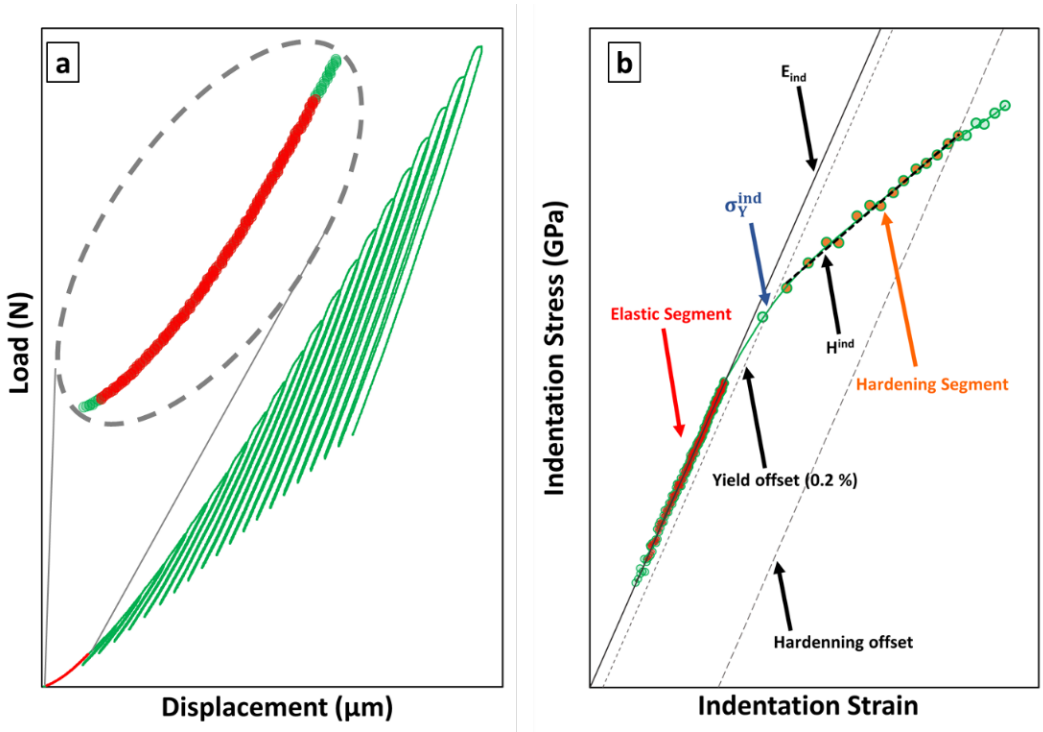

Figure 2.10: Schematic of microindentation stress-strain curves by applying several unloading segments on load-displacement.

To find an approximate maximum force for the first unload, for each new material, a set of single load-unload curves are required for different maximum force peaks. An example load-unload on a dual phase steel illustrates the selection of first unload in Figure 2.11. The material is tested with few single load-unload indentation tests. In this example, four maximum force of 5, 15, 25 and 35 N are applied and then unloading were recorded to 50% of the maximum force. The loading and unloading segments are highlighted in orange and blue colors respectively. As one can see in Figure 2.11 (a-d), by applying 5N, the unloading segment follows the same path as loading segment

indicating the material is still in fully elastic regimes. Increasing the maximum force results in a larger deviation of unloading segment form loading segments.

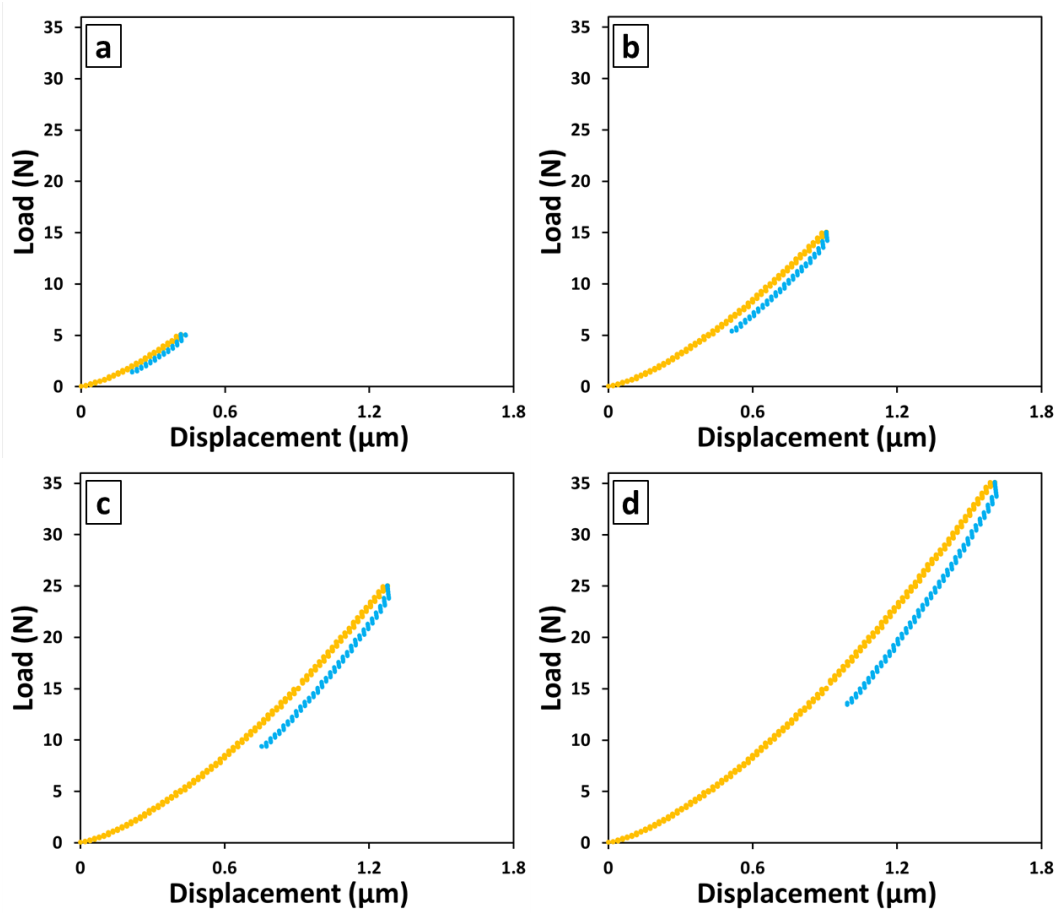

Figure 2.11: Preforming multiple indentation test in order to find out an estimation of maximum load or the where the material has not start deforming plastically.

The protocols for extracting indentation stress-strain curves from the raw load-displacement data from microindentation are based protocol developed by Pathak et al [57] which is still based on Hertz theory [106] as described in Section 2.3.3, and can be found in Equations (2.4) to (2.7). For ease of accessing to the equations, they are listed as follow:

$$P = \frac{4}{3} E_{eff} \sqrt{R_{eff} h_e^3} \tag{2.23}$$

$$\frac{1}{E_{eff}} = \frac{1-v_i^2}{E_i} + \frac{1-v_s^2}{E_s} \quad \textbf{(2.24)}$$

$$\frac{1}{R_{eff}} = \frac{1}{R_i} + \frac{1}{R_s} \quad \textbf{(2.25)}$$

where P and h_e are the indentation load and the elastic indenter displacement, and R_{eff} and E_{eff} are the effective radius and effective modulus, respectively. Constants (E_i , $\mathcal{V}_i$) and (E_s , $\mathcal{V}_s$) are Young's modulus and Poisson ratio for the indenter and the sample, respectively. For the initial elastic loading of a flat sample surface, the effective radius, R_{eff}, is equal to the indenter radius, R_i. Therefore, it would be possible to extract E_{eff} from the measured load-displacement using standard regression techniques

$$h = k(P - P^*)^{\frac{2}{3}} + C \quad \textbf{(2.26)}$$

$$k = \frac{3}{4} E_{eff}^{-\frac{2}{3}} R_i^{-\frac{1}{3}} \quad \textbf{(2.27)}$$

$$C = h^* \quad \textbf{(2.28)}$$

E_s can be recovered using Equation (2.24). Similar to nanoindentation protocol the microindentation stress-strain analysis also requires establishment of zero-point correction. However, the indentation stress-strain curves become almost insensitive to the surface quality of both sample and indenter. Consequently, for the microindentation testing here, there was no need for a zero-point load correction. In practice, the zero-point correction is found to be almost zero in majority of indentation tests (see Figure 2.12).

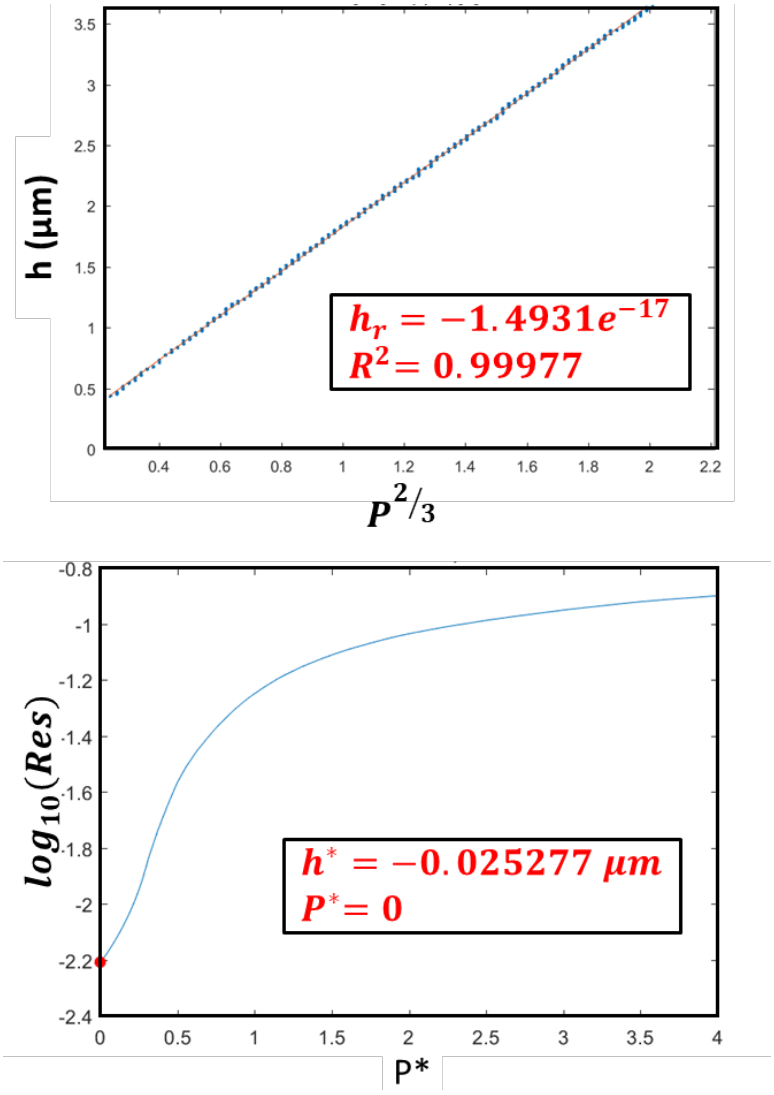

Figure 2.12: Microindentation stress-strain curves show far less sensitivity to surface quality and therefore almost no zero correction requires in most of the tests.

After the material in the indentation zone experiences plastic deformation, Equation (2.26) needs to be modified to introduce the permanent displacement or residual height, h_r:

$$h = \left[\frac{3}{4}\frac{1}{E_{eff}}\frac{1}{\sqrt{R_{eff}}}\right]^{\frac{2}{3}} p^{\frac{2}{3}} + h_r \qquad \textbf{(2.29)}$$

Note that Equation (2.29) can only be applied to unloading segments (these are assumed to be elastic). Applying standard regression techniques on the unloading segments to fit Equation

(2.29) produces reliable estimates of h_r and R_{eff}. In this analysis protocols, it is assumed that E_{eff} obtained from the initial elastic loading segment remains unchanged. This is a reasonable approximation for most materials, given the very small strains introduced in the indentation studies presented in this work. An unloading segment between 95% and 50% of the peak load (in each unloading) was employed in this work to estimate the evolving values of h_r and R_{eff}. After the initiation of plastic deformation in the sample, R_{eff} is no longer equal to R_i. Indentation stress, σ_{ind}, and indentation strain, ε_{ind}, corresponding to the start of each unloading segment are computed as

$$\sigma_{ind} = \frac{P_{max}}{\pi a^2} \tag{2.30}$$

$$\varepsilon_{ind} = \frac{4}{3\pi}\frac{h_{s,max}}{a} \tag{2.31}$$

$$a = \sqrt{R_{eff}(h_{s,max} - h_r)} \tag{2.32}$$

where P_{max} and $h_{s,max}$ are load and displacement at the peak of each unload, and a is the contact radius. $h_{s,max}$ is used to compensate the elastic displacement of the indenter, h_i, and is computed as:

$$h_s = h - h_i \tag{2.33}$$

$$h_i = \frac{3\left(1 - v_i^2\right)P}{4E_i a} \tag{2.34}$$

Young's modulus, E_i , and a Poisson ratio, v_i , of 640 GPa and 0.21 [143] were used for the tungsten-carbide spherical indenter. Equation (2.34) essentially estimates the indenter displacement by using Hertz's theory for indentation on a rigid flat surface. After converting load-displacement plot to indentation stress-strain curves, materials properties, such as elastic modulus, indentation yield strength, and indentation work hardening can extracted (see Figure 2.10. One should notice that, the measured mechanical properties using microindentation is very close to the

bulk properties of the tested materials since the indentation zone using a large tip covers multiple grains and phases.

To investigate the validity of microindentation measurements, a case study was performed on aging process of Al6061 alloy in which aging heat treatment alter its uniaxial yield strength. Two different testing protocols are performed to measuring mechanical properties; standard uniaxial tension and microindentation testing protocols. For standard tension test, multiple coupons of materials were solution annealed and then aged at 204, 274, 343, and 413 °C for 2 hours and then followed by water quenching. The aging process alters the volume fraction and type of precipitates in this alloy and microstructure characterization by EBSD showed that it has small effect on the overall texture of the material [144-146]. Then samples were machined to the standard dimensions according to with ASTM Standard E8-15 [101]. In the other testing protocol, indentation test was performed using a spherical tungsten-carbide tip which had a nominal composition of 94 wt.% WC and 6 wt.% Co and a radius of 6.35 mm. Since the probed volume in indentation is much smaller compared with the conventional testing, it is possible to design a customized sample that has a well-controlled thermal gradient. This high throughput sample can serve as a sample library (Figure 2.13) to explore the full range of aging temperatures. In this design, a cylindrical rod of 1.5 cm diameter and 18.7 cm length of the same material was used as a sample. It was held with one end in molten salt held at 480 °C, and the other end bolted to an aluminum block cooled continuously using a chiller and a 50/50 mixture of ethylene glycol and water maintained at 10 °C. On the section of the sample that was above the molten salt, eight small, equally spaced, holes were drilled to the center of the rod to place thermocouple sensors (K-type) to measure the local temperature histories. The sample was also insulated to minimize heat loss. The sample was aged 2 h in the setup described above and water quenched. Then it was sectioned along its axis and metallographically prepared for indentation as shown in Figure 2.13 (b). Each column (perpendicular to the applied gradient) in the array of indentation tests represents one process in the sample library.

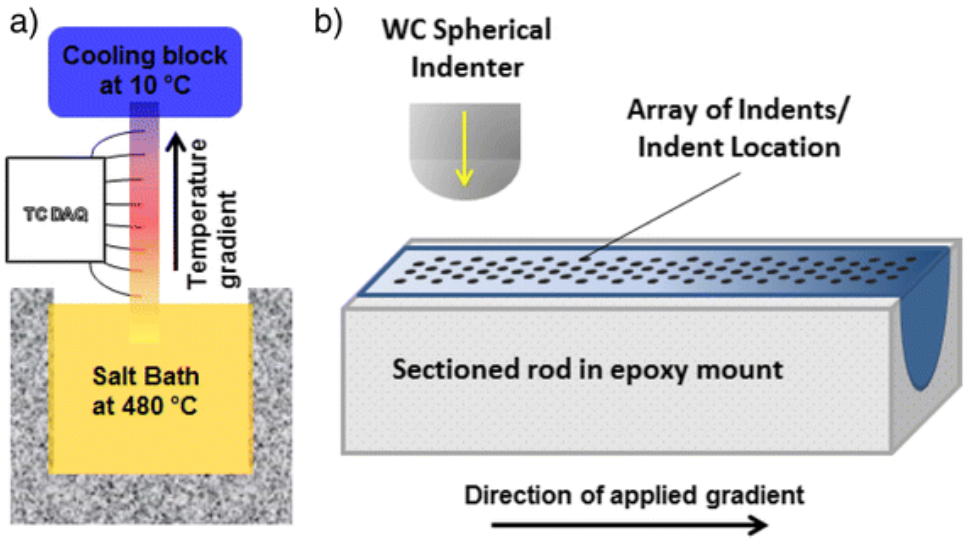

Figure 2.13: Schematic of high throughput testing protocol with a thermal gradient.

Results from both tension and indentation testing protocols are presented in Figure 2.14 in red (after applying converting factors that will be explain in next section) and blue colors respectively. As one can see, very similar results were obtained from both protocols. This is a very good example of how combining indentation protocol with a sample library speed up exploring aging process on this material. The recorded spent time in both testing protocol proves the effectiveness of the high throughput protocol (Figure 2.15). Looking at time and cost per sample provides better image of how efficient is the high through put protocol. The total time on both processes includes time spent on cutting, machining, polishing, heat treatment, test set-up, testing, and test analysis. The calculated overall time per test is ~12 and ~90 minutes for HT and conventional protocols respectively. The calculated overall cost per test is ~$19 and ~$250 for HT and convention protocols respectively. As one can see, the time spent per sample in high throughput method is almost 7.5 times faster than conventional method. Likewise, the cost per test is ~13 times less in high throughput compared to conventional protocols. It is worth to mention that investigating another condition in high throughput protocol will not only cost $11 per test (the cost associate

only with test set-up, testing and analysis) but also it lowers the total cost per test. While adding another condition by conventional testing costs $250 and no effect on the overall cost per sample. In addition, the readers need to pay attention that this recorded time and cost per test is only for mechanical testing not for microstructure characterization which requires preparing separate sets of samples for that purpose in conventional protocol while in high throughput method no extra effort is needed.

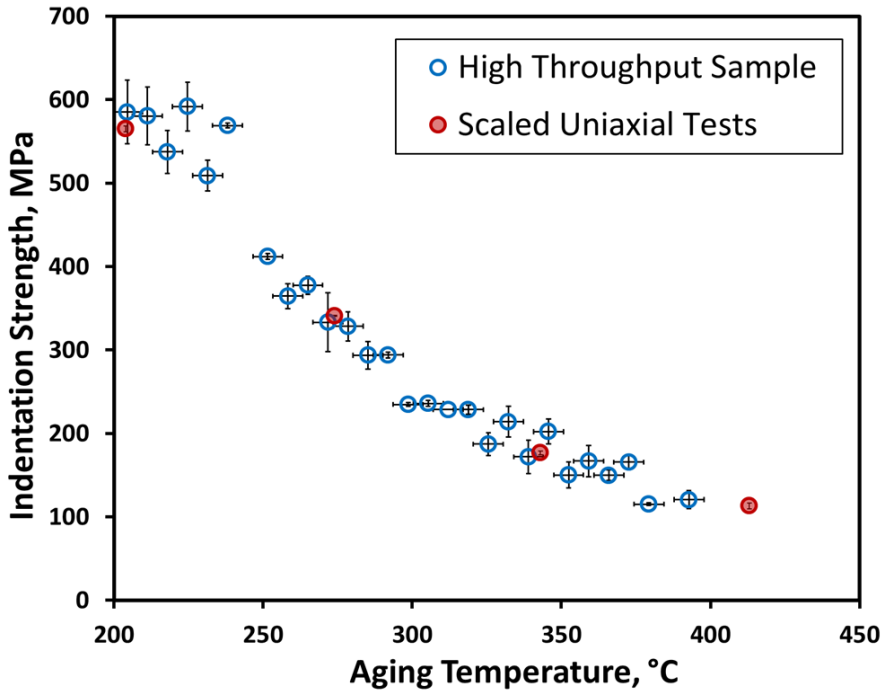

Figure 2.14: Comparison between from conventional testing and high throughout method.

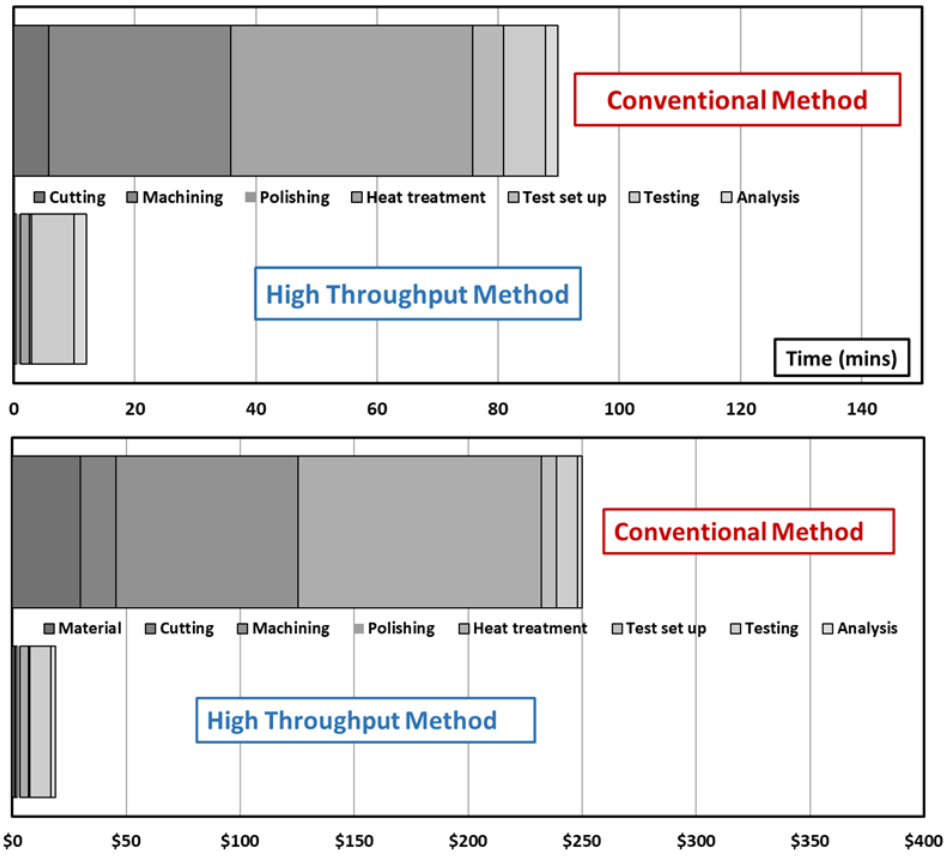

Figure 2.15: Comparison between times spent on conventional testing and high throughout method.

2.5. Conversion of indentation to tensile stress-strain

It should be clear that the uniaxial stress-strain data cannot be compared directly with the indentation stress-strain data, as these impose very different plastic deformation fields in the sample. Obviously, some scaling factor needs to be applied to the indentation results in order to compare with uniaxial tension results. This ratio accounts for the fact that the hydrostatic stress component is significantly higher in the indentation test conditions, compared to the uniaxial stress conditions. In the experiment on Al6061 alloy, the ratio between the 0.2 % offset indentation yield strength and the 0.2 % offset tensile yield strength was observed to be about 1.9, with a standard deviation of 0.3.

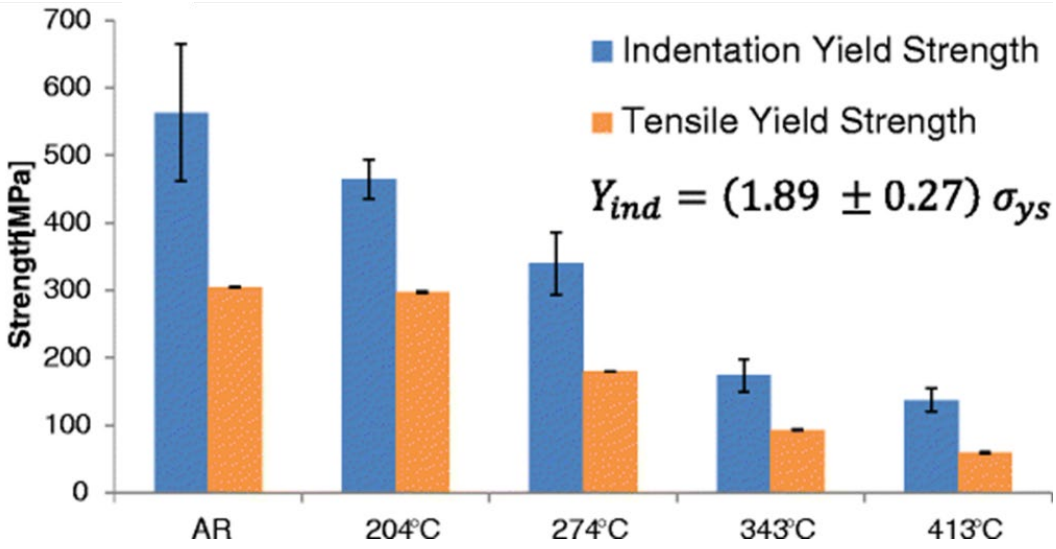

Figure 2.16: Direct comparisons between spherical indentation and uniaxial tensile measurements on the samples subjected to the same aging treatments. The indentation measurements reveal the same trends seen in the bulk tensile samples (i.e., decreasing strength with aging temperature). The ratio between the 0.2 % offset indentation yield strength and the 0.2 % offset tensile yield strength was observed to be about 1.9, with a standard deviation of 0.3.

Literature reports a value of around 2.8 for the indentation constraint factor defined as the ratio of hardness or mean pressure to uniaxial flow stress. These studies are primarily inspired by Tabor's initial experiments conducted on copper and steel for which he identified a ratio of 2.8 (see Section 2.3.1). In Tabor's experiments, the contact radius (actually the projected contact area) was determined from residual indents after complete unloading. It should be recognized that the protocols described and employed in the present work follow the definitions arising from Hertz's theory, where the contact radius and the corresponding projected contact area are both defined in the fully loaded condition. Furthermore, the measurements Tabor made required a significant amount of plastic deformation in order to make a residual indent, whereas this study quantified the 0.2 % offset indentation yield strength, which is well below the typical plastic strains seen in hardness measurements. The contact radius at peak load should be expected to be greater than the contact radius measured on residual indents because of the elastic recovery; this difference will be

significant in the early portion of the stress-strain curve (note that for a purely elastic indentation there is no residual indentation).

Further assessing the literature that supports a constraint factor of 2.8, it is noted that some researchers [110, 147-149] have indeed measured the contact radius in the fully loaded condition [105, 110, 150] [2, 5, 53], which appears to negate the arguments made earlier and adds significant confusion. Our interpretation and rationale is as follows. First, the agreement on the constraint factor for protocols which measure the contact radius in the fully loaded condition and from residual indents is largely based on the material response after significant plastic deformation has occurred at the indentation site (i.e., a fully plastic zone is established at the indentation site). At such large plastic strains, the difference between the contact radius in the fully loaded condition and from residual indents, as Tabor used, is significantly less than during the early stages of plasticity. Consequently, experiments in this regime using both definitions of contact radius provide similar constraint factors. Second, the protocols used to estimate the contact radius in the fully loaded condition [105, 110, 150] in prior studies are not the same as those used in this work [57, 89]. Donohue et al. [151] critically evaluated these differences using a finite element model as a surrogate for the indentation experiment. These authors found that the protocols used in literature estimate the actual contact radius while the protocols used in this work estimate the Hertzian contact radius—one that is consistent with Hertz's theory. Additionally, the Hertzian contact radius was found to be larger than the actual contact radius once plasticity initiates (even at small plastic strains).

In a recent work based on finite element simulations employing isotropic plasticity models, Patel et al. [97] suggested scaling factors of 2.2, 2.0, and 1.3 for the stress, elastic strain, and plastic strain, respectively and presented in Figure 2.17. The scaled indentation stress-strain curves can be interpreted as data from indentation measurements in substantially large indentations, within the assumptions of an isotropic plasticity model for the effective material response.

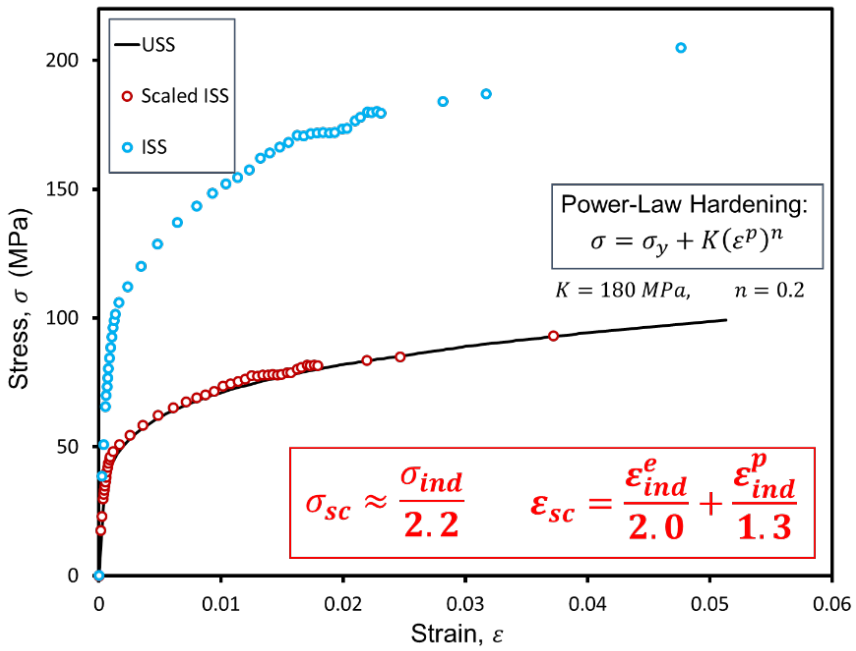

Figure 2.17: An example of converting an indentation stress-strain curve using the scaling factors by Patal et al. [152]. The FE simulation model is for a simple power law with K =180 and n=0.2 for the case of aluminum.

These factors were applied to Al6061 results to scale the measured tensile stress-strain curves on different aging temperature. Once again, a 0.2% offset is used on all plots to calculate the yield point. Finally, the indentation yield strength from all indentation tests and scaled tension tests are presented in a single plot in Figure 2.14. It should be noted that the scaling factors proposed by Patel et al. [152] value corresponds to isotropic elastic-plastic response of the sample material obeying the J2 flow theories. Keeping in mind that the real material behavior in our tests is likely to deviate somewhat from this idealized material law, it is remarkable that our experiments have indicated an average value of 1.9 with a standard deviation of 0.3.

Chapter 3 Microstructure quantification and PSP linkages

Most structural materials have microstructural hierarchy that can be manipulated by undergoing different processing steps to improve their performance in order to be used in advance applications. Any change in the microstructure of a material directly influences its physical, chemical, and mechanical properties. Finding how the microstructure of a material is altered by different processing conditions and consequently affecting the materials properties is the main concept in the field of materials science and engineering.

The introduction of the first commercial scanning electron microscopes (SEMs) in 1965 has changed microstructural characterization in the field of materials science. Higher resolution down to an atomic scale as well as uncovering several buried microstructure details opens the door to a new world for materials researchers. Despite technological advances in characterization techniques, microstructural quantification techniques are still in a very primitive state. Most of these quantification techniques, analyze the collected rich data from advance instruments, and only extract very simple descriptor of the microstructure as a simple scalar measure such as volume fraction, particle size, particle spacing. One can notice that none of these simple scalar measures can fully describes the microstructure of a material as many different microstructures with completely different corresponding properties can exhibit the same volume fraction (as an example of scaler measures). An example of this situation is presented in Figure 3.1 where the microstructure of two bulk metallic glass composite alloys and their corresponding uniaxial mechanical tests are presented. Both alloys were prepared with the same processing history but with different alloy compositions that result in different morphologies of the glass phase. Despite similar volume fraction of glass phase (bright phase in micrographs), two alloys have different mechanical responses. This example shows the deep deficiencies in using scalar measures as a representative of a material's microstructure. This is an example of many other situations that shows a rigorous, systematic, and modern analysis approach is needed to fully quantify the materials microstructures.

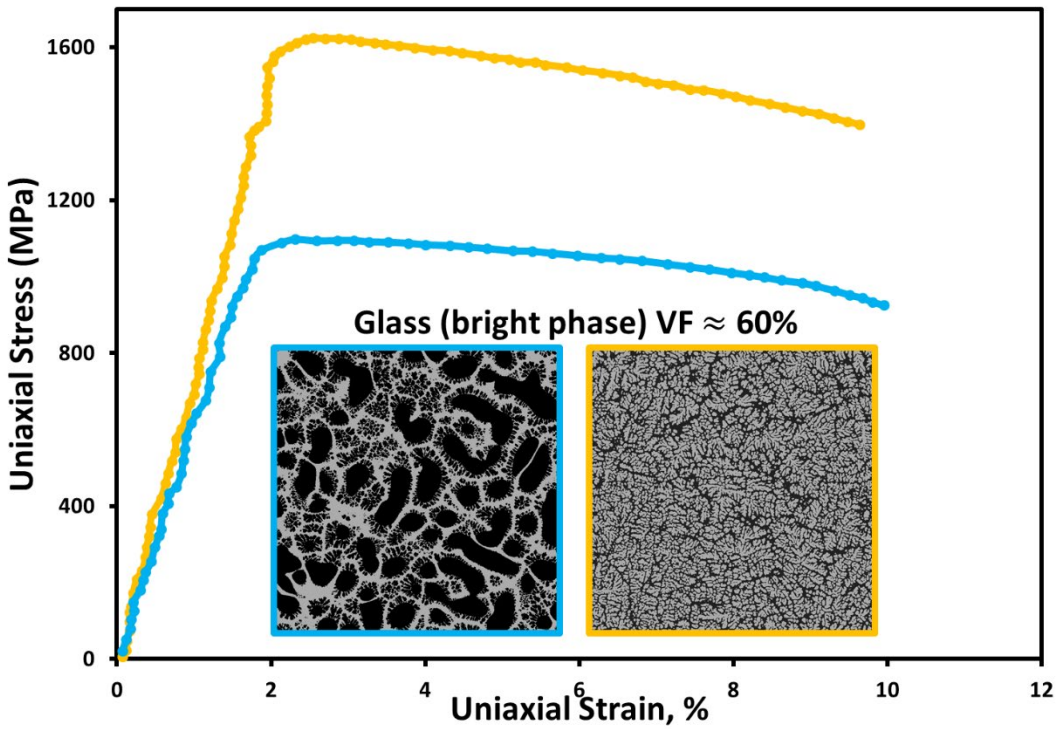

Figure 3.1: Examples that show simple measures such as volume fraction is not sufficient in quantifying microstructure. Two different composition of Ti-based bulk metallic glass matrix composites (BMG-MC) have different mechanical prosperities while both alloys show the same volume fraction of glass phase.

3.1. Microstructure function and local state space

A microstructure function describes the connection between a spatial location (x) in the material volume being studied to the local state, (h), of the material at that location which can be expressed as $m(h, x)$. In this definition, the local State (h) is a material structure attribute at the selected length scale that governs material properties of interest. The complete set of all theoretically possible local states defines the local state space(H). A local state can be specified by a thermodynamic phase, chemical composition of the phase, crystal orientations of phase, or amount of local defect in the lattice. In practice, all microstructure characterization techniques probe the local state in the material over a finite volume and a finite time interval, both of which are dictated by the resolution limits inherent to the characterization technique/equipment used. Since the local state can only be characterized as an average measure over a finite probe volume

and a finite time step, it becomes necessary to allow for the presence of mixed local states in the description of the microstructure function. (e.g., quantifying regions near grain boundaries or phase boundaries in multiphase polycrystalline materials systems). The microstructure function $m(h, x)$ is defined as the probability density associated with finding local state h at the spatial location x.

3.2. Two-point statistics

As described earlier, a robust method is needed to fully quantify a microstructure. The framework of using 2-point statistics with PCA analysis has shown promise in past studies [30, 31, 68, 72, 74, 75, 153]. The 2-point statistics are denoted as $f_r^{hh\prime}$ and are computed as [154]:

$$f_r^{hh\prime} = \frac{1}{S_r} \sum_{s=1}^{S_r} m_s^h \, m_{s+r}^{h\prime} \tag{3.1}$$

where S_r is the total number of bins in the microstructure, m_s^h is discretized representation of the microstructure denoting the volume fraction of local state h in voxel s, and r indexes discretized vectors placed into the microstructure for evaluating the 2-point statistics. In essence, the 2-point spatial correlations capture the probability of finding discrete local states h and h' at the tail and head of a discrete vector indexed by r (Figure 3.2). These spatial statistics maps contain a tremendous amount of information about the morphology and distribution of the local states in the microstructure. For example, the center peaks in the autocorrelations provide the volume fraction information. The contours in the center of the autocorrelation plots provide quantitative information on the shape of local state field in the microstructure. One can also extract a large number of conventional microstructure measures from these plots [30, 31], and even reconstruct the original microstructure from its spatial correlations [155-157].

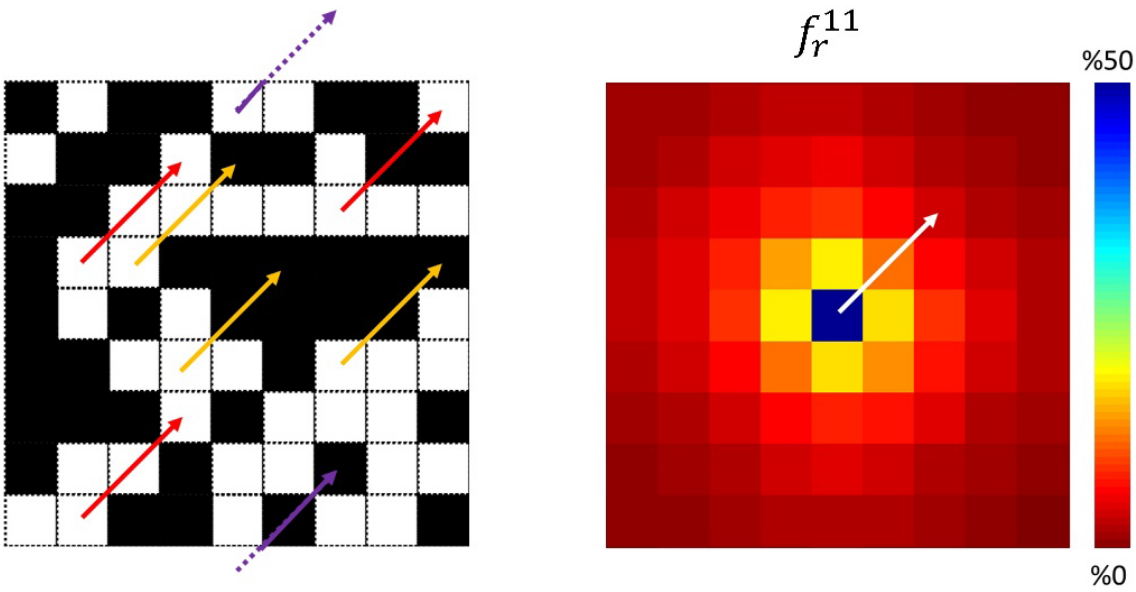

Figure 3.2: Schematic micrograph of two-phase material and corresponding 2-point statistics of the microstructure. The microstructure consists of two local states; white and black, the head of the white vector shows the probability value of finding similar vectors (in terms of size and direction) with both head and tail in white phase if randomly placed on the micrograph on left.

3.3. Dimensionality reduction

The quantification of microstructures using the framework of 2-point statistics produces a very large vector of descriptors for the microstructure (every voxel in each of the correlation maps would be an entry in this vector). Principal component analyses (PCA) has been shown to be remarkably effective in arriving at objective (data-driven) low dimensional representations [34, 68, 74, 153, 158-161] of the microstructure. Mathematically, this can be expressed as

$$f_r^{(k)} = \sum_{i=1}^{P-1} \alpha_i^{(k)} \varphi_{ir} + \tilde{f}_r \qquad \textbf{(3.2)}$$

where $f_r^{(k)}$ denotes a contracted representation (i.e., as a single vector) of all the spatial correlations of a microstructure indexed by k, $\tilde{f}_r$ denotes the ensemble average of all microstructures included in the analyses, φ_{ir} denote the directions of the new linearly transformed reference frame (identified by PCA) and α_i are the coordinates (also called PC scores) in the new

reference frame. A salient feature of PCA is that it transforms the data into a new orthogonal frame where the axes are ordered by the maximum variance seen in the data.

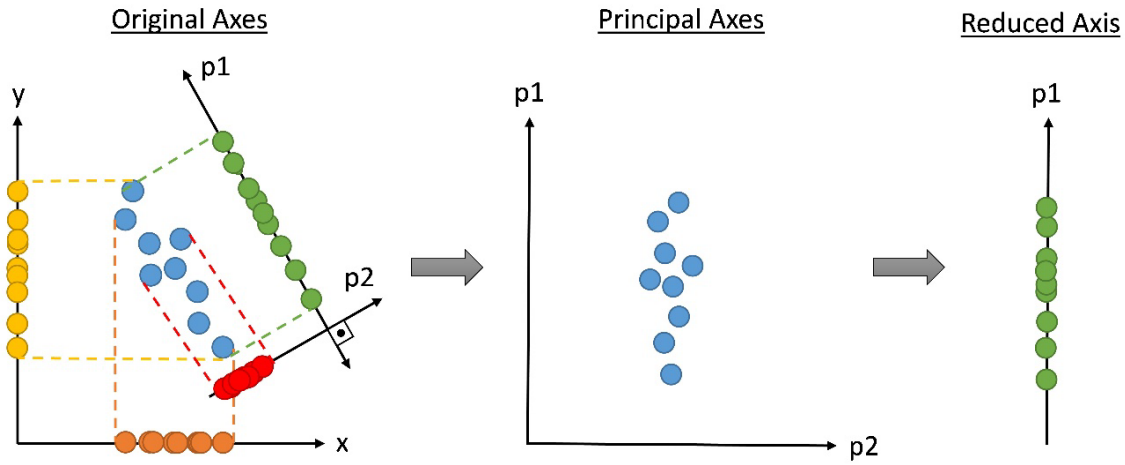

Figure 3.3: Low-dimensional representation of the 2-point statistics of few micrographs obtained from PCA.

Examples of 4 classes of two-phase microstructures and their corresponding 2-point statistics are presented in Figure 3.4 (a-h). Microstructures from Classes ***a*** have randomly distributed non-overlapping ellipses with horizontally alignment. The microstructures in Class ***b*** and ***d*** have ellipses in two orientations with 30 and 90° misalignment between the orientations of ellipses respectively. The class ***c*** has randomly distributed non-overlapping circles. All microstructures had generated such that the volume fractions stays very close to 20%. Except class ***c*** where circles is used to generate microstructure instead of ellipses, other microstructure classes contain ellipse with the same size and aspect ratio. Therefore, all traditional scalar measures of the microstructure such as volume fraction, size, and aspect ratio are identical for all these three classes. On the other hand, the 2-point statistics maps (autocorrelations of the white phase) retain all details of the microstructure (Figure 3.4 (e-h)). As an example, the value of the maximum peak in the center of the 2-point statistics plots which is the probability of finding of white local state at the tail and head of vector size 0 is nothing but the volume fraction of white phase and it is 0.2. Moreover,

the shape of the 2-point statistics maps carries information of the orientation and the shape of the features. As one may see the more similar microstructure (***a*** and ***b***) the closer their corresponding 2-point statistics data points in the PC space.

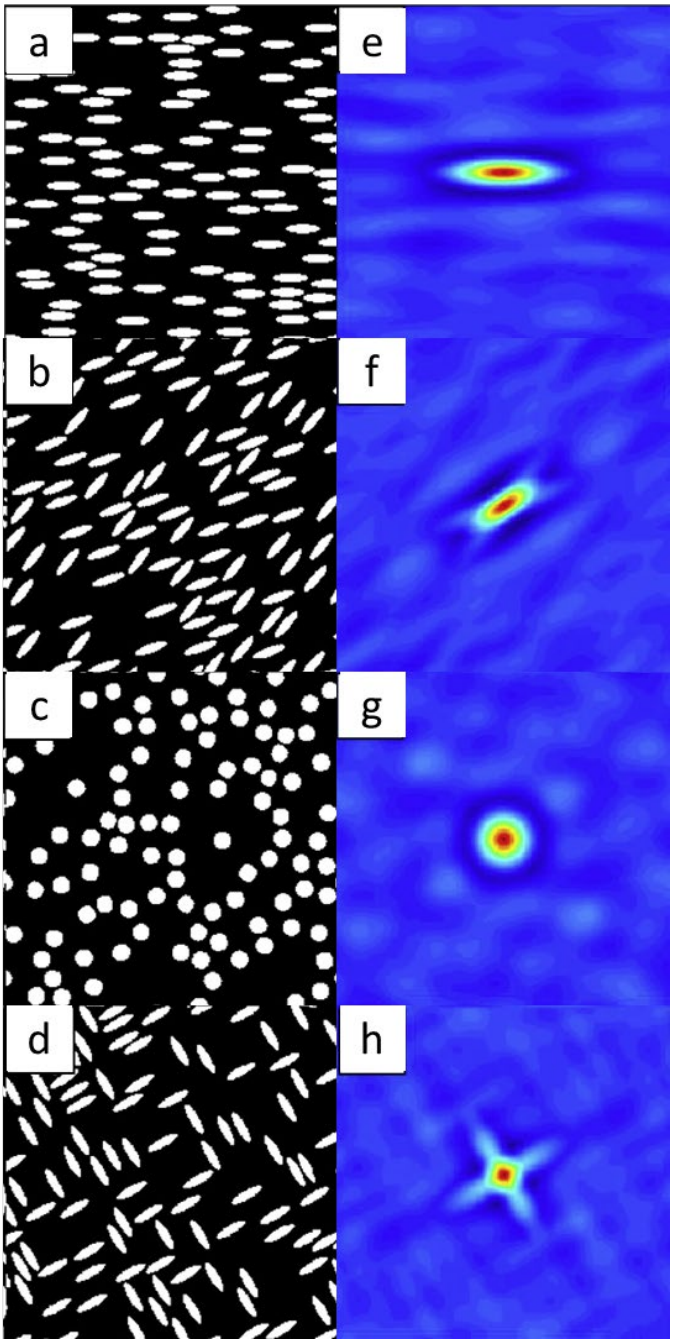

Figure 3.4: Examples of microstructure of two-phase material with in four different configuration classes. The autocorrelations of the white phase (i.e., ellipses) for the microstructures shown on the left contains all detail of the corresponding microstructure. [162]

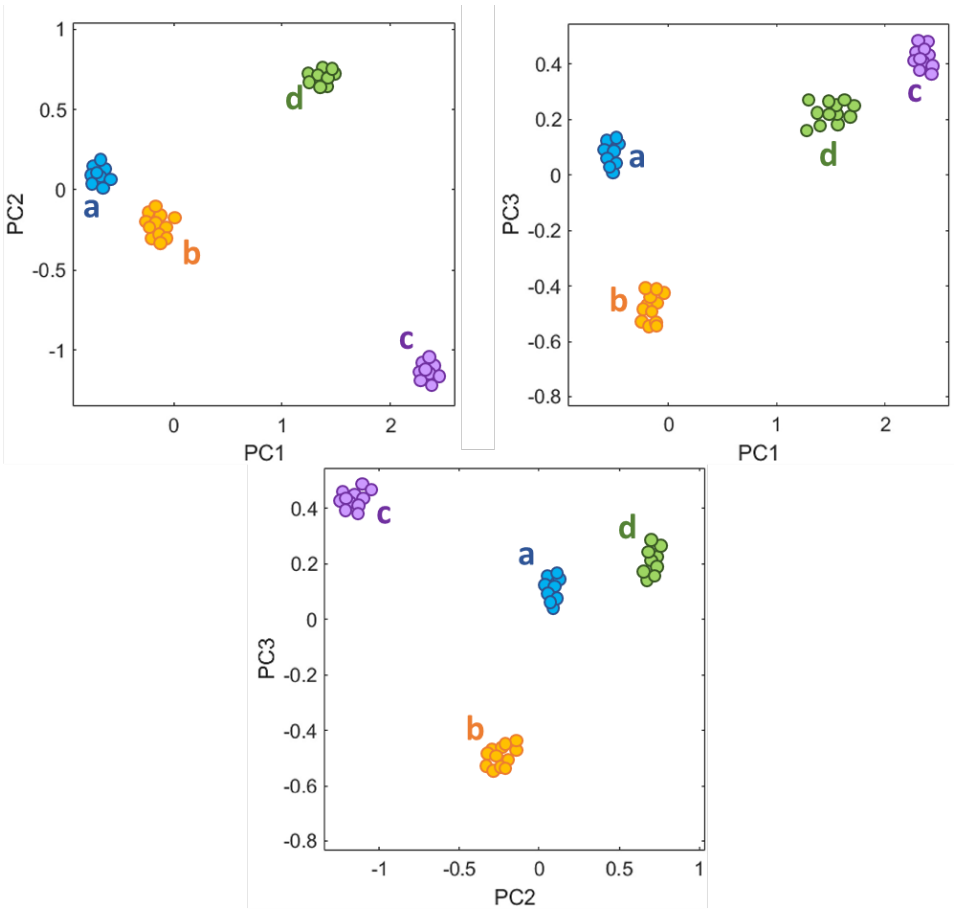

Figure 3.5: Visualization of two-point spatial correlations of the 4 classes of microstructures in the reduced-order PC space. Left, middle and right plots show PC1 vs PC2, PC1 vs PC3 and PC2 vs PC3, respectively [162].

More detailed information can be found in the PC bases. An example of PC spaces is presented in Figure 3.6. Knowing the bases of the new coordinate frame and the average value of all analyzed microstructure data points, the PC scores is nothing but the coordinates of the a microstructure data point in this new frame and can be presented mathematically as Equation (3.2) . The reader should notice that all collected microstructure data points contribute in defining these bases. In other words, adding up more microstructure to this set will change the average as well as the PC bases. Eventually, if enough and wide ranges of the microstructure are added to the analysis, the bases and the average values become less sensitive to adding a new data point.

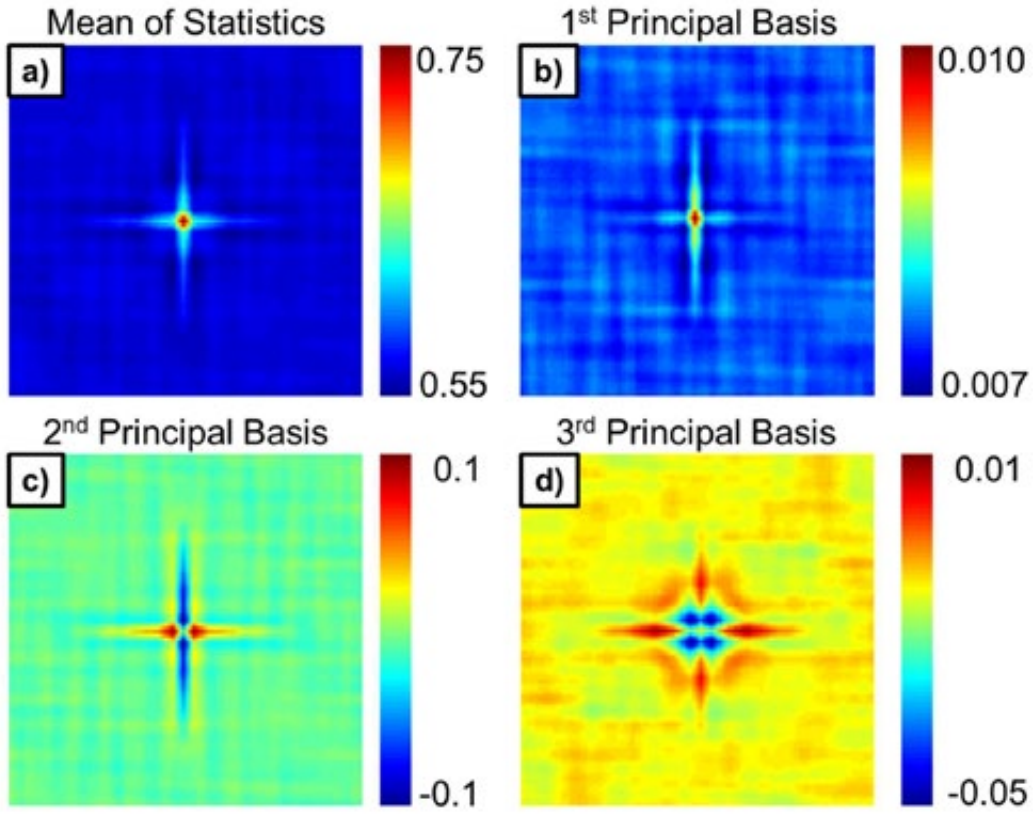

Figure 3.6: (a) The mean of statistics for all 80 microstructures, (b, c , d) first three principal component bases.

3.4. Processing-Structure-Property (PSP) linkages

The structure-property linkage is based on the homogenization theory developed from the statistical continuum theories by Kroner [163, 164]. In the theory the effective stiffness can be expressed as

$$C^{eff} = \bar{C} - \overline{C'\Gamma C'} + \overline{C'\Gamma C'\Gamma C'} - \cdots \quad \textbf{(3.3)}$$

$$\overline{C'\Gamma C'} = \frac{1}{V}\int_V \int_V C'(x)\Gamma(t)C'(x')\,dx'\,dx \quad \textbf{(3.4)}$$

where C and C' are a reference stiffness value and the perturbation from the local property at location x in the microstructure volume of V. The $\Gamma(t)$ is a symmetric second derivative of defined Green's function of the underlying physics of the problem where $t = (x - x')$. The second term in the equation can be recast as follow by using 2-poin spatial correlation

$$\overline{C'\Gamma C'} = \langle C'(x)\Gamma(t)C'(x')\rangle = \int_H \int_H \int_{\Psi(t)} f(h,h'|t)C'(h)\Gamma(t)C'(h')dhdh'dt$$
$$= \sum_{r,n,p} \aleph_r^{np} f_r^{np} \tag{3.5}$$

where f_r^{np} is the 2-poin statistics that contains microstructural information and $\aleph_r^{np}$ are microstructure-independent coefficient that capture physics- governing information of the studied phenomenon. Even though the presented equations are developed and presented for stiffness property, it has been shown in literature that these equations can be used for any nonlinear materials property.

As discussed in previous section, 2-point spatial correlation contains very high dimensional microstructural information, hence PC analysis was utilized to find the most and important microstructure features. Since the PCA is essentially a linear transformation (Equation (3.2)), and using the Equation (3.5), the effective property in Equation (3.3) can be recast as

$$C^{eff} \approx A_\circ + \sum_i A_i \alpha_i \tag{3.6}$$

The α_i are the PC scores of each microstructure and A_i denotes their corresponding influence on the effective property and are independent from the material structure. The goal in data-driven approach is to find a simple format of Equation (3.6) with minimum number of terms which keeps computational cost of the establishing a structure-property linkage very low. In order to do that, the least squares regression analysis with different degrees of polynomial and level of truncation on number of PCs is applied to achieve the most accurate linkages without overfitting. The established linkage then was validated by LOOCV (Leave-One-Out Cross Validation) technique [68].

Example of structure-property linkages from CPFEM simulation results is presented in Figure 3.7. Figure 3.7. (a) Synthetic 12 classes of different textures of the studied Set of 12 α-titanium synthetic microstructures (class A-L) with different textures is used in the study with 30

samples in each class of texture. The elastic stiffness and yield strength are predicted via CPFEM simulations. The classes A-G are used to establish structure-property linkage shown with grey color in the Figure 3.7 (b-d). Rest of the generated textures (class H-L) are used to validate the data-driven SP linkage for both elastic stiffness and yield strength properties which show very good agreement within 1 and 5% error bounds respectively [165].

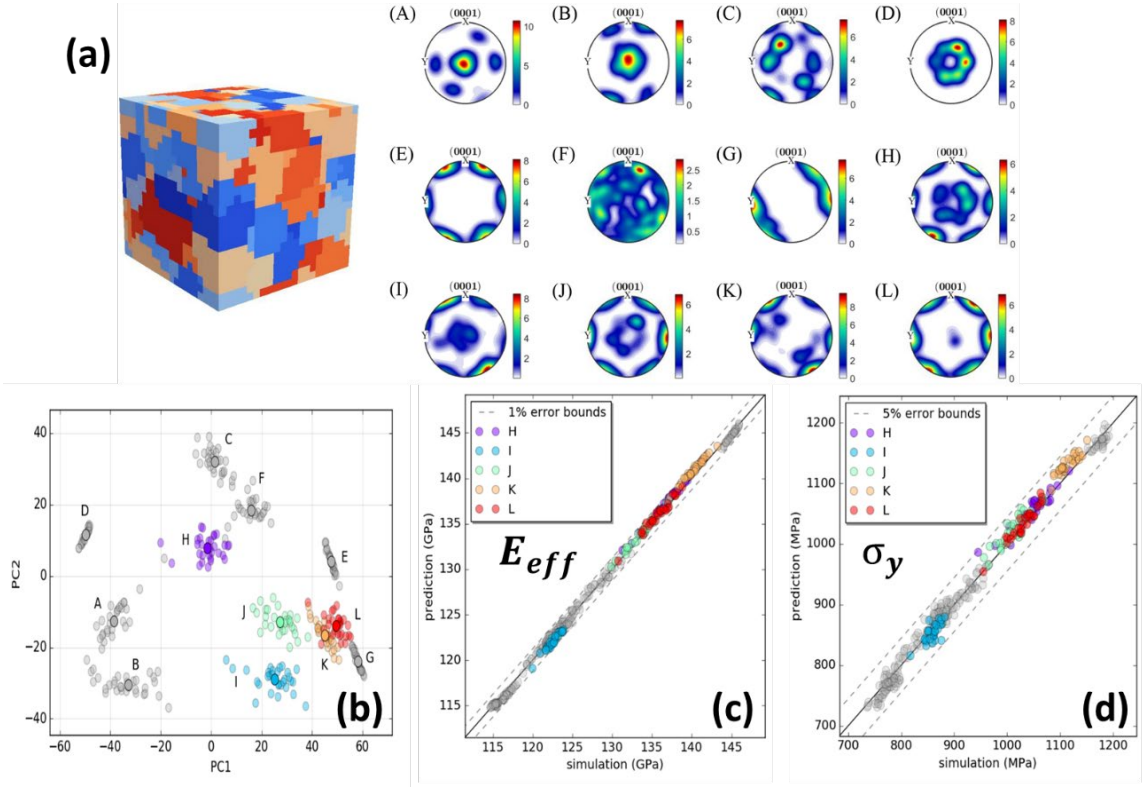

Figure 3.7. (a) Synthetic 12 classes of different textures of the studied α-titanium (b) Representation of all 12 classes after applying 2-point statistics and PC analysis. The class A-G shown in grey are used to train the structure-property linkage. Class H-L (colored ones) are used to show effectiveness of the data-driven linkage. Predicted versus simulated response for (c) elastic stiffness with 3 PCs and (d) yield strength with 6 PCs.

The same approached can be applied in establishing Processing-Structure linkage that captures the details of the microstructure evolution as a function of processing parameters. The difference between the Structure-Property linkage and the Processing-Structure linkage is on the

inputs and outputs. In the former one, the inputs are the PC scores from 2-point statistics and PCA analysis and outputs are the property of interest. In the latter linkage, the inputs are the processing parameters and outputs are the PC scores. This can be denoted with a simple polynomial format as

$$\dot{\alpha}_j \approx \tilde{A}_\circ(\theta_k) + \sum_i \tilde{A}_{ij}(\theta_k)\tilde{\alpha}_i \quad \textbf{(3.7)}$$

where $\tilde{\alpha}_i$ and θ_k are the polynomial combinations of PC scores and process parameters respectively.

The reader is reminded that the PSP linkages developed here are data-driven and a s result the linkage will change when new data is added. When a substantial amount of data becomes available and the collected microstructures cover all possible microstructure for the selected material system, then we could expect the PSP linkages to become stable (i.e., there would be no need to change the PSP linkages with the addition of new data points).

Chapter 4 Application to Dual Phase (DP) Steels

This chapter presents the application of the high throughput indentation testing and microstructure quantification protocols in dual phase steel. Dual phase steel is advanced high-strength steels that are widely used in automotive application due to their combination of high strength and good formability. Their compositions also contain very low alloying elements and their high strength and ductility can be reached by simple thermomechanical treatment, which makes this class of alloy an excellent candidate for weight reduction purpose in vehicle industries to improve fuel efficiency. These alloys also have an excellent fatigue strength and a good energy absorption capacity [38, 41, 45, 47, 51, 62, 63, 66, 166-174]. This outstanding combination of mechanical properties is due to their microstructure.

The microstructure of dual phase steel alloys consists of ferrite and a dispersed hard martensitic phase in the form of islands. Martensite forms during quenching of the steel after holding it at intercritical annealing temperature. During the austenite-martensite transformation, a volume change of 2-4% occurs and produces residual stresses and plastic deformation in the ferrite matrix adjacent to the martensite islands. Applying additional cold work increases the amount of internal stress at the martensite-ferrite interface. The next bake hardening process relief some of the internal residual stresses by letting ferrite and martensite undergo static strain aging and tempering phenomena respectively. As a result of these processes, the DP steel obtains a unique behavior of continuous yield behavior and high work hardening rates.

Despite simple processing steps in producing DP steel, the development of new generation of them requires deep scientific answers to various open questions regarding immense complexity exists in the microstructure and its relationship with mechanical response at different length-scale. To answer these questions this chapter is seeking two goals:

a) Multiscale mechanical characterization of martensite phase

b) Developing protocols in establishing processing-structure-property linkages for yield strength property

In the first step, nanoindentation test were conducted to investigate two major microstructure features: the amount of carbon content and the lath martensite interfaces. During the process of quenching and cold work, the carbon content and defect density in lath martensite varies locally. The heterogeneity becomes more complex when the lath martensite undergoes bake-hardening process during which non-uniformed tempering occurs in the lath martensite. As one can see, the very complicated local structure will definitely result in a very high variance in the small length-scale mechanical measurements and make it impossible to investigate the effect of each microstructure feature individually. For this purpose, we selected two non-commercial Fe-Ni-C alloys with low M_s temperature to minimize amount of auto-tempering during quenching process. Both alloys have a similar Ni content (~5%) but different carbon contents 0.13 and 0.3 wt. %. We tested samples as quenched and no further cold work and bake hardening applied. By changing indenter tip from 1, 16 and 100 μm in radius, we are able to study the effect of the carbon content and lath interfaces systematically on the mechanical response of lath martensite at small length-scales.

In the second step, we selected three intercritical annealing temperature, 3 amount of thickness reduction in cold work, and two bake hardening conditions in exploring the processing space for DP steel production while other processing parameters (alloy composition, annealing temperature and time, hot deformation, initial microstructure, quenching cooling rates bake hardening temperature and time) are kept constant. The bulk mechanical response then measured by microindentation test at various locations. The microstructure of the sample then characterized by EBSD technique. And the PSP linkages is established for the average indentation yield strength (as the property of interest) and the ensemble average of the microstructure for the selected processing conditions.

4.1. Multiresolution mechanical characterization of hierarchical materials: Spherical nanoindentation on martensitic Fe-Ni-C steels

4.1.1. Introduction

In this paper, two model martensitic steels Fe-5.1Ni-0.13C (wt.%) and Fe-5.0Ni-0.30C (wt.%) with different carbon contents were investigated using spherical nanoindentation stress-strain curves to quantify the mechanical behavior of lath martensite at multiple length scales using different spherical indenter tip radii. The indentation yield strength is dominated by the nanoscale defect structure for all indenter radii (1μm, 16μm and 100μm) and does not exhibit any discernable size effect in the measured yield strengths at different length scales. The work hardening rates measured in the indentation tests at the different length scales coincide until the indentation zones grow large enough, so that a significant increase of work hardening occurs which is attributed to the presence of high-angle block boundaries in the indentation probed volumes. Characteristic pop-ins were observed in the indentations performed with the 1 μm and 16 μm indenter tip sizes and have been attributed to the interaction of dislocations with lath boundaries and their eventual transmission. In addition, the correlations between the properties measured from these indentation protocols and those measured in uniaxial tensile tests are critically examined.

4.1.2. Review of Indentation Measurements on Lath Martensite

There is a substantial amount of uncertainty in current literature regarding the properties exhibited by the martensitic phase in high strength low-alloyed steels. Most of the previous indentation studies on lath martensite employed a sharp diamond tip and analysis protocols that analyzed the unloading segments after introducing a significant amount of plastic deformation in the indentation zone in the loading segment [37, 39-41, 46, 175-187]. These indentation protocols can only provide estimates of modulus and hardness. It needs to be pointed out that hardness is a measure of flow strength after some amount of nonstandard plastic deformation has been imposed on the sample. Consequently, it is entirely possible that the intrinsic mechanical properties

estimated in these protocols are significantly influenced by the indentation itself. In fact, most prior studies on different material systems have reported a size effect with higher strength values measured with shallow indentation depths [188-192]. A summary of indentation measurements on lath martensite is presented in Table 4-1. Only a few of these studies attempted to extract the elastic modulus of lath martensite in different alloys. From the reported values of elastic modulus, a large variation in the range of 180 to 320 GPa is observed. Besides the differences in the chemical composition (most prominently C content) being one of the main sources of the observed variance in the measurements, other factors include variations in the testing and analysis protocols (e.g., the indentations in the different studies were carried out to different maximum indentation loads/depths). The variance in the measured hardness is remarkably large not just from one study to another, but also within a study conducted on a single alloy composition. In some cases, the large variance in the reported measurements was explained as size-effects, where smaller indentation tips and shallower indentation depths produced higher values of hardness. Since the hardness measurements obtained at different indentation loads/depths correspond to different amounts of plastic deformation imposed on the sample, it is impossible to ascertain whether the measured size effect is intrinsic to the material or simply a consequence of the protocols employed. As further evidence, it is noted that investigations [39, 176, 177, 180] conducted on various alloy compositions reported almost no size effect with different loads/depths when using a Berkovich tip geometry. However, when the indenter tip was substituted with a Vickers geometry to measure hardness at a larger length scale, lower hardness values were obtained. Generally, from these studies the measured hardness from Berkovich tips were reported to be 1.2 to 2.5 times higher than the ones from Vickers testing. This implies that the geometry of the indenter tip possibly has a significant influence on the hardness measurements. Another inconsistency observed from the previously reported studies can be traced to whether or not the indentations were conducted close to or away from high-angle grain/phase boundaries. In some studies, higher hardness values were reported at locations close to boundaries [180, 187], while in other studies the opposite trend was noted [39].

The effect of carbon content on the hardness of martensite was systematically investigated by Ohmura [176] and Hutchinson [178]. For the same range of C content (0.1-0.5 wt.%), Vickers hardness measurements in the range of 4 to 8 GPa were reported in both studies, despite the significant differences in the compositions of the other alloying elements in the steels studied. This shows that the C content has the greatest influence on the hardness of martensitic steels compared with other substitutional alloying elements.

Table 4-1: Hardness measurements of lath martensite from previous studies on various alloys

Composition	Indenter Type	Max Depth (nm)	Max Load (mN)	Elastic Modulus (GPa)	Hardness (GPa)	Ref.
Fe-0.12C-2Mn-1Si	Berkovich	-	1	-	6.9-8.8	[41]
Fe-0.2C-1.5Mn-2Cr	Berkovich	-	3	-	5.6-7.4	[45]
Fe-0.15C-1.7Mn-0.5Si-0.012Nb	Berkovich	-	0.25-15	-	4.6-7.6	[47]
Fe-0.13C-1.9Mn-0.03Si-0.16Co-	Berkovich	-	3	-	6.2-8.1	[35]
Fe-0.2C-3Mn-1.6Si	Berkovich	30	-	211-215	4.5-8.5	[46]
Fe-32.8Ni	Berkovich	-	0.5	-	3.8-5.5	[37]
	Vickers	-	98, 245, 4900	-	2.06	
Fe-0.39C-0.87Mn	Berkovich	60, 400	-	250-320	5.6-9	[42]
	Vickers	-	4900	-	5.3-5.4	
Fe-0.4C	Berkovich	-	0.2, 0.5, 1	200-220	8-10	[38]
Fe-0.55C-4.16Cr-1.94Mo-1.61W-1.16V	Berkovich	-	0.5	-	10.5-12	[39]
	Vickers	-	4900	-	8.5	
Fe-0.38C-0.2Si-0.67Mn-0.97Cr-0.15Mo	Berkovich	-	10	-	4.9-5.8	[48]
Fe-(0.1, 0.2, 0.4, 0.6, 0.8)C	Berkovich	-	0.5	180-250	5-11	[36]
	Vickers	-	4900	-	4-9	
Fe-0.05C-16Cr-6Mn-6Ni-1Si-0.1Al	Berkovich	-	1	215	7.4-7.9	[34]
Fe-0.05C-17Cr-7Ni-0.5Si-1.5Mn-0.1Mo	Berkovich	-	1	-	3.8-6.5	[50]
Fe-0.95C-1.3Mn-0.91Si-0.23Cr	Berkovich	-	0.5	-	5.9-7.3	[49]
Fe-(0.12, 0.23, 0.31, 0.48)C	Vickers	-	9800	-	3.9-7.1	[40]
Fe-0.13C-5.1Ni	Berkovich	-	0.3	-	6.3-8	[51]

In contrast to the measurements described above with the Berkovich tip, size effects were absent in the indentation yield strengths measured on other alloys [56, 60, 93] using the recently developed spherical indentation stress-strain protocols. Therefore, the indentation yield strengths measured in the new spherical indentation protocols are better measures of the intrinsic material properties, and can be directly related to the details of the microstructure in the probed volume [56, 58-60, 90, 91, 93, 193]. In this paper, we specifically investigated the changes in the indentation yield strengths in two different martensitic steels (with different carbon content) at different length

scales. By systematically changing the length scale of the probed volume (accomplished by using indenters of different tip radii), we were able to identify the respective contributing defects (such as dislocations, interstitial carbon, grain boundaries, etc.) in the microstructure inside the indentation sample volumes probed in our experiments. Furthermore, the indentation results were suitably scaled and compared with the uniaxial mechanical properties (measured in standard tensile tests) to derive new insights on the correlations between the values measured at different length scales.

4.1.3. Materials and Experimental Procedure

Alloy processing: Two non-commercial grade alloys with compositions Fe-5.1Ni-0.13C (wt.%) and Fe-5.0Ni-0.30C (wt.%) were provided by ArcelorMittal Research Center in Maizières (France). Both materials were austenitized at 900 °C for 5 min and water-quenched to obtain martensitic microstructures.

Microstructure characterization: Sample preparation was carried out using standard metallography procedures. This involved grinding with silicon carbide papers down to grade 4000 and polishing sequentially with diamond suspensions of 3 μm, 1 μm, and OP-A alumina/OP-S silica suspension. For microstructure characterization, EBSD (electron backscatter diffraction) and ECCI (electron channeling contrast imaging) measurements were carried out in a TESCAN MIRA3 and a Zeiss "Merlin" scanning electron microscope with a field emission gun at 20 kV and 30 kV, respectively. A working distance of 5-6 mm was used to increase the backscatter electron signal and enhance contrast for ECCI.

A PANalytical's Empyrean X-ray diffractometer with Cu Kα radiation (k = 0.1540598 nm, powered at 45 kV and 40 mA) was employed for scans with the range of 2θ from 30-130° at the rate of 0.04°/min. In addition, higher resolution scans on the (200) and (211) diffraction peaks of martensite were obtained at a small step size of 0.0263° and an acquisition speed of 0.005°/min. The as-acquired diffraction curve was processed by Kα2 stripping and background removing.

Uniaxial tensile property measurements: Tensile testing was performed using standard protocols on specimens with a rectangular cross section of about 4.1 × 0.9 mm^2 and a gage length of 15 mm.

Nanoindentation strain-stress analysis: Spherical nanoindentation tests were performed on an Agilent G200 Nanoindenter with a XP head and a CSM (continuous stiffness measurement) module. The CSM superimposes small unloads with a displacement amplitude of 2 nm and a frequency of 45 Hz on the monotonic loading conditions imposed on the sample. Tests were run with a constant strain rate (loading rate divided by the load) of 0.05 s^{-1} to maximum depths of 300, 500, and 700 nm for indenter tip sizes of 1, 16, and 100 μm, respectively. A minimum of 30 nanoindentation tests was conducted at random locations on the surface of each sample for each indenter size. The collected data was converted to indentation stress-strain using the protocol described in Section 2.3.3.

From each measured indentation stress-strain curve, the indentation elastic modulus, the indentation yield strength, and the indentation work hardening rate were extracted. A 0.002 plastic strain offset was employed to identify the indentation yield strength. The indentation work hardening rate was extracted by fitting a line to the indentation stress-strain plot from the indentation yield point up to 0.015 indentation plastic strain.

4.1.4. Results and Discussion

An overview of the hierarchical martensitic microstructure in both alloys is illustrated in Figure 4.1(a-f). EBSD data, Figure 4.1(a and b), provides information about the crystallographic orientations of laths, blocks and packets as well as information on the prior austenite grain structure. However, EBSD only is not entirely able to resolve the low misoriented substructure within martensite blocks. Yet, electron channeling contrast imaging (ECCI) micrographs in Figure 4.1(c and d) reveal the lath morphologies. This technique permits imaging of defects in the lattice by diffraction contrast, very similar to the two-beam condition technique used in conventional TEM (transmission electron microscopy) for imaging dislocations. The advantage of ECCI over TEM is

that it can be carried out in the scanning electron microscope (SEM) on bulk samples with wider field of view and exhibits excellent capabilities in terms of defect imaging on the micro- and nano-scale [194-198]. Defects such as dislocations produce lattice distortion around the dislocation core that result in contrast changes. The intensity of this contrast depends on how the back-scattered electrons interact with the crystal lattice.

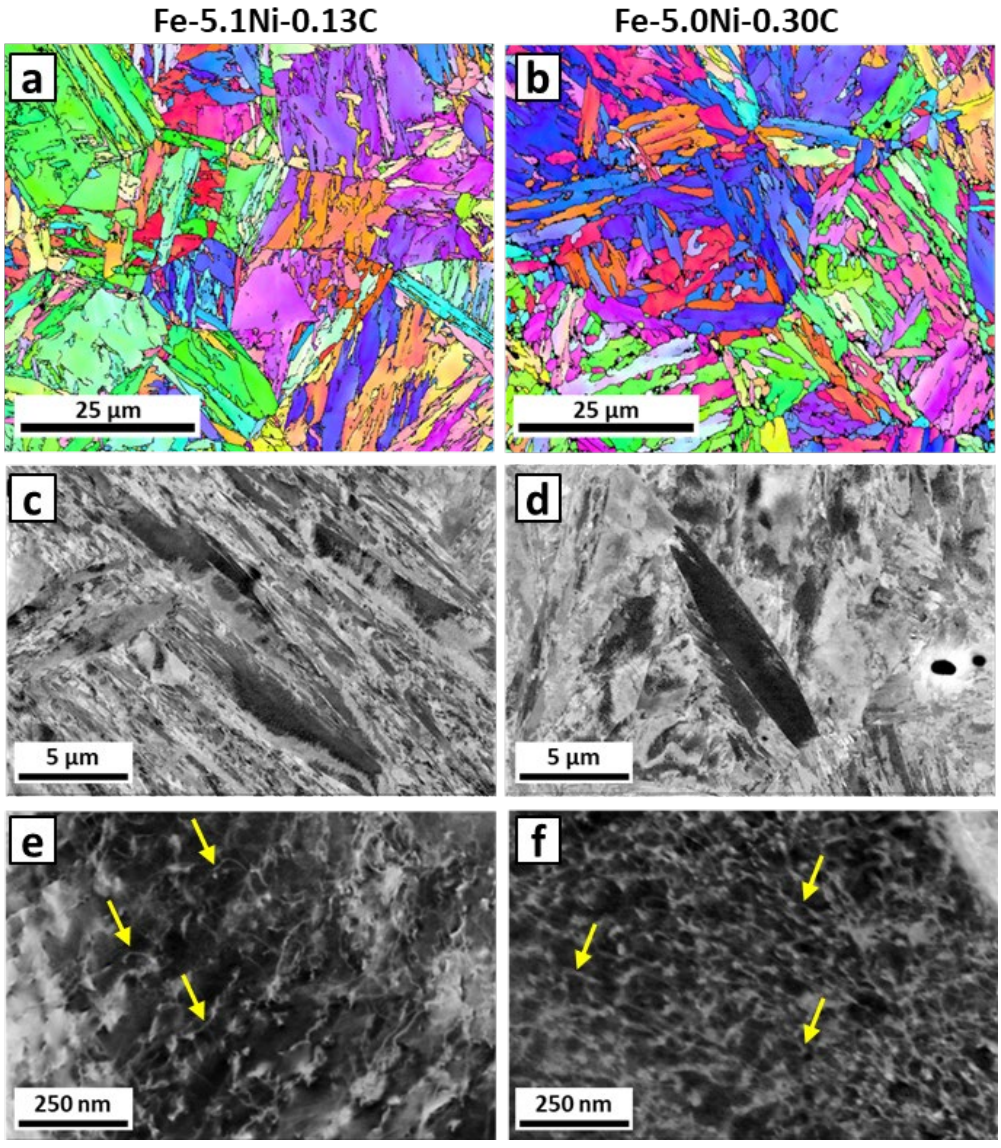

Figure 4.1: Inverse pole figure maps and ECCI images of the microstructure in both alloys at different length scales showing various orientations (a,b), different morphologies (c,d) and lattices (dark matrix) with high density of dislocations (bright features indicated by yellow arrows) (e,f) of the lath martensite.

ECCI confirms that both steels exhibit a complex and heterogeneous microstructure containing parallel stacked laths [199-201]. Lath morphologies were already studied in detail on the same material system [187], and have shown existence of a few coarse laths in a microstructure dominated by fine laths (also see Figure 4.1 c and d). A brief summary of the microstructural analysis performed previously on the same materials [187] is reproduced here for the convenience of the reader. Laths with a 2D projected size larger than 5 μm^2 were considered as coarse laths. The average area fractions of coarse laths were reported as 8.8% and 3.9% for Fe-5.1Ni-0.13C and Fe-5.0Ni-0.30C, respectively. The maximum width of the coarse laths was measured to be 3.5 μm, while the width of the fine laths varies between 50-500 nm (with an average of 200 nm). The microstructure of the alloy with the higher carbon exhibited a finer lath size, attributed to the restricted martensitic transformation at the higher carbon content [178]. The prior austenite grain size is about 25 μm in both alloys, and therefore the hierarchy in terms of packets and blocks should be comparable between the two alloys. More details about microstructural defects, such as dislocations, within the lath martensite are revealed in the higher resolution ECCI micrographs shown in Figure 4.1 (e and f). The lattice defects appear with a brighter contrast than the matrix in the ECCI micrographs. The dislocation networks are observed throughout the entire microstructure. In addition, this qualitative analysis of the dislocation structure already suggests a higher dislocation density in the Fe-5.0Ni-0.30C alloy as compared with its lower carbon counterpart.

The degree of lattice distortion as a result of the interstitial carbon atoms is studied by using x-ray diffraction (XRD). Figure 4.2 (g-i) shows the XRD results from the as-quenched samples, which include the peaks for martensite. In spite of the low amounts of alloying elements in the studied material, a small amount of retained austenite was detected in the spectrum. This has been observed in other studies [37, 41, 184, 185, 199, 201-205] by TEM where thin films of retained austenite between lath martensite were detected even after fast quenching. Higher resolution XRD scans were collected on 43-47° and 63-67° 2θ ranges for the (110) and (200) martensite peak positions, respectively. The total carbon content entrapped in interstitial lattice positions is not

sufficient to display the splitting of the (200) peak due to tetragonality of martensite. Also, autotempering occurs simultaneously during quenching [206-208]. This means that not all carbon atoms remain trapped in the lattice, but also decorate and pin dislocations and eventually form cementite precipitates nucleating from dislocation cores [208]. In the higher carbon alloy, the formation of carbon-rich clusters and transition carbides is additionally driven by spinodal decomposition at even smaller length scales (within the dislocation network) [208]. In general, the high carbon alloy experiences less autotempering during quenching due to the lower M_s temperature, so that the fraction of interstitially dissolved carbon atoms is higher than in the low carbon alloy. The slight shifts of the (200) peak to the right and the (110) peak to the left are attributed to the expansion and contraction of the crystal lattice along those directions during martensitic transformation, which is enhanced in the high carbon alloy. This indicates tetragonal distortion of the bcc structure particularly in the Fe-5.0Ni-0.30C alloy due to the elevated interstitial carbon content.

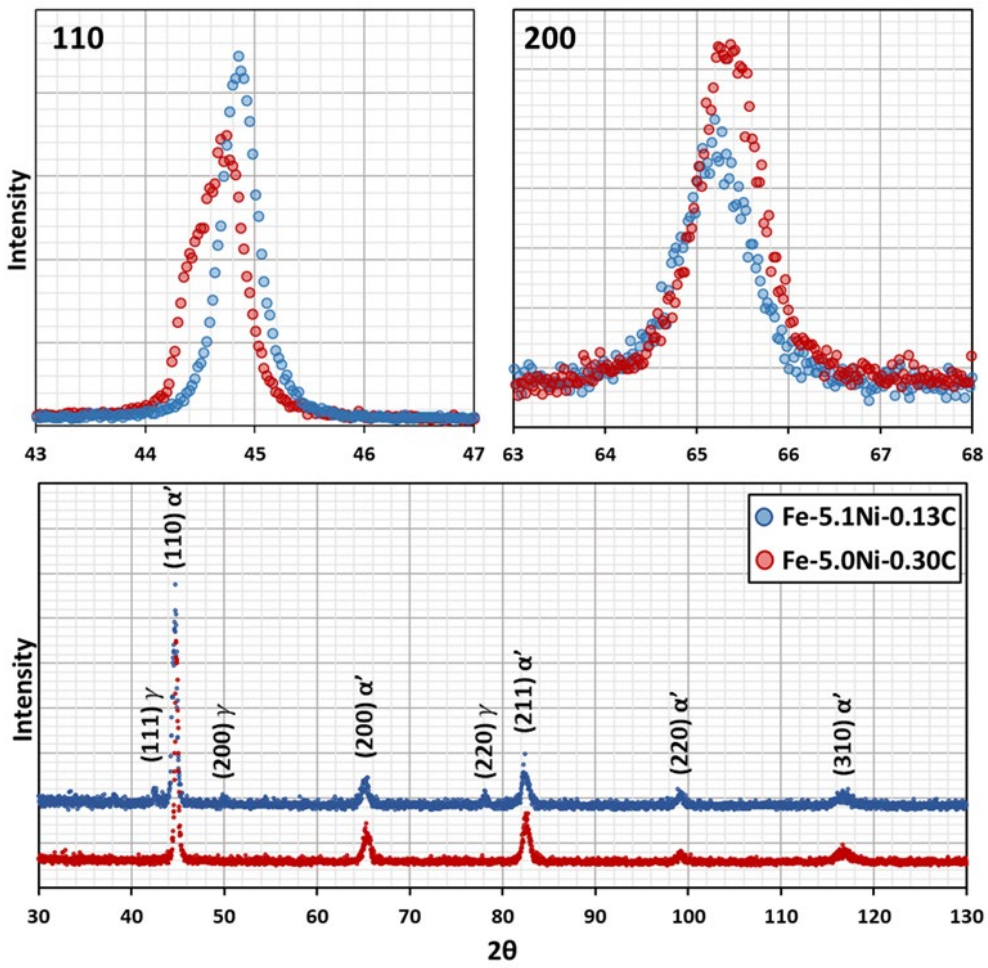

Figure 4.2: XRD plots from both materials and detailed scans on peaks (110) and (200) (g-i) showing shifts in the peak positions as a result of contraction and expansion of the lattice along [110] and [200] directions.

Examples of nanoindentation measurements obtained in this study using the 1, 16, and 100 μm indenter tip sizes are shown for both alloys in Figure 4.3. As discussed earlier, the transition from elastic to plastic regimes is not obvious from the load-displacement plots shown in Figure 4.3 (a-c). The details of the load-displacement curves at the very early stage of loading are magnified and shown in Figure 4.3 (d-f). These plots reveal a discernible difference in the load-displacement responses for both alloys, even at small indentation depths. However, the exact point of initiation of plastic deformation is still not easily identified from these plots. The elastic to plastic transition becomes obvious only after the data is corrected (i.e., zero-point correction [89]) and converted to

the indentation stress-strain curves shown in Figure 4.3 (g-i) using our recently developed protocols [89]. The elastic segments in the initial loading segments are highlighted in Figure 4.3 (d-f). The corresponding calculated values of the elastic moduli from these curves are also provided in the same figures. It is important to recognize that the very early segments of the measured load-displacement curves are excluded from the analyses as they do not match the Hertzian contact theory. This is because the contact in these very early segments is likely to be different from the ideal contact of smooth quadratic surfaces assumed in the Hertzian contact theory. Therefore, the concept of effective contact mentioned earlier is crucial for the proper analysis of the measured load-displacement curves. As mentioned earlier, the indentation yield strength is defined using a 0.002 plastic strain offset in these measurements, while the indentation work hardening rate is defined as the slope of a line fitted to the stress-strain data from the yield point to a plastic indentation strain of 0.015.

Since the martensitic microstructure exhibits a high degree of heterogeneity in terms of local carbon distribution, grain boundary density, dislocation density, crystallographic orientations (see Figure 4.1 and [187]) at the scale of the indentation probe volumes, it becomes essential to conduct multiple measurements at randomly selected locations on the sample. This allows us to arrive at a statistically meaningful comparison and interpretation of the effects of carbon on the measured indentation properties. The results from 30 nanoindentation tests per indenter tip size on each alloy are presented in Figure 4.4 (a-c). There is a clear overall trend in these results indicating that the Fe-5.0Ni-0.30C alloy (red) exhibits a higher indentation yield strength than the Fe-5.1Ni-0.13C alloy (blue). Also, the variance in the results is larger with the smaller indenter tip sizes. This variance can be attributed to a number of factors in the local microstructure including differences in carbon content, dislocation density, boundary density, and the crystallographic orientations of the laths [187].

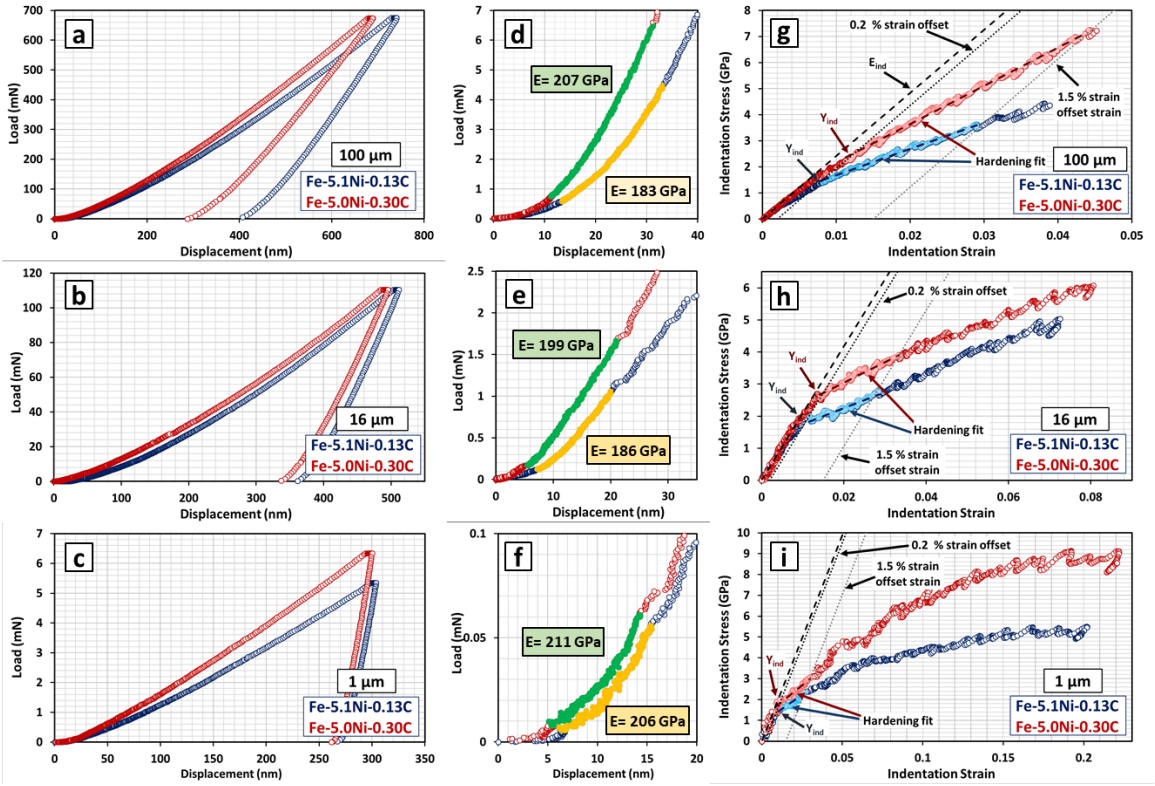

Figure 4.3: Examples of Load-displacement plots (a-f) using 1, 16, 100 µm indenter tip radius and indentation stress-strain curves (g-i) on both alloys: Fe-5.0Ni-0.30C (red) and Fe-5.1Ni-0.13C (blue). The highlighted segments in plots (d-f) indicate the elastic segment in load-displacement of each test.

The means and the standard deviations of the measured indentation elastic moduli (E_{ind}), indentation yield strengths (Y_{ind}) and indentation work hardening rates (H_{ind}) are summarized in Table 4-2. The averages are plotted against the estimated primary indentation probe volume in Figure 4.4 (d-f), where the primary indentation volume is estimated as a cylinder of diameter of $2a$ and the height of $2.4a$ [89]. Since the contact radius a evolves with increasing indentation depths, a separate estimation is carried out at each loading level (i.e. each indentation depth or load applied). Indeed, the contact radius is estimated as a part of computing the indentation stress and strain values using Equation (2.18) (for further details of these computations the reader is referred to Refs [57, 89]). The diameter of the primary indentation probed volume for 1, 16, and 100 µm indenter tip size was found to cover the range from 100 nm to 4 µm at the 0.002 offset yield point

on the indentation stress-strain curves. At an indentation plastic strain of 0.015 (note that the data between yield and 0.015 strain level is used to measure H_{ind}), the diameters of the probed volumes for the different indenter tip sizes cover the range from 140 nm to 11 μm. Clearly, these represent substantial ranges of microstructural features contained in the probed volumes which will be discussed in the following.

Table 4-2: Statistics (means and standard deviations) of the mechanical property measurements from spherical indentation on alloys Fe-5.1Ni-0.13C and Fe-5.0Ni-0.30C using different indentation tip radii

	Fe-5.1Ni-0.13C			Fe-5.0Ni-0.30C		
	100μm	**16μm**	**1μm**	**100μm**	**16μm**	**1μm**
Indentation Modulus (E_{ind}), GPa	192.1 ± 20.7	194.8 ± 18.1	200.8 ± 24.1	204.8 ± 23.9	204.2 ± 15.4	209.8 ± 26.4
Indentation Yield Strength (Y_{ind}), Gpa	1.71 ± 0.33	1.67 ± 0.30	1.53 ± 0.46	2.53 ± 0.38	2.43 ± 0.44	2.17 ± 0.53
Contact Diameter at Y_{ind} (2a), nm	4,187 ± 833	753 ± 140	115 ± 27	3,927 ± 863	739 ± 87	109 ± 24
Probed Volume at Y_{ind} (Vp) $\times 10^{-3}$, μm^3	77,387 ± 47359	442.8 ± 234.4	1.6 ± 0.1	64,409 ± 35,320	395.7 ± 144.7	1.4 ± 0.9
Indentation Work Hardening (H_{ind}), GPa	90.24 ± 17.10	51.84 ± 15.13	45.78 ± 12.50	132.72 ± 15.78	71.59 ± 14.82	58.20 ± 16.31
Contact Diameter at H_{ind} (2a), nm	11,263 ± 2434	1,712 ± 219	149 ± 30	9,576 ± 1,309	1,554 ± 238	141 ± 30
Probed Volume at H_{ind} (Vp) $\times 10^{-3}$, μm^3	1,537,622 ± 1,067,880	4,954.3 ± 1,856.4	3.5 ± 1.9	872,687 ± 367,645	3,792.2 ± 2,013.6	3.0 ± 1.9

Figure 4.4 (d-f) indicates that changing carbon content from 0.13% to 0.3% has a smaller influence on elastic modulus, but a larger influence on the indentation yield strength and indentation work hardening rate measured with all three indenter tip sizes. These increases are quantified and summarized in Figure 4.5. The ratios of the indentation moduli, indentation yield strengths and indentation hardening rates for the two alloys were measured to be in the ranges of 1-1.1, 1.4-1.5, and 1.2-1.5, respectively. These observations can be explained by the fact that the elastic properties are dominated by characteristics of the atomic bonding, while the plastic properties are controlled by the various defects in the microstructure that include interstitial C atoms as well as carbon

clusters or early stage transition carbides, dislocations and the low-angle lath and high-angle block boundaries. The higher dislocation density and interstitial carbon content, as well as the finer microstructure in terms of lath sizes in the alloy with the higher carbon content (see Figure 4.1 and [51]) are in line with the observed increases in the indentation yield strength and the indentation work hardening rates.

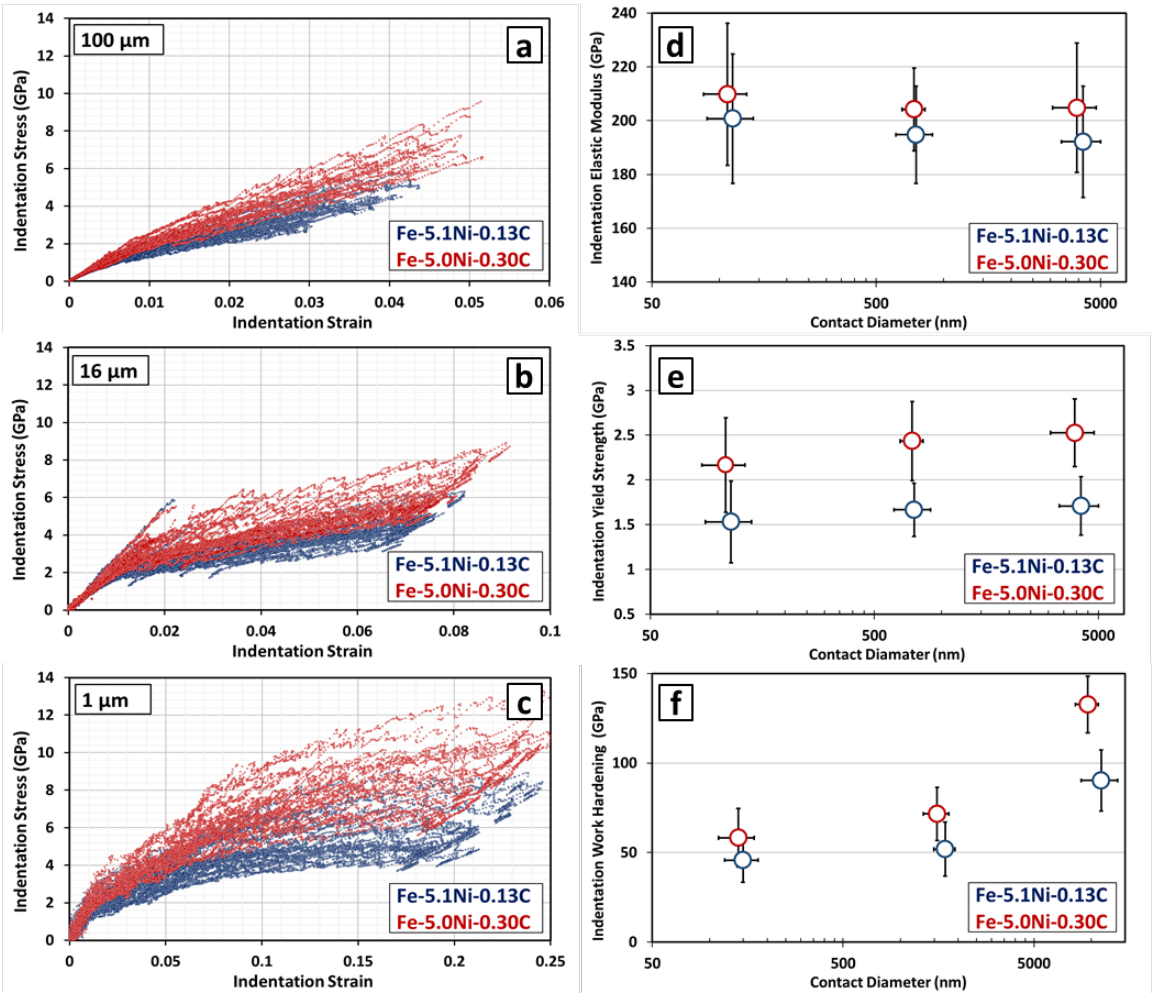

Figure 4.4: Multiple indentation stress-strain curves (a-c) from randomly selected locations capturing the variance in the measured responses using the different indenter tip radii in both sample alloys: Fe-5.0Ni-0.30C (red) and Fe-5.1Ni-0.13C (blue). The statistics (means and standard deviations) of extracted properties: indentation elastic modulus (d), indentation yield strength (e), and indentation work hardening rate (f) as a function of the primary indentation zone size.

An important observation from Figure 4.5 and Table 4-2 is the relative insensitivity of the indenter tip size on the measured indentation yield strengths. As mentioned earlier, a number of prior studies in literature [188-192] have reported increased hardness values with smaller indentation depths (and probe volumes). The results presented in this work show that the mean indentation yield strength obtained as 0.002 indentation plastic strain offset value is mostly insensitive to the indenter tip size. The very small decrease in the measured indentation yield strengths with the smaller indenter tips lies within the range of measurement variance. The measurements obtained in this work strongly suggest that the previously reported indentation size effect in literature (i.e., higher hardness at smaller indentation depths) is most likely a consequence of the analyses protocols employed in those studies. As mentioned earlier, most previous studies have reported hardness values (as opposed to the indentation yield strengths reported in this work) that correspond to non-standard values of imposed plastic deformation in the indentation experiment.

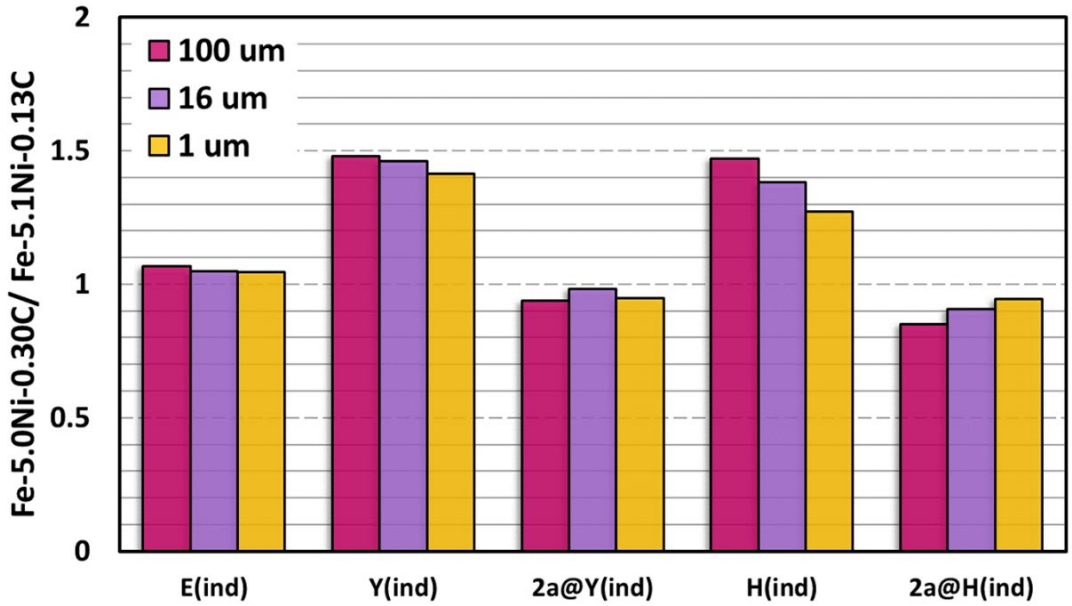

Figure 4.5: Effect of carbon content on the mechanical responses of lath martensite in alloys Fe-5.1Ni-0.13C and Fe-5.0Ni-0. 30C. The ratio of the extracted values, from left to right, indentation elastic modulus, indentation yield strength, the diameter of the indentation primary zone at yield, Indentation work hardening, and the diameter of the indentation primary zone at 0.015 plastic strain.

Figure 4.6 (a and b) shows all indentation stress-strain plots for different indenter sizes for both alloys. This provides a visual overview of the variance of the nanoindentation data as well as the indenter size effect on the material responses. Figure 4.6 also reveals a significant influence of the indenter tip size on the work hardening rate. To obtain a better insight into this effect, one needs to examine these in the context of the length scales of the microstructural features inside the primary indentation zone. As discussed before, the primary indentation zone can be approximated as a cylinder with diameter and height of $2a$ and $2.4a$, respectively [89]. The probed volumes for 1, 16, and 100 μm indenter tips at the indentation yield strength and 0.015 indentation plastic strain are schematically depicted on a representative ECCI micrograph of the martensitic microstructure for the Fe-5.0Ni-0.30C alloy, in Figure 4.6 c and d, respectively. This schematic illustrates that the primary indentation zone sizes at yield point and 0.015 plastic strain are typically smaller than the average lath thickness for the measurements with the 1 μm indenter tip size. This is because the indented zone size in these experiments is of the order of 112 ± 25 nm at yield (0.002 indentation plastic strain) and 146 ± 30 nm at 0.015 indentation plastic strain, while the average fine lath size is about 200 nm [187]. Therefore, the measurements with the 1 μm indenter tip are most likely from a single martensite lath, and in some cases might have included a single most probably low-angle lath boundary in the indented zone. The diameter of the indentation probed volume for the 16 μm indenter tip changes from 739 ± 87 nm to 1554 ± 238 nm, which is still in the order of the average lath size (including fine and coarse laths) and possibly includes a handful of low angle boundaries. In other words, the probed material volumes in the measurements with both 1 and 16 μm indenter tips are mostly influenced by a small number of interfaces with mostly low misorientations. Therefore, it is not surprising that the averaged mechanical responses for both indenter sizes are very similar to each other, although the measurements with the 1 μm indenter tip exhibited a higher variance. On the other hand, the measurements obtained with the 100 μm indenter tip (shown in magenta in Figure 4.6) show a significantly higher strain hardening rate (see

also Figure 4.4 f and Table 4-2). It should be noted that the 100 μm indenters probed a volume which is larger than the average martensite block size (see Figure 4.6 d). The probed material volumes with the 100 μm indenter tip corresponded to length scales of about 4 μm at indentation yield to about 10 μm at an indentation plastic strain of 0.015. At these length scales, the indentation primary zone is likely to contain several high angle boundaries which are effective in impeding dislocation transmission [209]. It should also be noted that the high angle grain boundaries are likely to serve as potent dislocation sources (cf. [91]) and can contribute in a very effective manner to the higher hardening rates measured with the larger indenter tips. Dislocation density and carbon distribution, however, equally affect indentation measurements at all scales studied, as the dislocation cell size and carbon network size are significantly smaller than all probed volumes.

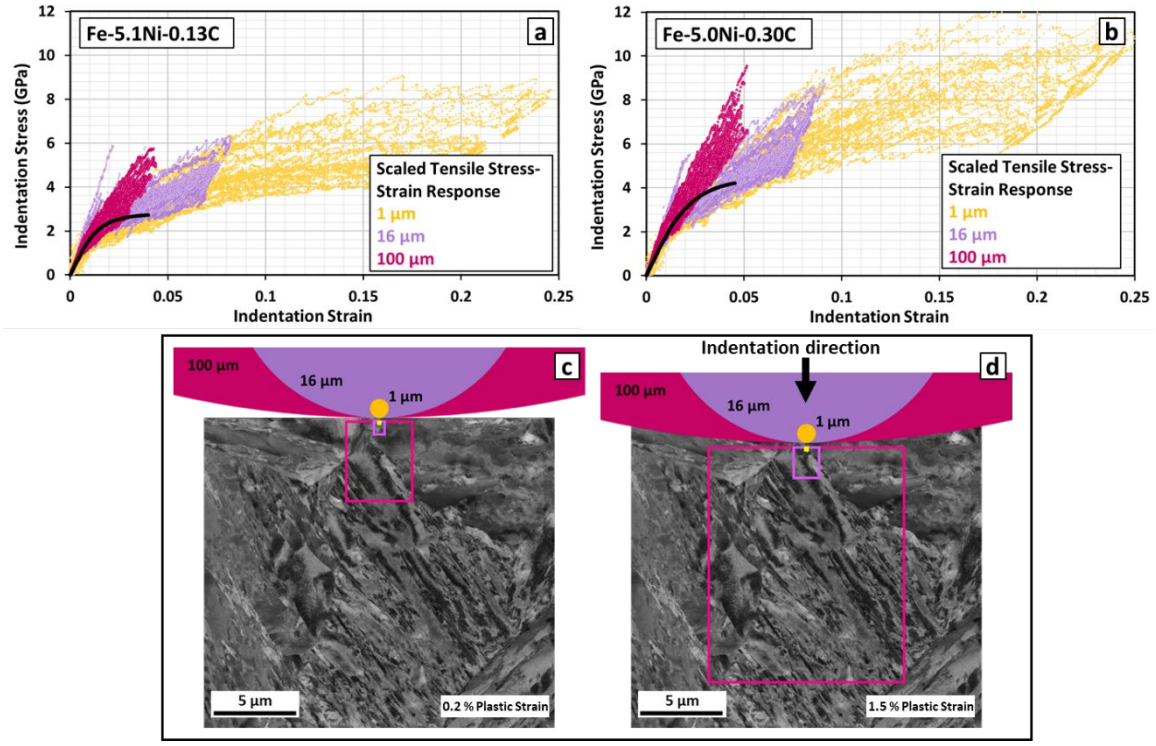

Figure 4.6: Multiple indentation stress-strain measurements at different lengths scales. Results from 1, 16, 100 µm indenter tip sizes are plotted in orange, purple, and magenta (a, b). The schematic of the indentation zone size for each indenter tip in relation to the microstructural details for a vertical indentation direction is shown in the bottom with the same color code for Fe-5.0Ni-0.30C sample at two loading levels, when the yield occurs (c), and when 1.5% plastic strain is achieved (d). The width and height of the rectangular is $2a$ and $2.4a$, respectively, where a is the contact radius.

Another important observation in this study is the presence of pop-ins in some of the indentation tests. Pop-in events have been reported previously [91, 111-113, 116] in load-control indentation tests, defined by a sudden jump in the displacement at roughly constant load. In prior studies using the same spherical indentation protocols used here, pop-ins were observed only in the fully-annealed metal samples studied with the smallest indenters [91, 113, 136, 210, 211]. They disappeared when the indenter tip size was increased or when the samples were given small amounts of plastic deformation [211]. As a result, the pop-ins observed in these studies were attributed to the activation of dislocation sources in the primary indentation zone [91, 111-113, 212,

213]. However, the mechanism behind pop-ins observed in the present study must be very different, because lath martensite exhibits a significant density of pre-existing dislocations (see Figures 1e and 1f).

Another type of pop-in reported in literature is the grain boundary pop-in observed in indentation tests conducted near grain boundaries [113-119]. It is generally believed that these are caused by the pile-up of the dislocations produced in the primary indentation zone at the grain boundaries and their eventual transmission through the grain boundary. However, these grain boundary pop-ins were never observed in any of the previously reported spherical indentation measurements.

In the present study, pop-ins were observed in the measurements conducted with the 1 μm and 16 μm spherical indenter tips. Typical examples are shown in Figure 4.7. These are identified as displacement bursts exceeding 1.5 nm. Interestingly, these pop-ins are distinctly different from those reported in the earlier studies on the fully annealed samples [91, 113, 136, 210, 211]. First, the pop-ins observed in the present study were significantly smaller. For example, the pop-ins observed in the fully annealed samples exhibited displacement bursts of 10-150 nm and 5-40 nm in the tests conducted with the 1 μm and 16 μm spherical indenter tips, respectively. However, the pop-ins observed in the present study exhibited displacement bursts of 1-4.5 nm and 1.5-7.5 nm in the tests conducted with the 1 μm and 16 μm spherical indenter tips, respectively. Not only are the displacement bursts significantly smaller, they also exhibited a completely different trend with the increase in the indenter tip size. The displacement bursts in the current study increase with indenter tip size, while the opposite was observed in the previous study. Second, the pop-ins in the 1 μm spherical indentation tests were observed after a significant amount of plastic strain was introduced in the primary indentation zone. These observations clearly suggest that the pop-ins are not caused by the lack of dislocation sources.

Instead, the root cause for pop-ins seems related to the effect of grain boundaries with dislocation pile-up and eventual transmission at the lath interfaces or block boundaries. The contact

radius and the indentation stress are extracted at each pop-in event in the tests conducted with the 1 μm and 16 μm indenter tips and plotted in Figure 4.8. The contact radius associated with the pop-ins corresponds well with the average lath thickness. The dislocations are expected to interact with the dislocation arrays along lath boundaries before they are transmitted into in the neighboring lath. The range in displacement bursts between 1 and 7.5 nm might be related to the difference in dislocation transmission across high- and low-angle boundaries. High-angle block boundaries effectively hinder dislocation transmission due to the mismatch of adjacent slip planes, while low angle boundaries present a lesser obstacle to dislocation transfer [67, 75]. Another observation from Figure 4.8 is that the indentation stress for the pop-in events is higher for the tests with the 1 μm indenter tip compared to the 16 μm indenter tip. This can be explained by the fact that the stress gradient in the tests with the 1 μm indenter tip is significantly sharper compared to the tests with the 16 μm indenter tip. In other words, the stress fields with the smaller indenter decay extremely fast and consequently need to rise to higher levels before successfully transmitting the dislocations across the lath boundaries. It is also worth noting that pop-ins were not found in the tests conducted with the 100 μm indenter tip. It is reasonable that pop-ins disappeared in the indentation tests with the 100 μm indenter tip as one should expect a multitude of pop-in events occurring continuously in different parts of the indentation primary zone. The measured load-displacement curve simply reflects an averaged (smoother) response, where the individual pop-ins are no longer discernable. All the observed pop-ins in our tests are therefore consistent with the notion of grain boundary pop-ins.

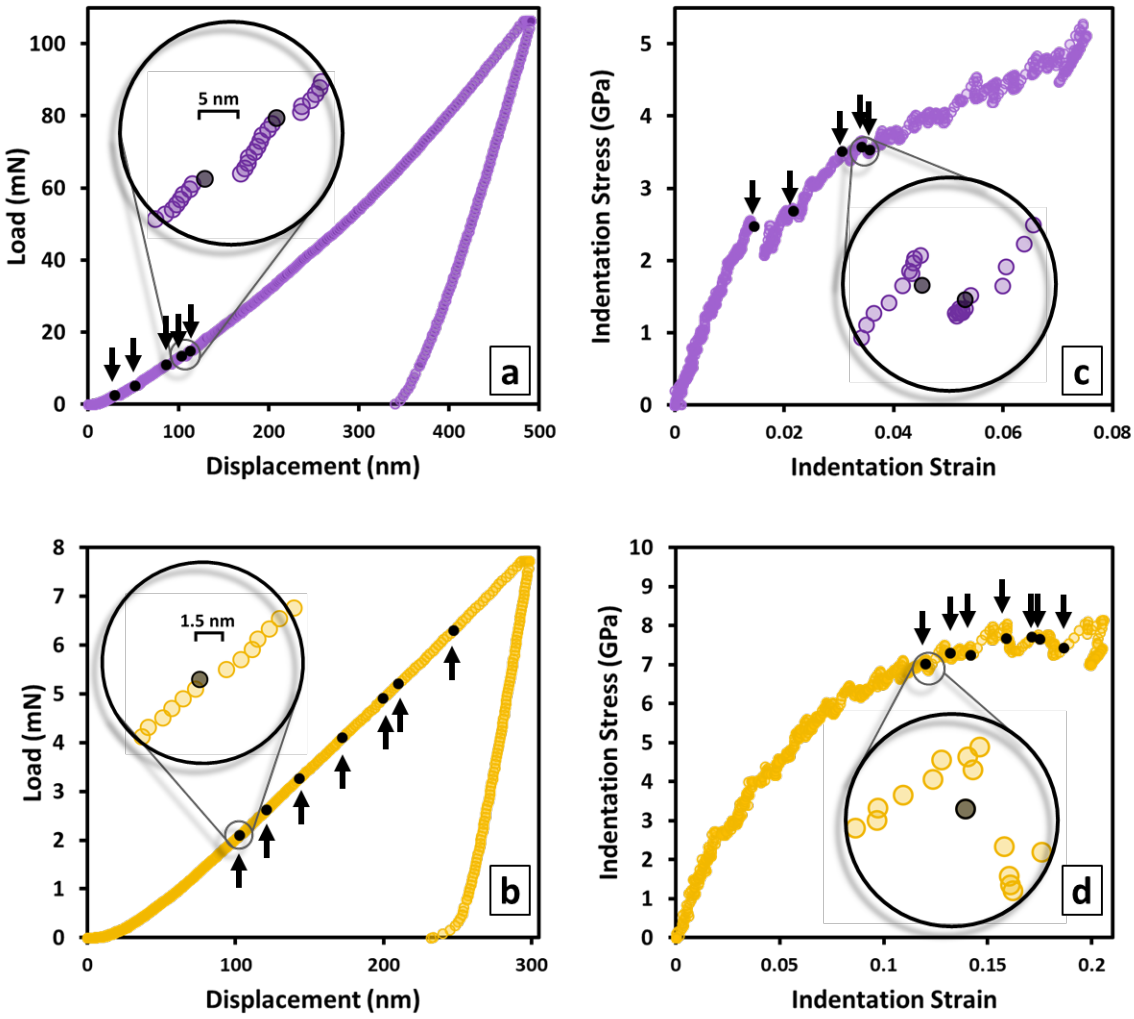

Figure 4.7: Examples of pop-ins in the tests conducted with the 1 and 16 µm indenters are presented as load-displacement curves (a and b) and their corresponding indentation stress-strain curves (c and d). The black arrows point to the detected pop-ins.

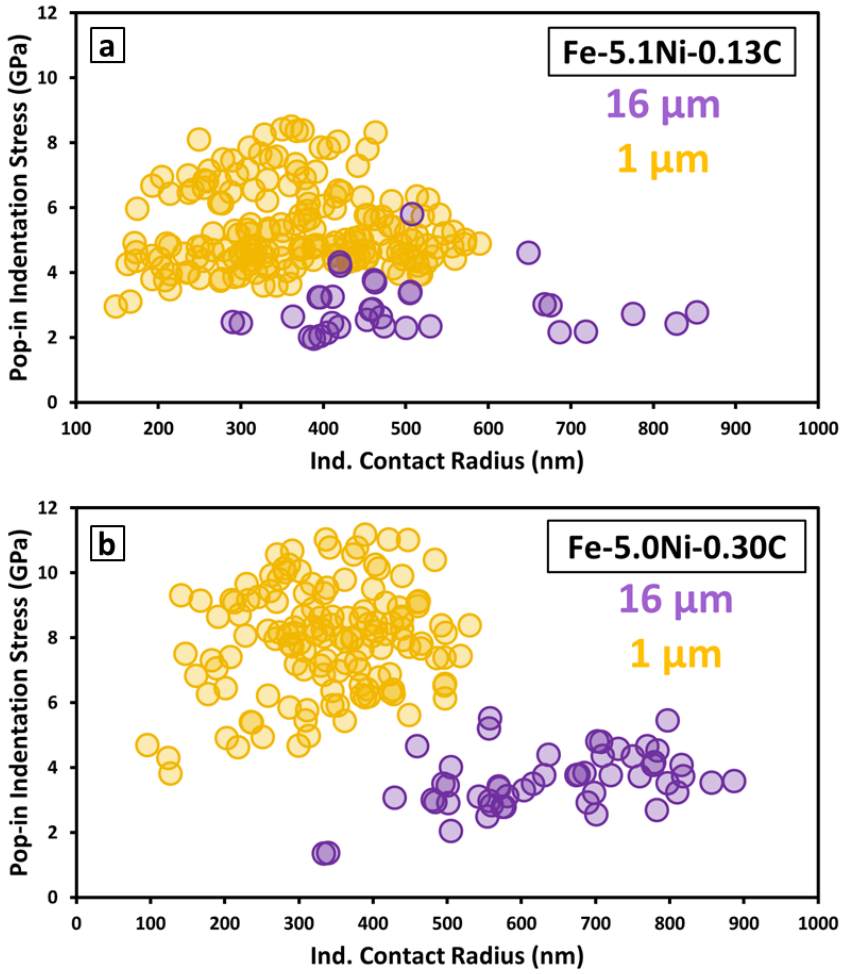

Figure 4.8: Indentation stress and contact radius for each detected pop-in in (a) Fe-5.1Ni-0.13C and (b) Fe-5.0Ni-0.30C alloys.

In addition to nanoindentation tests, uniaxial stress-strain measurements were obtained for both alloys from standard tensile tests which are presented in Figure 4.9 a. Two tensile tests were conducted for each alloy. The Fe-5.1Ni-0.13C alloy exhibits an average uniaxial yield strength of 1029 MPa, while the corresponding value for the Fe-5.0Ni-0.30C alloy is 1319 MPa (Figure 4.9 a). To maintain consistency with the indentation measurements, the work hardening values are extracted from the early parts of the stress-strain curves. Using the stress-strain curves after the yield point and up to 0.015 plastic strain results in work hardening rates of 22.8 GPa and 32.6 GPa for Fe-5.1Ni-0.13C and Fe-5.0Ni-0.30C, respectively. The ratios of the yield strengths and the work

hardening rates for the two alloys (expressed as values for Fe-5.0Ni-0.30C over the values for Fe-5.1Ni-0.13C) are 1.3 and 1.4, respectively. Note that these ratios are in excellent agreement to the corresponding ratios obtained from nanoindentation data (see Figure 4). This agreement in the ratios of the measured properties proves the accuracy and reliability of the spherical indentation stress-strain protocols employed in this work.

It should be clear that the uniaxial stress-strain data cannot be compared directly with the indentation stress-strain data, as these impose very different plastic deformation fields in the sample. In a recent work based on finite element simulations employing isotropic plasticity models, Patel et al. [97] suggested scaling factors of 2.2, 2.0, and 1.3 for the stress, elastic strain, and plastic strain, respectively. These factors were used to scale the measured tensile stress-strain curves in Figure 8a to indentation stress-strain curves shown in Figure 4.9 b. The indentation stress-strain curves presented in Figure 4.9 b can be interpreted as data from indentation measurements in substantially large indentations, within the assumptions of an isotropic plasticity model for the effective material response. The scaled tensile stress-strain curves are superimposed on the indentation measurements in Figure 4.6 a and b. It is seen that the scaled indentation stress-strain responses from Figure 4.9 b are in reasonable agreement with the nanoindentation measurements for both alloys, at least up to small plastic strains.

The scaled indentation yield strengths extracted from Figure 4.9 b are 2090 and 2612 MPa for the Fe-5.1Ni-0.13C and the Fe-5.0Ni-0.30C alloys, respectively, and are 22% and 3% higher than the indentation yield values measured with the 100 μm indenter tip for the Fe-5.1Ni-0.13C and the Fe-5.0Ni-0.30C alloys, respectively. The scaled work hardening rates extracted from Figure 8b for the two alloys are 43.3 and 68.2 GPa, which are very close to the average values measured with the 1 μm and 16 μm indenter tips. However, the hardening rates measured with the 100 μm indenter tip are significantly higher compared to those measured in tension.

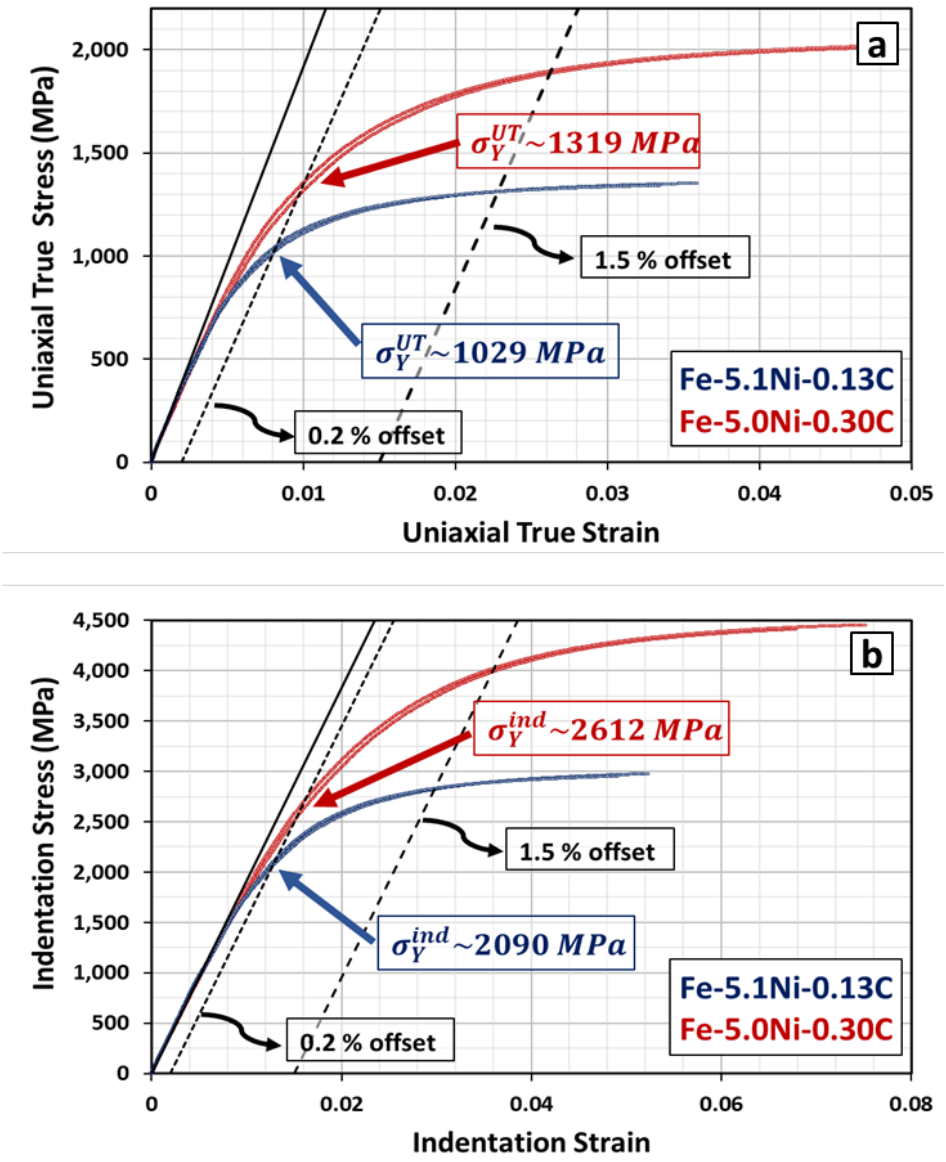

Figure 4.9: Mechanical responses of Fe-5.1Ni-0.13C and Fe-5.0Ni-0.30C alloys from uniaxial tension test (a) and the same results after conversion using scaling factors to obtain indentation stress and indentation strain (b).

The comparisons presented above between the properties measured in indentation and tension tests provide several key insights. They demonstrate good agreement for the measured yield strengths and elastic moduli in the different testing modes. To this end, the indentation protocols developed and presented in this paper provide a new set of reliable and robust tools to assess mechanical properties of hierarchical microstructures such as lath martensite in steels. Yet, it is

clear that the hardening rates measured with the 100 μm indenter tip are significantly higher compared to those measured with tensile tests. There could be a number of reasons for this: (i) the deformation imposed in indentation is indeed highly heterogeneous and exhibits strong gradients. Consequently, it is possible that the indentation hardening rates will always be higher than those measured in tension. (ii) the tensile tests were conducted with a nonstandard sample geometry where the gage length/width ratio was slightly less than 4.0. This might have introduced a small inaccuracy in the measured tensile stress-strain curve. (iii) Tensile stress states might promote early damage initiation and result in a lower hardening rate compared to indentation tests with a significantly higher negative hydrostatic stress component. (iv) The discrepancy in work hardening rates measured with indentation and tensile testing shows that the rather simplistic scaling approach cannot sufficiently account for the complex plastic response of lath martensite at the length scale of multiple prior austenite grains that was previously analyzed by the authors [65].

4.1.5. Summary

The mechanical properties of lath martensite in Fe-5.1Ni-0.13C (wt.%) and Fe-5.0Ni-0.30C (wt.%) alloys were systematically investigated at multiple length scales with spherical nanoindentation stress-strain protocols as well as standard tensile tests. Consistent results from the indentation measurements with indenter tip radii ranging between 1 μm and 100 μm as well as from the standard macroscale tensile tests attest to the reliability of the applied indentation protocols for studying hierarchical microstructures such as martensitic steels. The results provided reliable data on the indentation yield strength of lath martensite as a function of carbon content with only 3% and 22% deviations compared with tensile testing of the Fe-5.1Ni-0.13C (wt.%) and Fe-5.0Ni-0.30C (wt.%) alloy, respectively. The work hardening rates measured in indentation tests with the 100 μm indenter tips are significantly higher than those measured with the 1 μm and 16 μm indenter tips, as well as those measured in tension tests. The discrepancy in work hardening measured with different indenter tip sizes is attributed to the presence of high angle block boundaries in the 100 μm

indenter tip probed volumes. The discrepancy between values obtained by 100 μm indentation and tensile tests is regarded as an inherent limitation due to the microscopic probe volume compared with macroscopic tensile samples. Yet, both indentation and tensile results consistently showed that increasing the carbon content from 0.13 to 0.3 wt.% increased the yield strength by ~42-48% and the work hardening by ~27-47%, while the elastic modulus showed a small increase of only ~5%.

The level of consistency achieved in this study suggests that the indentation size effects on indentation yield strengths reported in prior literature are largely a consequence of the analysis protocols employed in those studies. The higher spread in the indentation data at lower length scales is attributed to the heterogeneity of the microstructure in terms of lath size, dislocation density and carbon distribution. Therefore, a sufficiently large indenter tip is required to obtain the bulk response from the indentation measurements.

4.2. Establishing process-structure-property linkages in multiphase metals: Application to dual-phase steels

4.2.1. Introduction

The main goal of this work is to explore the viability of high throughput experimental assays for establishing PSP linkages in multiphase polycrystalline metals, while utilizing small sample volumes and leveraging some of the recent advances described earlier (i.e., spherical microindentation stress-strain protocols and the framework of 2-point statistics). We have selected DP steels for this study because of their importance to several advanced technologies, owing to their excellent combination of continuous yielding behavior, high tensile strength, high work-hardening rate, and good ductility [38, 41, 45, 47, 51, 62, 63, 66, 166-174]. These properties are generally achieved in DP steels through a special heat treatment process called intercritical annealing [36, 52, 64, 65, 67, 167, 171, 214] during which the material is heated up to the austenite/ferrite region, held for a certain amount of time, and quenched to room temperature. Intercritical annealing results in formation of hard particles of martensite (α') in a soft matrix of ferrite (α) grains. This step is usually followed by additional cold work and heat treatment called bake hardening (BH [50, 66, 166, 169, 172-174, 214-222]; cf. Figure 4.10) to achieve the desired combination of mechanical properties. The main mechanisms involved in this overall thermomechanical process are as follows: (i) Introduction of mobile dislocations in ferrite grains at the vicinity of α/α' interfaces ([47, 62, 67, 166, 169, 170, 216, 223-225]; see Figure 4.10 b), generally attributed to the volumetric plastic strains induced during the austenite to martensite transformation that occurs during the quenching from high temperature. This hypothesis is supported by transmission electron microscopy (TEM) observations [66, 172, 223, 224, 226] of higher densities of mobile dislocations in the ferrite matrix close to α/α' interfaces and the continuous yielding behavior exhibited by the DP steels. (ii) Formation of tangled networks of dislocations during the imposed plastic deformation, resulting in higher work hardening rates [166, 168, 172, 217, 223, 224] (see Figure 4.10 c). (iii) Pining of dislocations, relieving residual stresses,

and tempering martensite during the bake hardening process through diffusion of carbon atoms [66, 169, 170, 172, 173, 216-219, 221-223, 227] (see Figure 4.10 d). As one might expect, the final properties exhibited by DP steel are critically dependent on the extent of the different mechanisms described above, which in turn depend critically on the process parameters employed in the production of the DP steel.

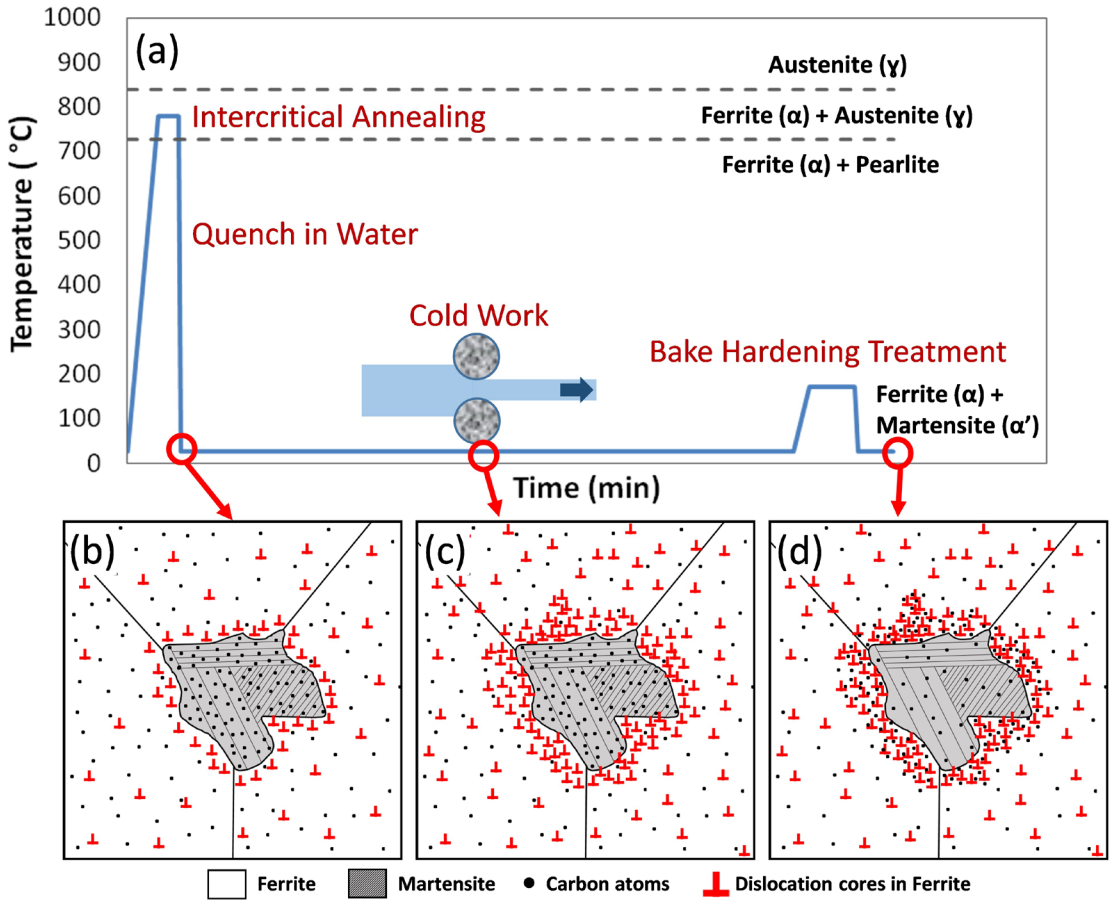

Figure 4.10: Schematic of a dual phase steel processing path and the expected strengthening mechanisms in each step of the thermo-mechanical process.

It is therefore clear that the process space (this is the set of all combinations of process parameters that could be utilized) to be explored in optimizing the set of final properties of interest in DP steels is extremely large. Consequently, high throughput assays mentioned earlier, if successfully employed, could produce dramatic acceleration in the deployment of these alloys in

emerging technologies. In this work, we have formulated a foundational framework for the development of high throughput assays for establishing PSP linkages in advanced structural metals and alloys, and demonstrated its successful application to a selected process space in DP steels.

4.2.2. Sample Prototyping

The first step in the assays described in this paper is the high throughput prototyping of a sample library. Since our intent is to use indentation techniques for measuring plastic responses, we need to produce only small quantities of the material (no significant stipulations on sample shape either) for each selected material chemistry and/or process history. In this study, we decided to select a single chemical composition, and allow for variations in the thermo-mechanical processing history.

A four millimeter strip of low carbon steel with a chemical composition (in wt.%) of 0.15C, 1.4Mn, 0.04P, 0.04S was secured and used in this study. The strip was cut into coupons of 10 mm × 20 mm × 4 mm. All of the coupons were heat treated at 450 ºC for 2 hours in order to produce an annealed microstructure, which then served as the starting material for the study described here. Table 4-3 (cf. Figure 4.10) summarizes the different processing histories included in this study, which were selected following the studies published in prior literature [38, 45, 47, 50, 51, 63-65, 67, 169, 170, 172, 173, 216, 228-232]. In the intercritical annealing process, the samples are heated to the specified temperature in a salt bath furnace (taking them into the austenite/ferrite region), held for 4 minutes, and quenched in an oil bath. Subsequent to the intercritical annealing, plane strain deformation was applied by rolling, and was followed by bake hardening at 170 ºC for 20 minutes and quenching in water to the room temperature. As described in Table 4-3, three different intercritical annealing temperatures (750, 780, and 810 ºC) and three amounts of total thickness reduction (0, 5, and 10%) were selected for this study. This resulted in nine different processing conditions, with the sample labelling (see Table 4-3) capturing the processing history information. As an example, sample 750-05-170 indicates an intercritical annealing temperature of 750 ºC and 5% thickness reduction, followed by bake hardening process at 170 ºC for 20 minutes.

Table 4-3: Sample library and the labelling scheme employed in this study. The label includes information on intercritical annealing temperature, amount of cold work. and bake hardening temperature.

Sample code	Intercritical annealing temperature (°C)	Cold work -Thickness reduction (%)	Bake hardening at 170 °C for 20 min
750-00-000	750	0	×
750-05-170	750	5	✓
750-10-170	750	10	✓
780-00-000	780	0	×
780-05-170	780	5	✓
780-10-170	780	10	✓
810-00-000	810	0	×
810-05-170	810	5	✓
810-10-170	810	10	✓

It is emphasized here that the time and effort expended in sample prototyping for the present study are minimal because the assays we intend to use do not pose stringent requirements on either the size or the shape of material volumes to be produced in each different processing history. In the present study, all of the sample prototyping was completed by one person in about 100 hours.

4.2.3. Spherical Microindentation Stress-Strain Protocols

As mentioned earlier, most of the prior work on indentation stress-strain curves has been focused on evaluating the plastic response at length scales that were significantly smaller than the grain size [53, 55, 56, 58-60]. Only recently, these protocols have been extended to microindentation, where the length scales correspond to several grains (about 10-1000) in the indentation zone [95]. For microindentations conducted in the present study, we utilized a customized Zwick-Roell Z2.5 hardness tester with a 6.35 mm radius tungsten-carbide spherical tip. A constant crosshead speed of 0.1 mm/min was utilized in all the tests reported here.

An example indentation stress-strain curve produced in this work is plotted in Figure 4.11 (b), which corresponds to sample 750-10-170. In this test, there were 20 unloading segments. The sample elastic modulus, E_S, is estimated from the initial elastic loading segment (shown highlighted in red in Figure 4.11 (a)). The sample Young's modulus estimated from this indentation measurement is 207.8 GPa. The indentation yield strength defined based on 0.2% offset on the indentation stress-strain curve using an indentation modulus of $\frac{E_S}{1-\nu_S^2}$, was estimated to be 1191.2 MPa for this sample. Indentation results from the multiple tests (at least 10 tests on each sample) conducted in this work are summarized in Table 4-4. The average Young's modulus for all indentation measurements on all samples was 201.4 GPa with a standard deviation of 14.2 GPa, which compares well with reported Young's modulus in literature for steel from conventional tensile testing [233]. It is important to recognize that the indentation zone in the experiments reported here is sufficiently large to include multiple microstructural features, including ferrite and martensite regions. This is illustrated in Figure 4.12 for sample 750-00-000, where the estimated indentation zone sizes are delineated both at yield and at the end of the indentation test. The solid line circle in Figure 4.12 (a) shows the estimated indentation zone size at the end of test, and the dashed line circle corresponds to the zone size at the indentation yield point. The image on right, Figure 4.12 (b), is an SEM image taken on the same sample, whose size was made to correspond to the contact area at indentation yield. As one can see, the indentation area is large enough to justify the measurements reported here as measurements of the bulk mechanical response of the sample, especially keeping in mind that multiple indentations are conducted on each sample and an average is reported for all indentations conducted on the sample (see Table 4-4). An estimate of the number of grains in the indentation zone can be obtained assuming a cylindrical primary indentation zone of radius a and height $2.4a$ [89]. The contact radii a at the yield point are listed in Table 4-4 for all tests. Considering the average grain size (30 μm) for the material tested and an

average contact radius at yield in the range of 142-182 µm (see Table 4-4), the number of grains in the primary zone is estimated to be in the range of 190-400 grains.

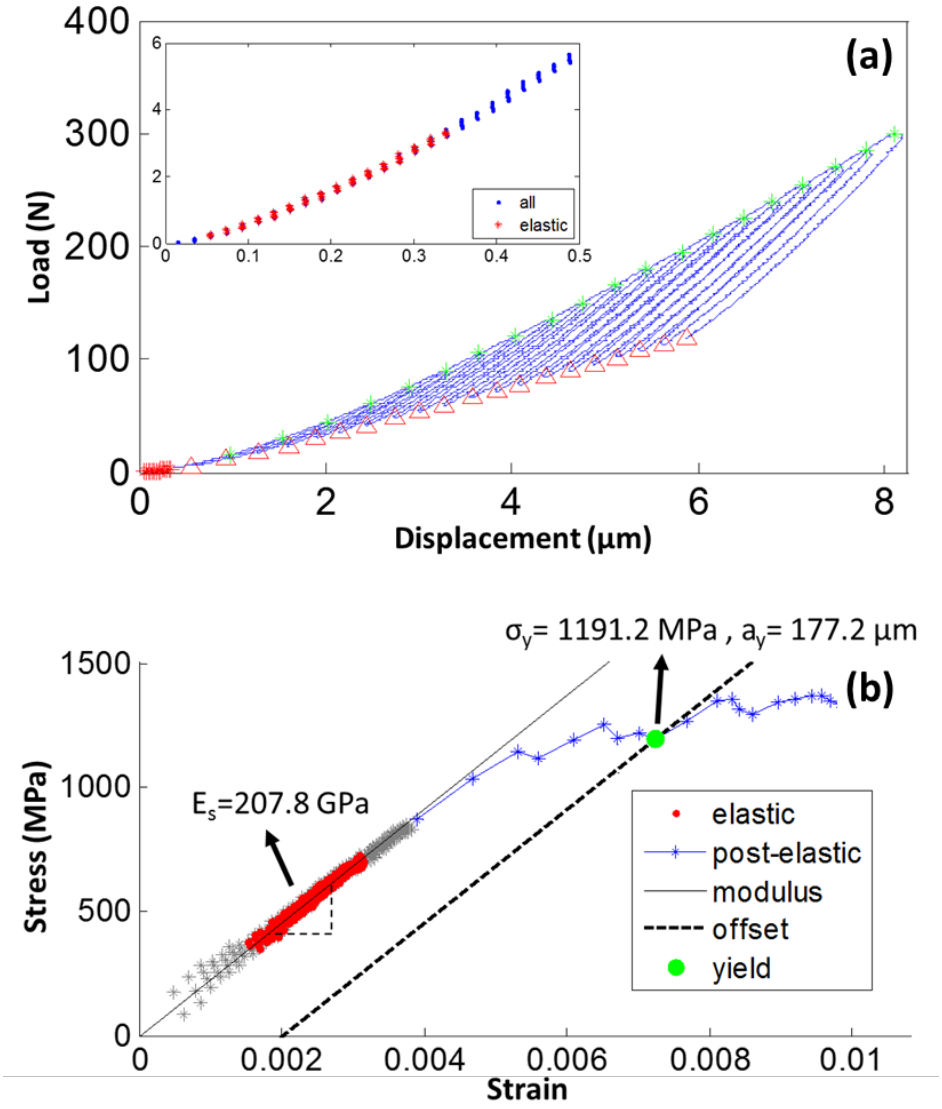

Figure 4.11: Example microindentation load-displacement curve, and indentation stress-strain curve for a test on sample 750-10-170. The red data corresponds to the initial elastic segment used to determine the effective modulus.

Table 4-4: Comparison of the indentation yield strength, the indentation elastic modulus, and the contact area at yield point between samples subjected to different thermo-mechanical treatments. At least ten measurements were made on each sample.

Sample code	Average indentation yield strength (MPa)	Average indentation elastic modulus (GPa)	Radius of the contact area at yield point (μm)
750-00-000	899.5 ± 62.9	174.5 ± 25.3	142.3 ± 7.0
750-05-170	950.4 ± 29.7	193.4 ± 23.3	166.7 ± 13.2
750-10-170	1100.9 ± 130.3	200.9 ± 22.3	176.2 ± 11.5
780-00-000	1097.7 ± 41.6	216.8 ± 23.3	165.7 ± 14.8
780-05-170	1299.4 ± 68.7	209.6 ± 15.4	178.1 ± 17.7
780-10-170	1336.3 ± 69.5	201.9 ± 16.7	181.3 ± 14.2
810-00-000	1168.6 ± 186.8	188.5 ± 14.7	153.3 ± 10.9
810-05-170	1340.4 ± 130.9	219.2 ± 14.5	169.3 ± 10.2
810-10-170	1506.5 ± 132.3	207.6 ± 9.7	180.5 ± 15.1

It is clear from Table 4-4 that the strength of the DP steel is largely controlled by the amount of both martensite and the imposed cold work. Increasing the amount of martensite (by means of quenching from higher intercritical annealing temperatures) results in strengthening of the DP steel. For example, the indentation yield strength, σ_Y^{ind}, increases from 899.5 ± 62.9 MPa to 1168.6 ± 186.8 MPa, when the quenching temperature is increased from 750 ºC to 810 ºC. The same trends can be seen even after 5% and 10% cold work and bake hardening were applied. These trends are consistent with the observed results in literature [45, 51, 66, 169, 174, 218, 219, 221, 230]. Although, it is possible to establish suitable conversion factors to estimate uniaxial yield values from the indentation yield values [100], this was not pursued in the present work as the focus in this work is on the establishment of high throughput assays.

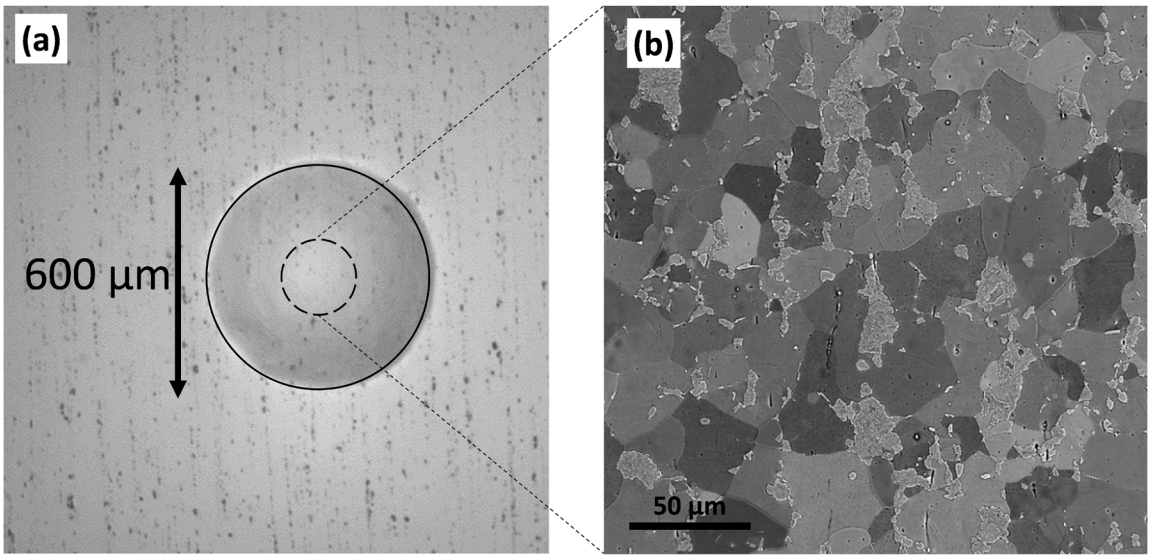

Figure 4.12: a) An optical micrograph showing the size of indentation after unloading, dashed line circle shows the estimated size of the contact area at yield. b) A representative BSE image with the same size as the area indicated by the dashed line.

It is emphasized here that the sample preparation for the microindentation tests reported here is identical to the sample preparation used for microstructure characterization (described next). In other words, the same sample preparation is used for both aspects of the study, leading to substantial economy in both time and effort expended.

4.2.4. Microstructure Characterization

The next step in the assays employed in this work focused on microstructure characterization. In prior literature, the most common approaches employed in microstructure characterization of DP steels included optical microscopy [36, 38, 45, 51, 64-66, 170, 214, 230-232], scanning electron microscopy [36, 41, 42, 47, 51, 63, 214, 230, 232], and electron back-scattered diffraction (EBSD) [47, 48, 234-238]. While each of these techniques has demonstrated certain advantages over the others for highlighting specific aspects of the microstructure, our goal here is to identify and employ the protocols that give us the best chance at establishing reliable PSP

linkages. Furthermore, we also desire to minimize the overall effort required so that we can maximize the potential for high throughput.

After a careful consideration of the relative merits of the different protocols, it was decided to employ the EBSD technique for the present study. In addition to mapping lattice orientations in ferrite regions and indirectly identifying martensite regions (based on very poor diffraction patterns), the EBSD technique provides critically needed information on the extent of deformation pinning (in the ferrite grains next to the martensite grains; cf. Figure 4.10) through an analysis of the lattice misorientations. Consequently, although the use of the EBSD technique represented a time and effort intensive option for the present study, it was deemed essential as the other microscopy techniques are incapable of capturing any relevant information on the extent of pinned dislocations in the samples. It is emphasized that some measure (even if it is an indirect measure) of the pinned dislocation density is essential to correlate to the plastic properties of the sample.

EBSD scans were carried out in a field emission gun scanning electron microscope at 20 kV. Samples were prepared (for both EBSD and indentation studies) using standard metallography protocols. This involved grinding with silicon carbide papers down to grade 4000, and polishing sequentially with diamond suspensions of 3 μm, 1 μm, and OP-A alumina suspension. The final step in sample preparation was electro-polishing using A3 Struers electrolyte at 5 ºC.

Several scans (around 9 or 10) were collected on ND plane on all samples with 1μm resolution. It was also decided to keep the scan size consistent with the primary indentation zone in the mechanical characterization described earlier. The EBSD scan size was selected to be 400×400 μm^2. This is important because one of the goals of this study is to find linkages between indentation yield strength, σ_Y^{ind}, and the microstructure. Just as we conducted multiple indentation measurements on each sample, we have also conducted multiple EBSD scans on each sample to allow for the quantification of variance.

The collected raw data was post-analyzed using TSL OIM© software. Example EBSD scans obtained for different samples in our sample library are shown in Figure 4.13. In these figures,

multicolored regions represent ferrite grains whose lattice orientations have been mapped out with a 1μm spatial resolution and martensite regions are colored black. One can see that the martensite mostly forms at grain boundary regions and triple points. The amounts of martensite appear to increase with quenching from a higher intercritical temperature (from top row to the bottom row in Figure 4.13). Furthermore, a close inspection of the EBSD scans in Figure 4.13 reveals that samples subjected to higher deformation levels show significantly higher levels (and extent) of in-grain misorientations (i.e., compare left side maps with right side ones in Figure 4.13). The main implication here is that the misorientation fields in the samples do capture some information on the extent of pinned dislocations and their spatial distributions in the microstructure. This information will be utilized later in establishing the PSP linkages of interest in this study.

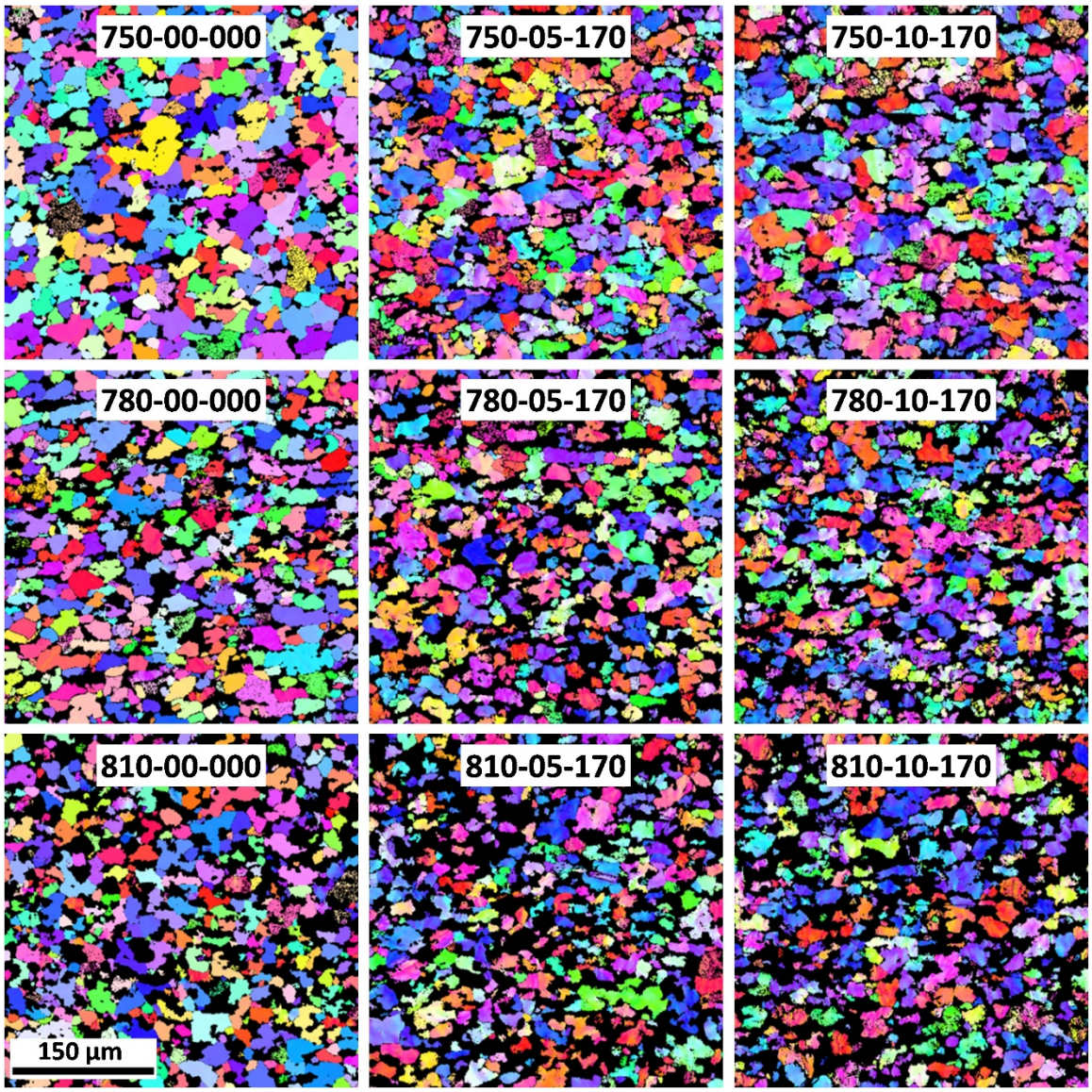

Figure 4.13: A sampling of microstructures produced in the present study.

Figure 4.14 shows φ_2= 45° section of the orientation distribution functions (ODFs) for all samples produced in this study. All textures depict α fiber, β fiber, and cube components. Applying deformation by means of cold work moves the strongest texture component from the $\{001\}\langle 110\rangle$ α fiber component to the $\{111\}\langle 110\rangle$ β fiber component. It is seen that the differences in texture between the samples are not very significant.

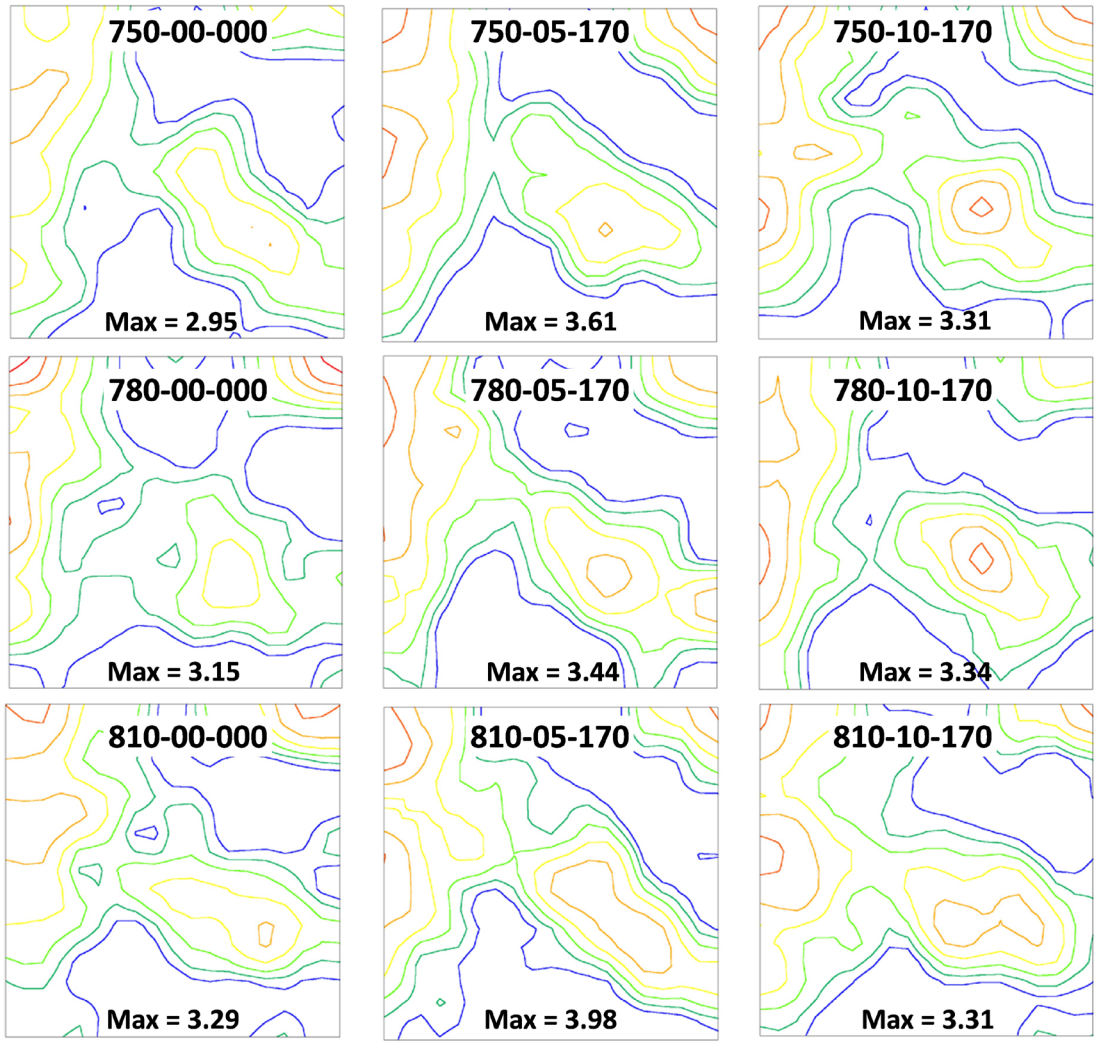

Figure 4.14: Ferrite textures in the φ_2= 45 degree section of the ODF for the different samples produced in this study.

As it was mentioned earlier, EBSD technique was chosen for this study because it provides information about phase as well as the extent of pinned dislocations (as indicated by local orientation gradients in the ferrite). In the case of DP steel, martensite can be identified based on low values of CI (confidence index) and IQ (image quality) [47, 48, 234, 235, 237, 238]. The poor quality of diffraction patterns in martensite is generally attributed to the high density of defects in these regions. More importantly, as the DP steel is deformed, dislocations accumulate at the martensite-ferrite boundaries producing significant local gradients in the lattice orientations (see

the right column in Figure 4.13). In other words, a suitable measure of the local orientation gradients can serve as an indicator of the local (microscale) hardening in the sample.

Currently used measures of in-grain misorientations can be broadly grouped as either grain-based or kernel-based approaches. Grain based approaches such as GOS (grain orientation spread) [239-241], GAM (grain average misorientation) [239, 241] estimate an average value of misorientation based on all measurements within one grain. In contrast, in kernel based approaches such as KAM (kernel average misorientation) [225, 242-244], quantities such as local average misorientation and local misorientation spread are computed at each grid point in the measurement scan. Clearly, the KAM is a better indicator of the local hardening in the microstructure.

KAM is defined as the average misorientation between the orientation at the center of the kernel and all its neighbors (Figure 4.15 (a)). In this approach, misorientations that exceed some tolerance value (maximum misorientation, 5°) are excluded from the averaging calculation, to avoid erroneous consideration of neighbors across a grain boundary. The distributions of KAM values recovered from the EBSD scans for the different samples in our sample library are shown in Figure 4.15 (b).

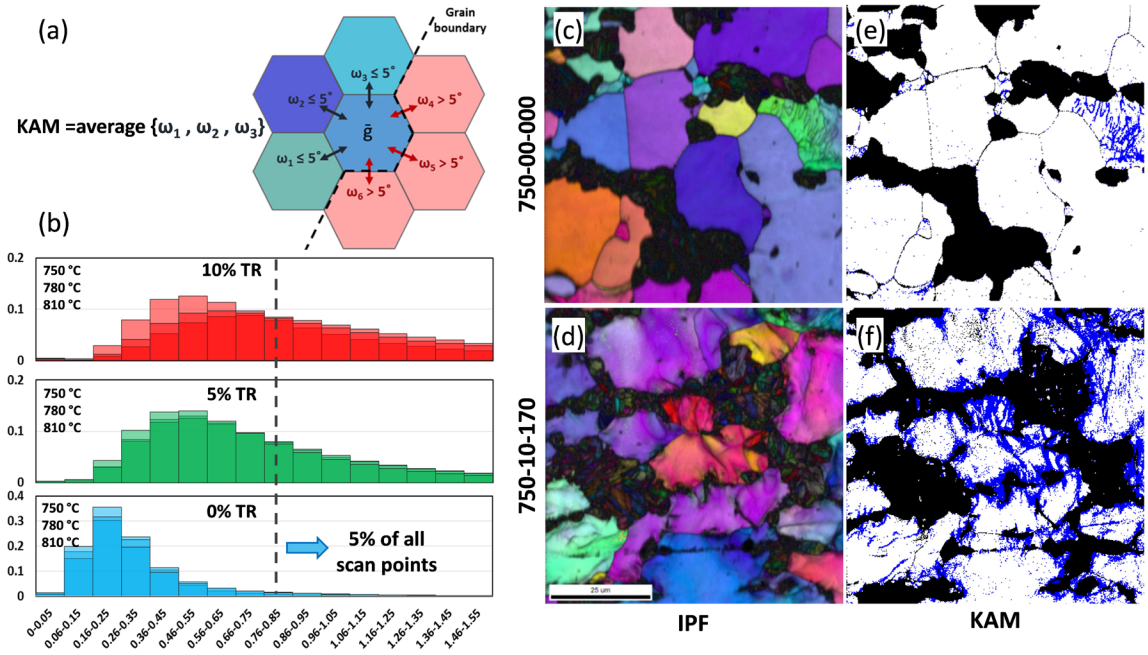

Figure 4.15: (a) Schematic of KAM definition for each pixel in the EBSD scan. (b) KAM distributions for the samples studied. (c) and (d) IPF maps from selected areas in samples with and without cold work. (e) and (f) Corresponding KAM maps identifying regions with KAM values larger than 0.8 in blue.

For the quantification of each microstructure, we need to make a judicious selection of the local states to be included in the analyses. Local states denote attributes needed to assign the local properties associated with each voxel of the microstructure. For the samples studied, the local state would be ideally defined by a combination of the phase identifier (i.e., ferrite or martensite), the lattice orientation, the KAM value, among several other potential attributes. It should, however, be recognized that adding more local state attributes will exponentially increase the effort expended in arriving at PSP linkages of interest. Therefore, it behooves us to make smart choices in the selection of local states.

In the present study, we have decided to include only the phase identifier and the KAM as the local state attributes. Since the texture in the sample did not change appreciably between the different processing histories employed in the study, the lattice orientation was not included as a local state variable in each voxel. This is also partly because the inclusion of the lattice orientation

as a state variable increases dramatically the effort involved in microstructure quantification [76, 78], which is not justified when there do not exist significant differences in crystallographic and/or morphological textures in the ensemble of samples studied. Finally, it was also decided to use a discretized representation of the KAM value in the microstructure quantification pursued in this work. Based on the histograms shown in Figure 4.15 (b), it was decided that a KAM value of 0.8º or more would be labelled as "deformed ferrite", while KAM values lower than 0.8º would be labelled as "undeformed ferrite". Note that 95% of the KAM values in all samples quenched at 750, 780, and 810 ºC (without any cold work) exhibited values below 0.8º (see Figure 4.15 (b)), justifying the selection of this value.

As a consequence of the simplifications introduced above, each voxel in the microstructure is assigned to one of three discrete local states: martensite, deformed ferrite, or undeformed ferrite. Although one might raise objections to such gross simplifications, it is important to recognize and understand that a much more detailed quantification of the microstructure may actually be not warranted in the present study. Indeed, we will demonstrate that this simple selection of local states is adequate in the present study to establish reliable PSP linkages of interest. Of course, as one expands the processing windows to be included in the PSP linkages being formulated, one would need to add additional attributes in the description of the local states.

Figure 4.15 (c) and (d) show selected areas of the measured IPF maps for 750-00-000 and 750-10-170 samples. Figure 4.15 (e) and (f) show the corresponding discretized microstructures employed in the quantification of the material structure in this study. As noted earlier, these microstructures have only three discrete states, which are colored black, white, and blue in Figure 4.15 (e) and (f). Note the increase in the number of blue voxels, especially near the martensite interfaces, in the 750-10-170 microstructure compared to the 750-00-000 microstructure.

In this study, we will employ the framework of 2-point statistics to quantify the microstructures generated in this work. Since, the microstructures studied here have three local states, a total of nine 2-point spatial correlations can be defined. Three of the computed 2-point

correlations for sample 780-10-170 are shown in Figure 4.16, along with the original EBSD scan and the discretized microstructure. The autocorrelation of the martensite (colored black), the autocorrelation of the deformed ferrite (colored blue), and the cross-correlation of the martensite and the deformed ferrite are shown in Figure 4.16 (c), (d), and (e), respectively. These spatial statistics maps contain a tremendous amount of information about the morphology and distribution of the local states in the microstructure. For example, the center peaks in the autocorrelations provide the volume fraction information. Consequently, it can be seen that the volume fractions of martensite and deformed ferrite are 0.45 and 0.276, respectively, for the microstructure shown in Figure 4.16. The contours in the center of the autocorrelation plots provide quantitative information on the shape of local state field in the microstructure. One can also extract a large number of conventional microstructure measures from these plots [30, 31], and even reconstruct the original microstructure from its spatial correlations [155-157].

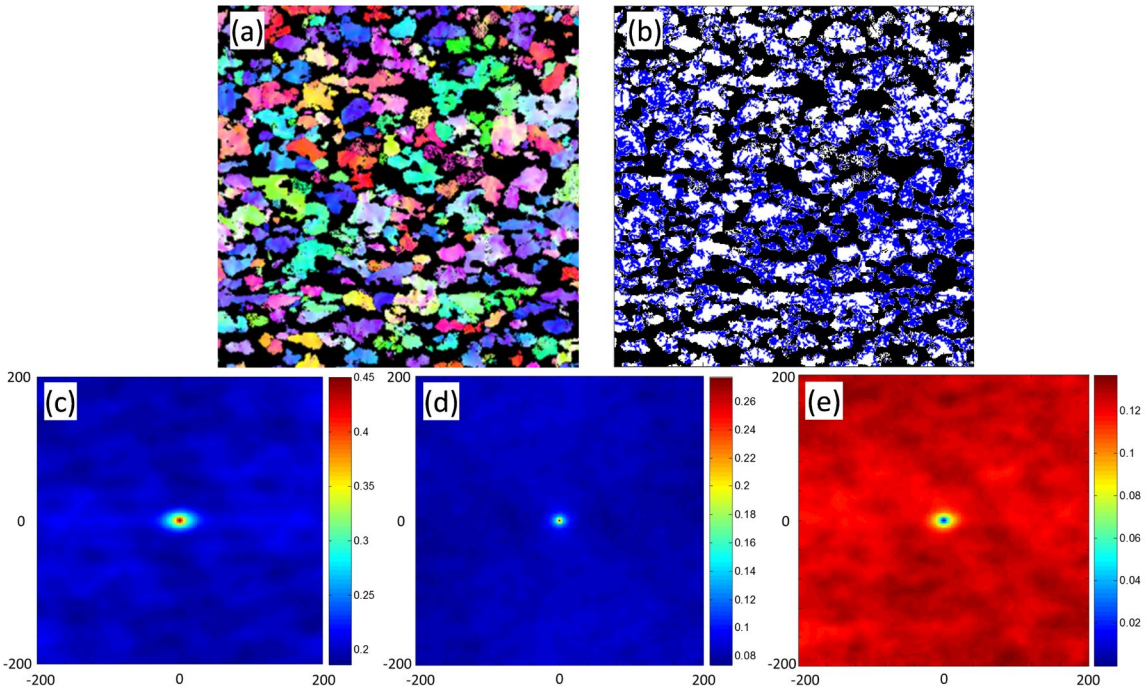

Figure 4.16: (a) An IPF map from the sample 780-10-170. (b) A map showing the three local states selected for the study - martensite as black pixels, deformed ferrite as blue pixels, and undeformed ferrite as white pixels. (c) Autocorrelation of martensite, (d) autocorrelation of deformed ferrite, and cross-correlation of martensite and deformed ferrite.

As discussed before the quantification of microstructures using the framework of 2-point statistics produces a very large vector of descriptors for the microstructure (every voxel in each of the correlation maps would be an entry in this vector). For the present case study, PCA was performed on a total of 81 EBSD scans (nine scans for each of nine process histories). The analyses indicated that only two PC scores (see Figure 4.17) are adequate to capture 99.4% of the variance between the different microstructures in this ensemble (i.e., all 81 scans included in the study). In other words, only two numbers (i.e., the first two PC scores denoted as PC1 and PC2) are adequate to distinguish each of the microstructures produced in this study. This is indeed a remarkable dimensionality reduction, and to the best of our knowledge, unmatched by any other existing framework for microstructure quantification.

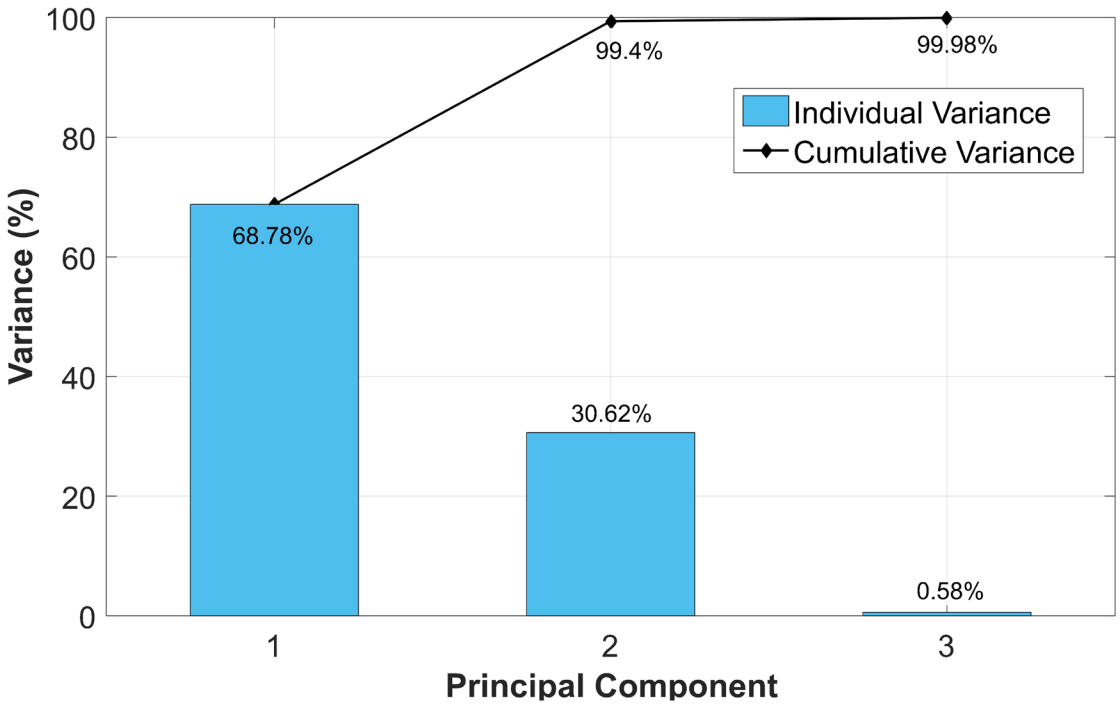

Figure 4.17: The individual and cumulative variances from the PCA for the first 3 principal components shows that PC1 and PC2 carry 99.4% of the total variance in the dataset.

For microstructures with three local states, only two of the nine 2-point spatial correlations would be independent [72], if the boundaries of the microstructure were treated as periodic. However, through repeated trials of the PCA described above, we observed that using the two autocorrelations and the cross-correlation shown in Figure 4.16 provided a good separation between the microstructures of each of the nine groups of samples.

Figure 4.18 shows all of the microstructures included in the present study in the low dimensional PC space, where each point represents one microstructure. The interclass (nine different processing histories) and the intraclass (nine microstructures from each sample) variances are clearly discernable in this plot. Furthermore, one should note that the variance in PC1 is higher than the variance in PC2 for the ensemble of microstructures studied. It is observed that the intraclass variance for the deformed samples is higher than the intraclass variance for the undeformed samples. Most importantly, one can discern trends in the microstructure evolution by

following the centroids of each class of microstructures. For example, one can capture quantitatively the effect of quenching temperature by following the dashed lines. Similarly, one can follow the effect of cold work by following the solid lines in this figure. These trend lines can be called processing paths or processing streamlines, as they capture quantitatively the salient aspects of the influence of process parameters on the evolved microstructures. It is indeed remarkable that a simple data-driven approach involving 2-point spatial correlations and PCA can capture so much detail with just two PCs.

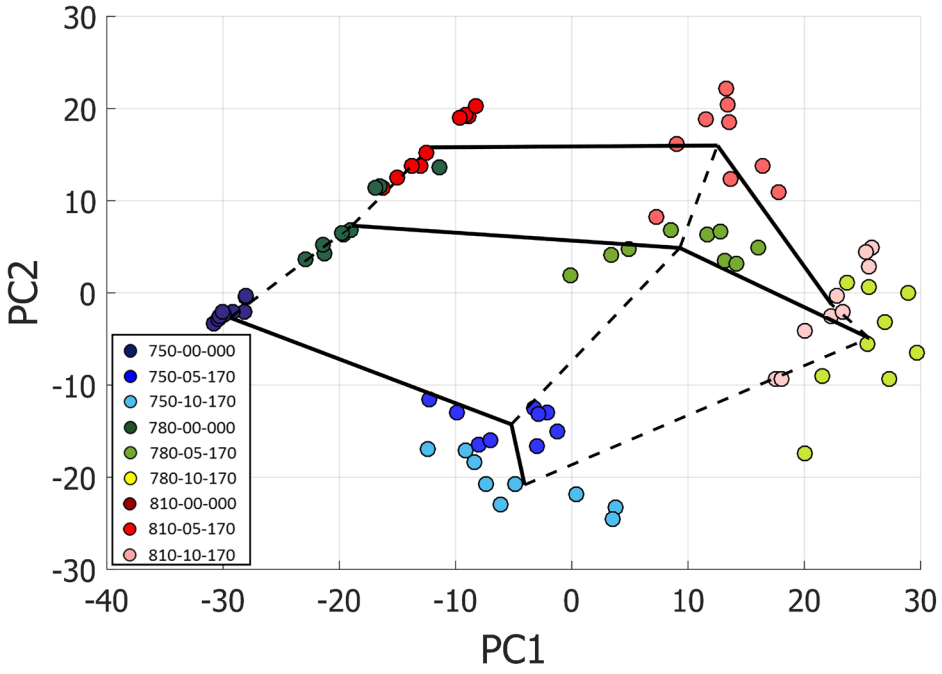

Figure 4.18: Low-dimensional representation of the entire ensemble of 81 micrographs obtained from PCA, colored by the different processing histories. Solid lines capture the influence of cold work, while the dashed lines show the effect of the intercritical annealing temperature.

4.2.5. Extraction of PSP Linkages

Building on the low dimensional structure representation obtained in the previous section (i.e., PC1 and PC2), we are now in a position to establish PSP linkages of interest. For the present case study, the process parameters are taken as the intercritical annealing temperature (T) from which the samples are quenched, and the imposed thickness reduction during the rolling process

(D). The desired process-structure linkages are then established using least squares regression and cross-validation techniques [68], which resulted in a second-order polynomial fit expressed as

$$PC1 = -5612.478 + 14.089\,T - 5.138\,D + (15.308\,(D \times T) - 8.862\,T^2 - 332.461) \times 10^{-3} \quad \textbf{(4.1)}$$

$$PC2 = -2734.355 + 6.665\,T - 1.682\,D + (1.823\,(D \times T) - 4.035\,T^2 - 131.892) \times 10^{-3} \quad \textbf{(4.2)}$$

The accuracy of these models is displayed as parity plots in Figure 4.19, where each point corresponds to one process history (i.e., the average of all 9 scans from each sample).

PC1 and PC2 denote the strengths of certain spatial patterns in the microstructure. These patterns are visualized in Figure 4.20. The first column in this figure shows the ensemble average, while the second and third columns depict the patterns captured by PC1 and PC2, respectively. In the PC space, each microstructure is approximated as a weighted deviation from the ensemble average (see Eq. (11)) using the φ_{ir} (plotted in second and third columns of Figure 4.20) as an orthonormal basis. As an example, as PC1 is increased, it is seen (from the second column in Figure 4.20) that the volume fractions of martensite and deformed ferrite will both increase, and the martensite regions will become more elongated in the horizontal direction. Likewise, when PC2 is increased, there is an increase in the volume fraction of martensite accompanied with a decrease in the volume fraction of the deformed ferrite, while making the martensite regions more equiaxed. Of course, there is a lot more information embedded in the basis maps shown in Figure 4.20, which actually contributes to the remarkable efficacy of PCA in arriving at the low dimensional representation employed in this study. There currently do not yet exist any systematic approaches for carefully studying these basis maps.

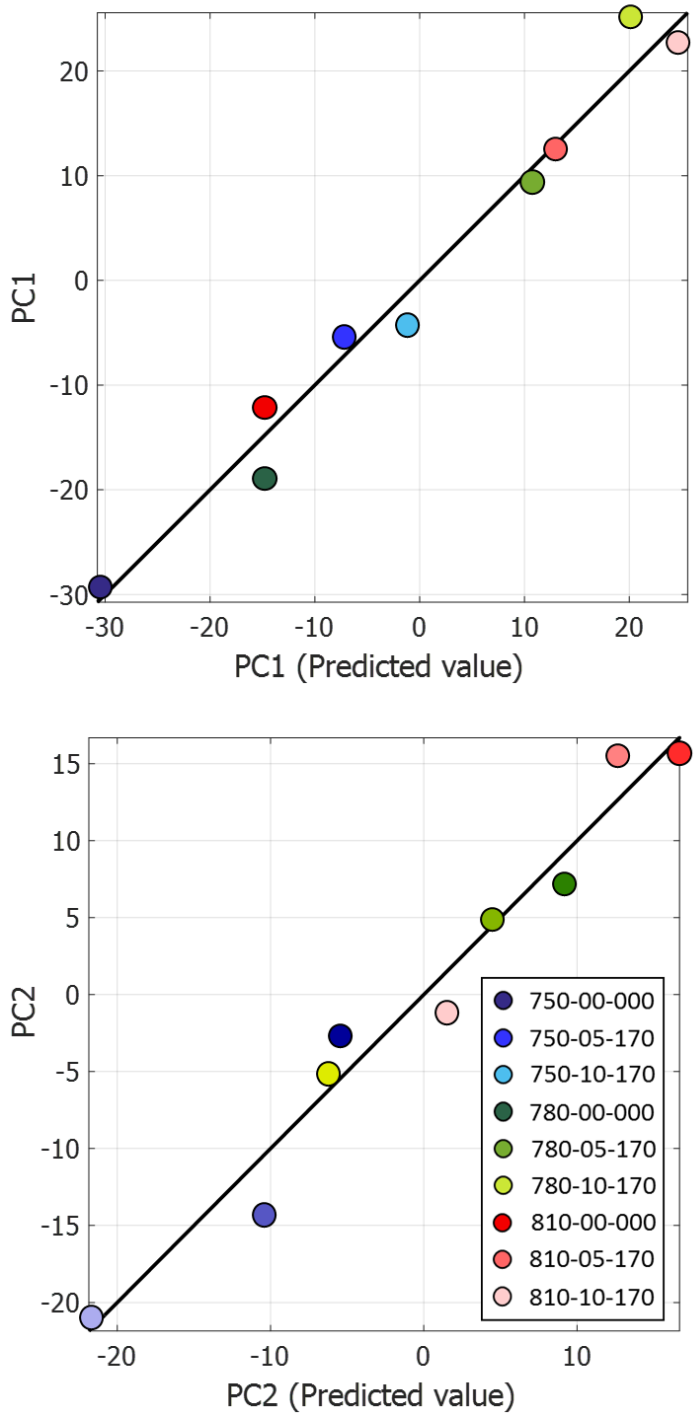

Figure 4.19: The accuracy of process-structure linkages established in this work using data science approaches. The process variables included the intercritical annealing temperature (*T*) in °C and the amount of cold work (percentage of thickness reduction) from rolling process. Each point is an ensemble average of 2-point statistics of all scans from one processing history.

The approach described above can also be applied to establish a structure-property linkage. For the present case study, the recovered structure-property linkage is expressed as

$$\sigma_Y^{ind} = 1156.4 + 9.2\ (PC1) + 5.5(PC2) \quad \textbf{(4.3)}$$

where σ_Y^{ind} denotes the yield strength of the material measured in the indentation protocols described earlier. The accuracy of this linkage is depicted in the parity plot shown in Figure 4.21.

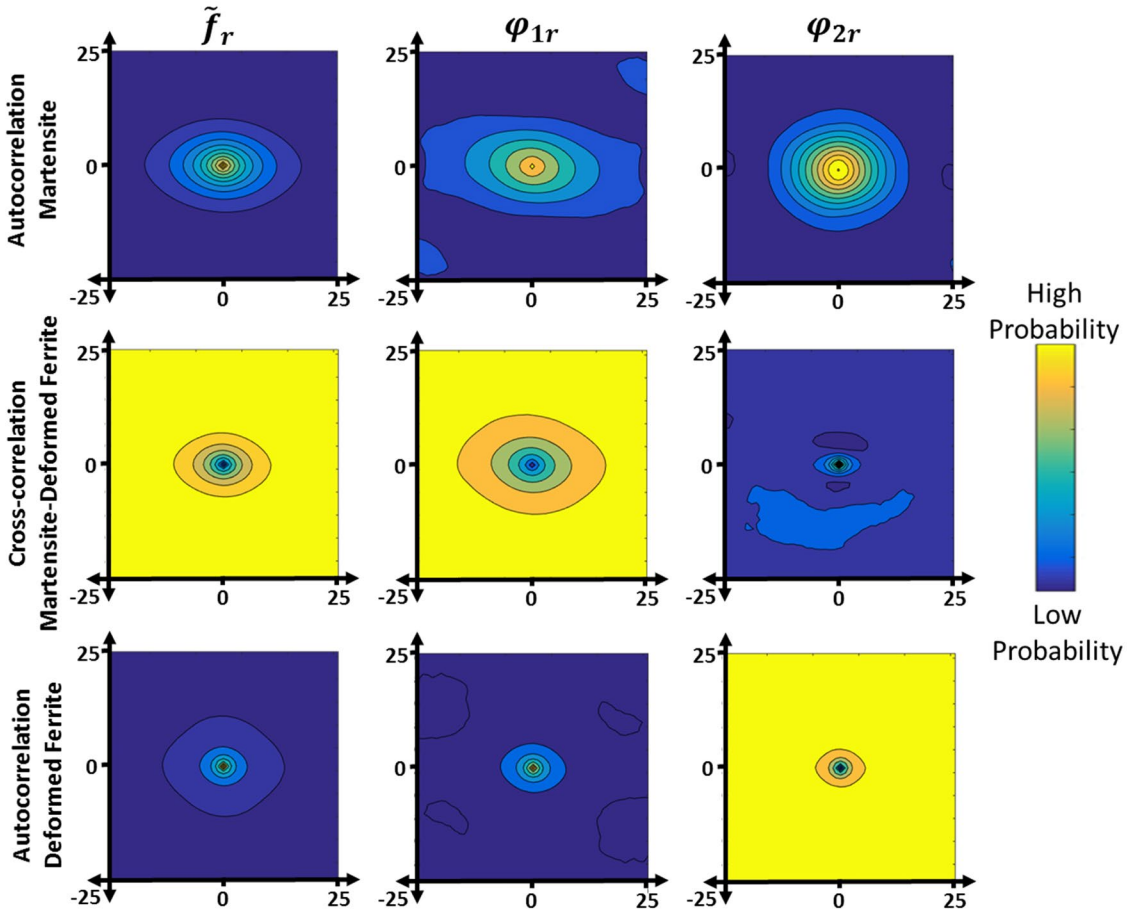

Figure 4.20: The ensemble average and the first two PC basis ($\varphi_{1r}$and φ_{2r}; see Eq. (11)) computed in the PCA on the entire ensemble of microstructures studied.

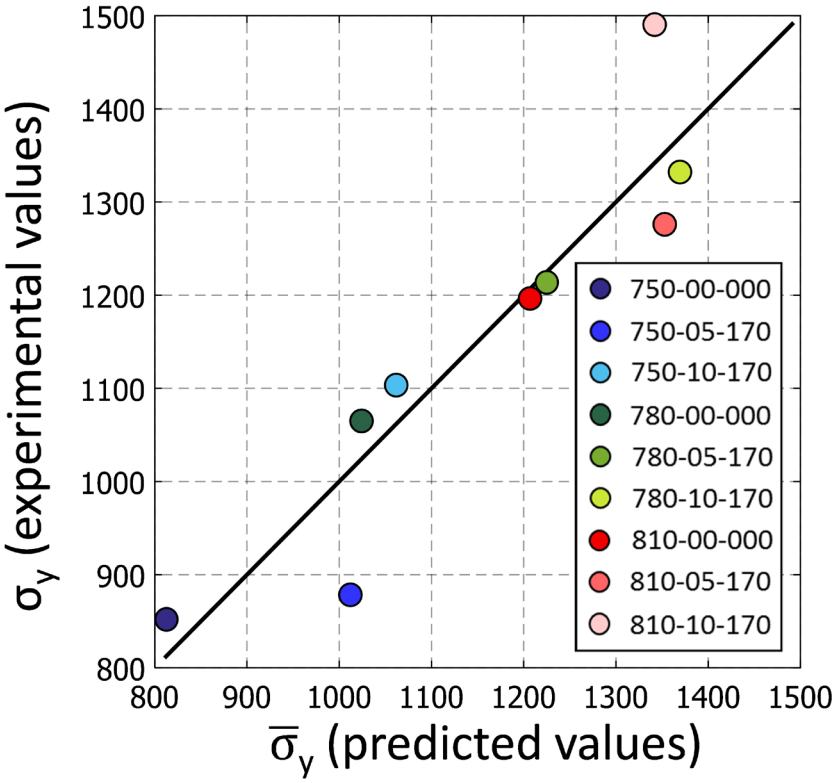

Figure 4.21: The accuracy of the structure–property linkage established in this work using data science approaches. The property captured is the indentation yield strength. Each point is an ensemble average of all measurements from one processing history.

The reader is reminded that the linkages developed here are data-driven. One of the implications is that the PSP linkages built here will change when new data is added. This is to be expected, especially since we used only nine different processing histories in this study. When a substantial amount of data becomes available, we could expect the PSP linkages to become stable (i.e., there would be no need to change the PSP linkages with the addition of new data points). This indeed is the most attractive feature of the protocols described here. They allow a coordinated effort by research groups and/or investigators in ways that leverage all available data and minimize redundant effort in establishing such linkages. Furthermore, with the use of high throughput strategies, such as the indentation methods described in this paper, it is conceivable to aggregate

PSP linkages of high value to the scientific community at dramatically accelerated pace compared to the conventional approaches used currently.

4.2.6. Summary

In this study, we have formulated and demonstrated novel high throughput assays for extracting data-driven, high value, PSP linkages in complex multiphase structural alloys such as DP steels. These new protocols utilized spherical indentation stress-strain measurements, 2-point spatial correlations, principal component analysis (PCA), and regression techniques. Following are the major findings from this study:

Spherical indentation is a reliable high throughput tool for probing the changes in the yield behavior of dual phase steel processed at different intercritical annealing temperatures and different amounts of cold work applied before bake hardening. While indentation elastic modulus showed only small variations as expected, indentation yield strength varied significantly with the processing history. This is attributed to the many changes induced in the microstructure of the sample with the processing history. These have included not only changes in the volume fractions of the different constituents, but also their spatial distributions. Additionally, the spatial distribution of the dislocation content at the martensite/ferrite interface also played an important role in controlling the final plastic yield values in the sample.

The application of PCA on the 2-point correlations provided a rigorous framework for objective, low-dimensional, quantification of the microstructures in DP steels. In this work, this protocol was applied only on the phase and misorientation information. The protocol found that only two PCs are needed to distinguish the microstructures studied and establish reliable PSP linkages. However, the framework is highly extensible for including more details of the microstructure (additional local states as well as higher-order spatial correlations) as more data becomes available.

Chapter 5 Application to Ti-Based BMG MCs

This chapter presents the application of the high throughput indentation testing and microstructure quantification protocols in Ti bulk metallic glass matrix composites (Ti BMG-MC). These alloys are still under development in order to find the best fabrication parameters as well as overall chemical composition for the final performance of interest. The manufacturing cost for these alloys are very high even at laboratory scale, and therefore the exploration of wide range of composition and processing parameters in a short time is very limited and is not practical. As it was mentioned before, statistical evaluation of the mechanical response for a new material at different processing condition is a costly process. The cost is mainly for producing large amount of materials at different processing condition, and then testing each sample bar one by one to evaluate the influence of composition and the processing parameters. Hence, as one can see, utilizing fast screening mechanical testing protocols, such as indentation, is inevitable in exploring large design spaces in material chemistry and process histories. In addition, BMG-MC material systems can represent all different types of composite materials whether the reinforcement particles or fibers are added to a matrix material or they are fabricated naturally during thermal treatments. In the latter case the challenge would be in locating tiny particles to conduct a test. Then it will be possible to perform indentation testing with different tip diameter to evaluate bulk mechanical response as well as individual constituent's responses. This will be the main challenge that we are addressing in this chapter. Given our interest in covering a very large window of material chemistries and process histories in Ti-BMG MC material systems, it is also clear that the protocols need to be high throughput. Such measurements are critical for the validation and calibration of multiscale materials models used in tailoring the material properties for any targeted application. To the best of authors' knowledge, the elastic-plastic responses of the individual phases in such composites have not been measured and reported in current literature in a systematic meaningful manner. This chapter contains two sections;

a) Multiscale mechanical characterization of both crystalline and amorphous phases
b) Developing protocols in establishing processing-structure-property linkages for indentation yield strength property

In the first step, both nanoindentation and microindentation tests were conducted to evaluate the mechanical responses at two distinct length-scales in four different Ti-based BMG MC alloys. In nanoindentation, the aim is to measure mechanical response of each crystalline and amorphous phase by using a spherical 1μm tip radius. The locations for indentation on each phase were identified using SEM images and an optical microscope. Then, composition effects on individual phases were investigated at two length-scales in both phases. In addition, more detailed analysis was performed on the indentation tests to shed light on the deformation mechanisms in the amorphous phase. Utilizing these high throughput protocols, we report for the first time a large number of indentation stress-strain measurements from both the crystalline and amorphous regions in four differently processed BMG-MC samples. The set of measurements is large enough to characterize the local responses of the individual constituent phases in the samples in a statistically meaningful manner. More importantly, it will be shown that these new protocols can produce quantitative and meaningful insights into the driving forces responsible for microscale shear banding in the samples studied.

In the second step, the local mechanical properties were assessed using a microindenter using a 500μm tip radius. This tip size was selected considering the high strength of the alloys and the load limit in the microindentation machine. In order to establish process-structure-property linkages, approaches similar to those taken in the previous chapters are applied. However, this time, we tried not to build these linkages based on the average properties and the ensemble average of the microstructure. Instead, microstructure images at indentation locations were captured by SEM before indentation testing. Since the SEM data collection is faster than EBSD technique, larger surrounding areas of indentation sites were imaged as well and added to the analysis. Using this approach, short-and long-distance variation in the microstructure could be captured. In addition,

incorporating more images in the protocol of using 2-point statistics and PCA analysis, provides more stable bases for the PC frame. And therefore, it becomes less sensitive to adding new images of these alloy's microstructure later in the analysis.

5.1. Introduction

Bulk metallic glass matrix composites (BMG-MC) have shown a remarkable combination of high specific strength and high specific fracture toughness compared to other metallic systems, making them excellent candidates for several advanced technologies [245-251]. A large number of experimental and computational studies have reported the influential role of microscale shear banding on the plastic response of the amorphous phases. However, experimental protocols needed for reliably extracting a quantitative fundamental understanding of the driving forces responsible for this deformation mechanism have not yet been established and demonstrated; this constitutes one of the main hurdles in the exploitation and further development of the bulk metallic glasses [252-260]. The gap is even more acute for BMG-MCs, where the size, distribution and volume fraction of the crystalline and glass phases vary significantly with both chemistry and the process histories. Several studies have reported effective (bulk) mechanical properties of various metallic glass alloys measured using standard test methods such as the simple compression test [261-266], tension test [266-269], and bending test [269-273]. In several of these studies, researchers have presented qualitative observations of microscale shear banding and its effect on the measured effective properties. Some of the critically missing quantitative information include: (i) elastic-plastic responses of the individual constituent phases (crystalline and glass phases), and (ii) their variation with changes in chemistry and process history and its influence on the bulk mechanical response.

5.2. Materials and Experimental Procedure

The materials evaluated in this work were produced in the Division of Materials Development and Manufacturing Technology at the NASA JPL (Jet Propulsion Laboratory). The

DVx BMG-MCs alloys are based on Ti-Zr-V-Cu-Be system and made by arc melting followed by suction casting process. The process involved melting constituent elements in a water-cooled copper bowl and rapid solidification by termination of the arc. The cooling rate in this process is about 500° /s leading to formation of amorphous and crystalline regions. Three different Ti-based BMG-MC alloys were selected with following compositions: DV2 ($Ti_{44}Zr_{28}V_{12}Cu_5Be_{19}$), DV1 ($Ti_{48}Zr_{20}V_{12}Cu_5Be_{15}$), and DV4 ($Ti_{62}Zr_{18}V_{10}$ Cu_4Be_9). The DV0 sample has a composition of $Ti_{29.5}Zr_{28}V_{5.8}Cu_9Be_{27.7}$. The glass content in the composites is the highest in the DV2 and lowest in the DV4 composite. The DV0 sample has 100% glass content. (cf. [274]). The differences in the composition of these alloys resulted in different volume fractions of glass phase in the composite.

Careful considerations are taken in the sample preparation to avoid possible damages introduced during the preparation. Samples were cut using wire EDM technique to minimize damage layer on the sample surface to few microns which can be easily removed by progressively grinding (1200, 2400 and 4000 grit) with SiC papers and polishing with diamond suspension (3, and 1 μm) followed by vibro-polishing in the mixture of colloidal silica (0.06 μm) and Hydrogen peroxide slurry for 48 hrs.

Nano- and micro-indentation experiments were conducted with customized Zwick-Roell Z2.5 hardness tester and G200 Agilent systems respectively. The indenter tips used are a diamond conical tip with radius of 1 μm and a tungsten-carbide spherical tip with a 500 μm radius. Tests were performed with a constant strain rate (loading rate divided by the load) of 0.05 s−1 to maximum depths of 300 nm. CSM was run at a displacement amplitude and oscillation of 2 nm and 45 Hz, respectively. The corresponding length scales of the indentation probed volume are 0.03 mm^3 and 0.04 μm^3, for the two tips used in this study. A minimum of 20 microindentation tests were performed at randomly selected locations on the surface of each sample coupon. In addition, a minimum of 15 nanoindentation tests were carefully placed on each individual phase in all samples. Imprints of all tests were imaged by SEM to aid in further interpretation of results.

5.3. Multi length-scale mechanical measurements of composite materials: Application to Ti-based bulk metallic glass matrix composites (Ti BMG-MC)

The microstructures of the studied alloys were investigated using a Tescan Mira XMH FE-SEM. Figure 5.1(a-d) shows small BSE (backscattered electron) images of DV0, DV2, DV1, and DV4 samples respectively. The DV0 sample is a monolithic bulk metallic glass one with no evidence of existence of any other phase, while the other alloys consist of two phases; bright phase (amorphous) and dark phase (crystalline). The DV2 samples contain only ~30% crystalline dendrites while other two have more, ~47% in DV1 and ~60% in DV4 (based on the values reported in Hofmann [274], more accurate measurements will be presented in Section 5.4)

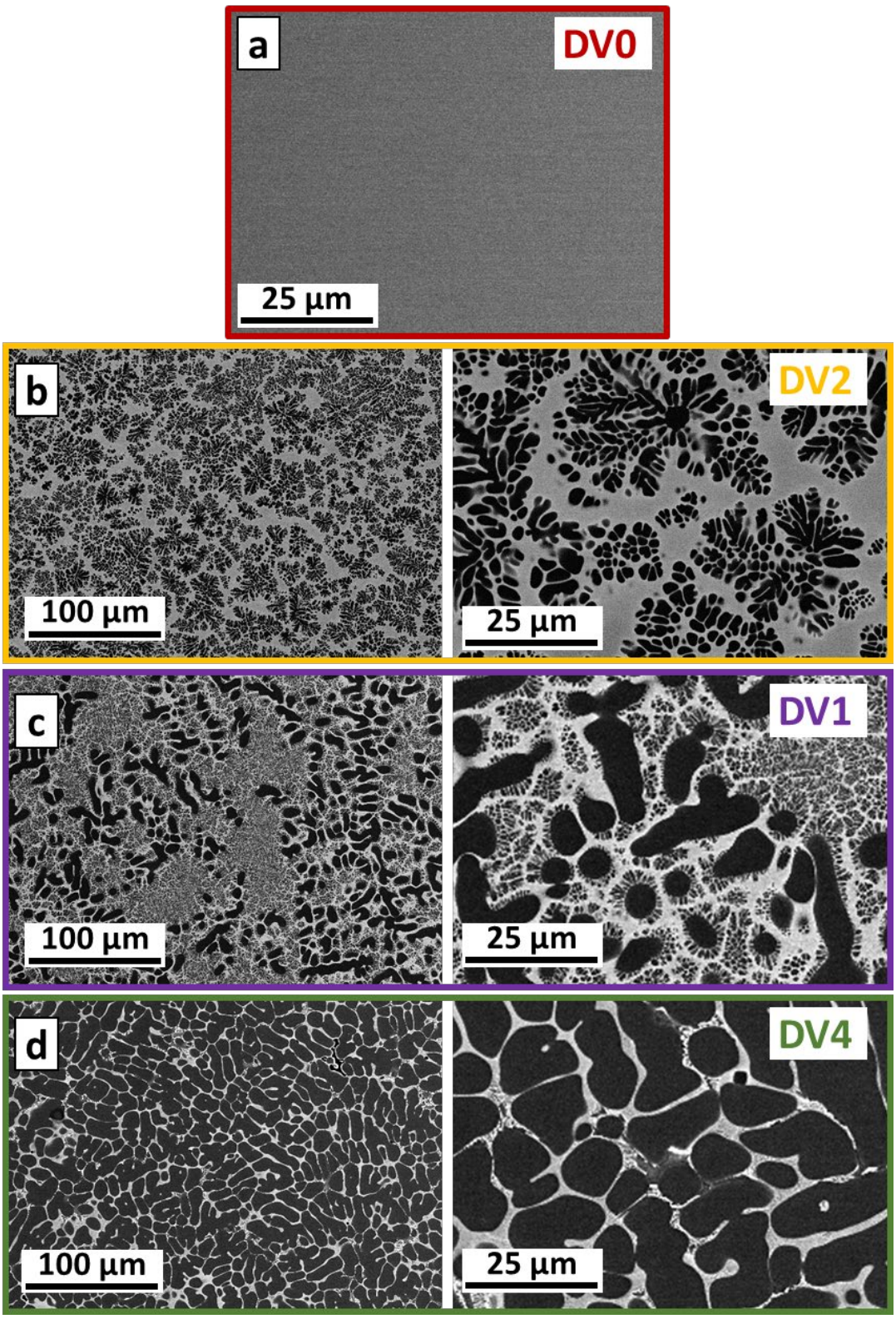

Figure 5.1: BSE images of the microstructure of the bulk metallic glass (DV0) and other three bulk metallic glass matrix composites (DV2, DV1, and DV4) with different volume fractions of crystalline phase.

As it is evident in Figure 5.1 images, the amorphous phase contains heavier elements as it appears brighter in BSE mode. Details of distribution of elements in both phases was investigated by Energy Dispersive Spectroscopy (EDS) for all alloys using a Hitachi SU-8230 SEM with Oxford EDS detector with X-Max detector and SATW window. The elemental distribution maps long with their corresponding BSE images are presented in Figure 5.2. During the process of solidification, the Zr, Cu and Be elements segregate from nucleated crystalline dendrite and push out to form the amorphous phase. On the other side, the crystalline phase contains more of titanium and vanadium in all alloys. Despite segregation of elements between two phases, no gradient of composition is observed within each phase. Consequently, we can represent this microstructure using only two local states (glass and amorphous) as described in Section 5.4.

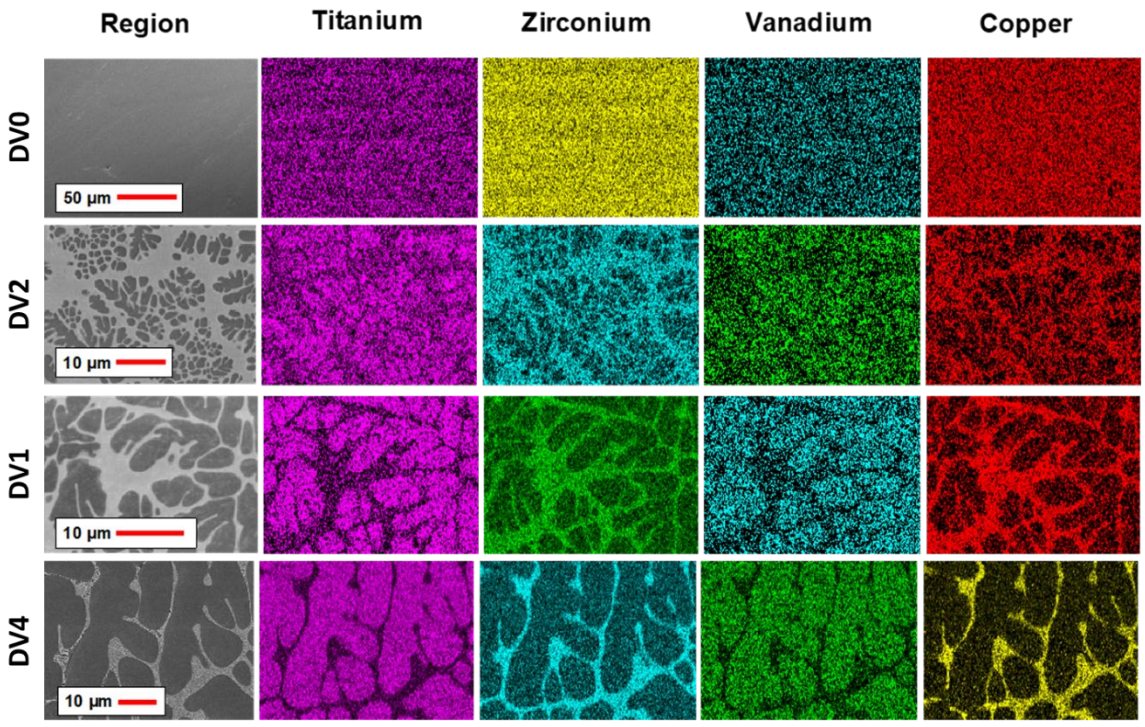

Figure 5.2: The element distribution maps from EDS analysis for Ti, Zr, V, and Cu

The mechanical properties of these materials have been investigated using uniaxial tensile tests in the work published by Hofmann [274]. The results are presented in the Figure 5.3 and as

one can see the tensile strength of the metallic glass composite are enhanced up to 1.6 GPa which is a big improvement compared to the Grade 5 Ti-6Al-4V and Grade 2 commercially pure titanium. These new alloys also present very comparable fracture toughness to Ti64 alloy. A summary of the measured mechanical properties from that study is presented in Table 5-1. The importance of the strength and toughness enhancement becomes more prominent when the density of the newly developed alloy are measured and considered. The density measurements are made using Archimedes method by measuring weight of the sample before and after submerging in water. It is defined by the following equation:

$$\rho_{sample} = \rho_{water} \frac{m_{dry}}{m_{dry} - m_{wet}} \quad \textbf{(5.1)}$$

The test were performed 4-5 times and average values are reported for each alloy in the Table 5-1. As evident in the density measurements, the density of the new alloys are similar to CP-Ti and Ti64 alloys which results in much higher specific strength of these Ti-based BMG-MCs.

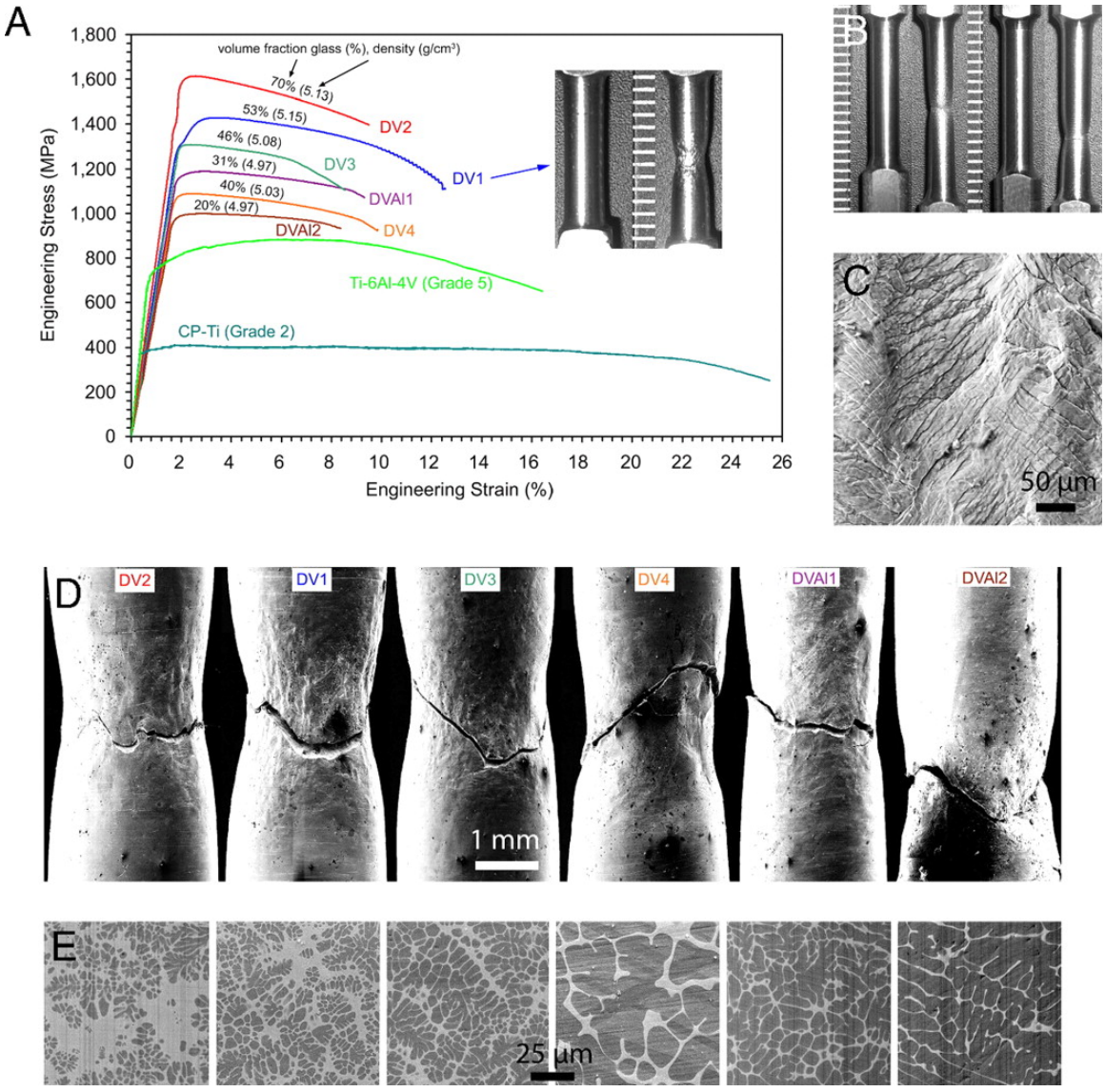

Figure 5.3: Tensile properties (A) and microstructure of the newly developed Ti-based metallic glass composites (E) and the SEM images of the necking region for the tested materials (D). The results are compared with tensile data from CP-titanium and Ti64 titanium alloy.

Table 5-1: Comparison between mechanical properties and density of the Ti-Based BMG-MCs and CP-Ti and Ti64 alloys (* data from [275])

	at%	wt%	%BMG (Amorphous)	%BCC (Crystalline)	Density (g/cm^3)	σ_y (MPa)	K_{1c} ($MPa.m^{1/2}$)
DV0	$Ti_{29.5}Zr_{28}V_{5.8}Cu_9Be_{27.7}$	$Ti_{27.7}Zr_{50.2}V_{5.8}Cu_{11.3}Be_{4.9}$	100	0	5.320 ± 0.0004	NA	-
DV2	$Ti_{44}Zr_{28}V_{12}Cu_5Be_{19}$	$Ti_{41.9}Zr_{36.3}V_{12.1}Cu_{6.3}Be_{3.4}$	70	30	5.310 ± 0.0004	1597	-
DV1	$Ti_{48}Zr_{20}V_{12}Cu_5Be_{15}$	$Ti_{44}Zr_{35.2}V_{11.8}Cu_{6.1}Be_{2.6}$	53	47	5.194 ± 0.0007	1362	43.8
DV4	$Ti_{62}Zr_{18}V_{10}Cu_4Be_9$	$Ti_{57.3}Zr_{26.4}V_{9.8}Cu_{4.9}Be_{1.6}$	40	60	4.993 ± 0.0002	1086	61.6
Ti64*	$Ti_{86.1}Al_{10.3}V_{3.6}$	$Ti_{90}Al_6V_4$ (Grade 5, annealed-STA))	NA	NA	4.43	950-1170	75-43
CP-Ti*	Ti_{100}	Ti_{100} (Grade 2)	NA	NA	4.51	66	380

As discussed earlier, several fiducial markers are placed on the sample in square grid format in order to locate the indentation sites in the center of each square. The fiducials are placed at 600 μm distance to assure they don't affect the indentation measurements (Figure 5.4). Then the microindentation tests were carefully performed in the center of the square grid (highlighted in yellow in the figure).

The tests were conducted with a tungsten-carbide spherical tip with a 500 μm radius. The initial elastic loading regime was identified using the method explained in Section 2.4 (see Figure 2.11). The initial loading, load increments, and number of unloading cycles were set to be 10 N, 5 N, and 20. An example of microindentation load-displacement curve is presented in Figure 5.5. The data corresponds to DV1 sample. The elastic modulus of the sample was estimated from the initial elastic loading segment highlighted in red in Figure 5.5(a) using Equation (2.26), and then indentation stress and indentation strain were calculated for each unloading segment. The estimated elastic modulus value for this example test was 87 GPa. The indentation yield strength was estimated to be 2.59 GPa (using a 0.2% strain offset). In addition, the slope of a line fitted to the indentation stress-strain data after plasticity occurs up to 1% plastic strain is used to extract the

indentation initial work hardening rate (42.5 GPa for this example). Several microindentation (20-25) tests were done on random locations on the surface of each sample coupon. The results for all indentation stress-strain responses for all four samples are shown in Figure 5.6.

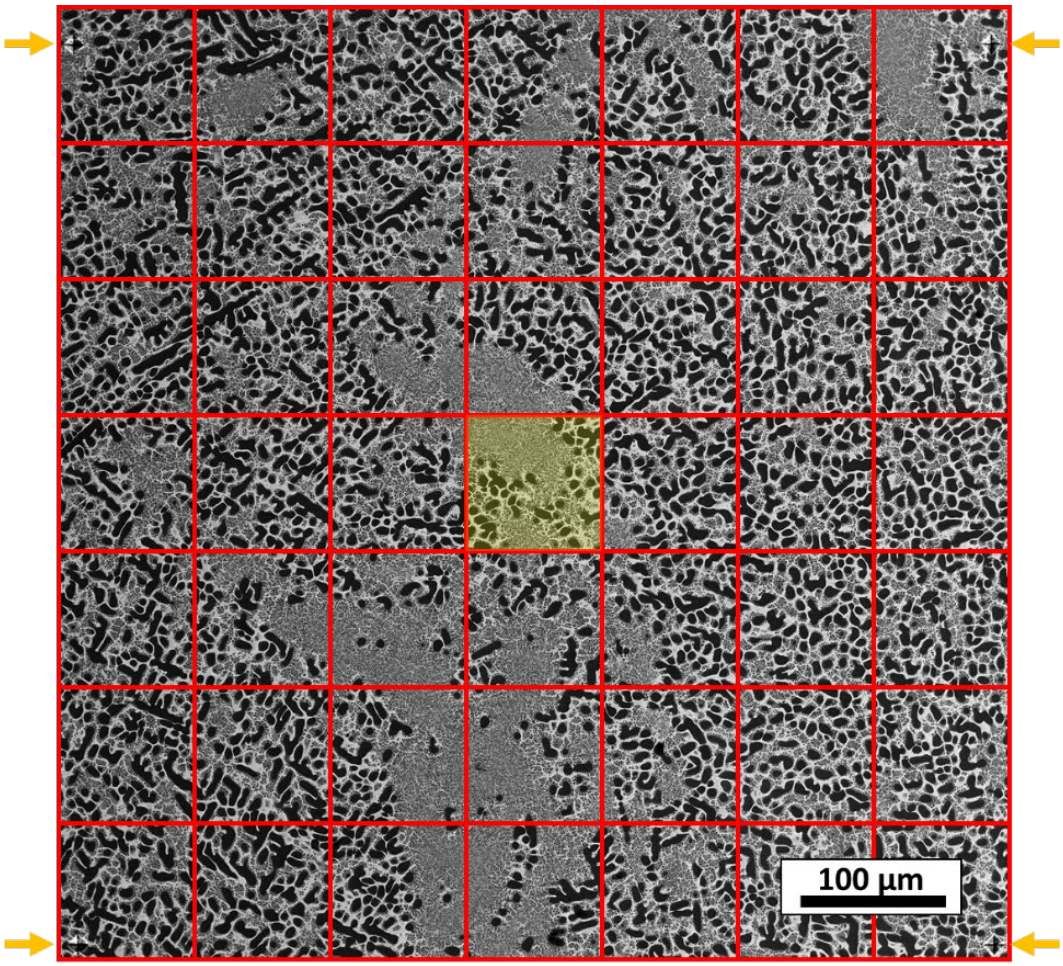

Figure 5.4: Example of setting up a site for an indentation before performing the test to collect image of the indented area as big as the indentation zone at yield point. The rest of the image were divided to smaller ones with similar dimensions of the one in the center. Orange arrows indicated the location of the fiducial markers.

The extracted indentation elastic modulus, yield strength, and work hardening are summarized in the Figure 5.7 and Table 5-2. The elastic modulus increases from 82.79± 3.25 GPa (DV4) to 88.17 ± 4.57 GPa (DV1), to 91.41 ± 4.51 GPa (DV2), and to 98.17± 1.70 GPa (DV0),

and correlates well with the increasing volume fraction of the glass phase that has higher elastic modulus. The same increasing trend is observed in the 0.2% offset indentation yield strengths obtained as 2.03 ± 0.07, 2.52 ± 0.27, 3.03 ± 0.24, and 3.51± 0.19 GPa for DV4, DV1, DV2, and DV0, respectively.

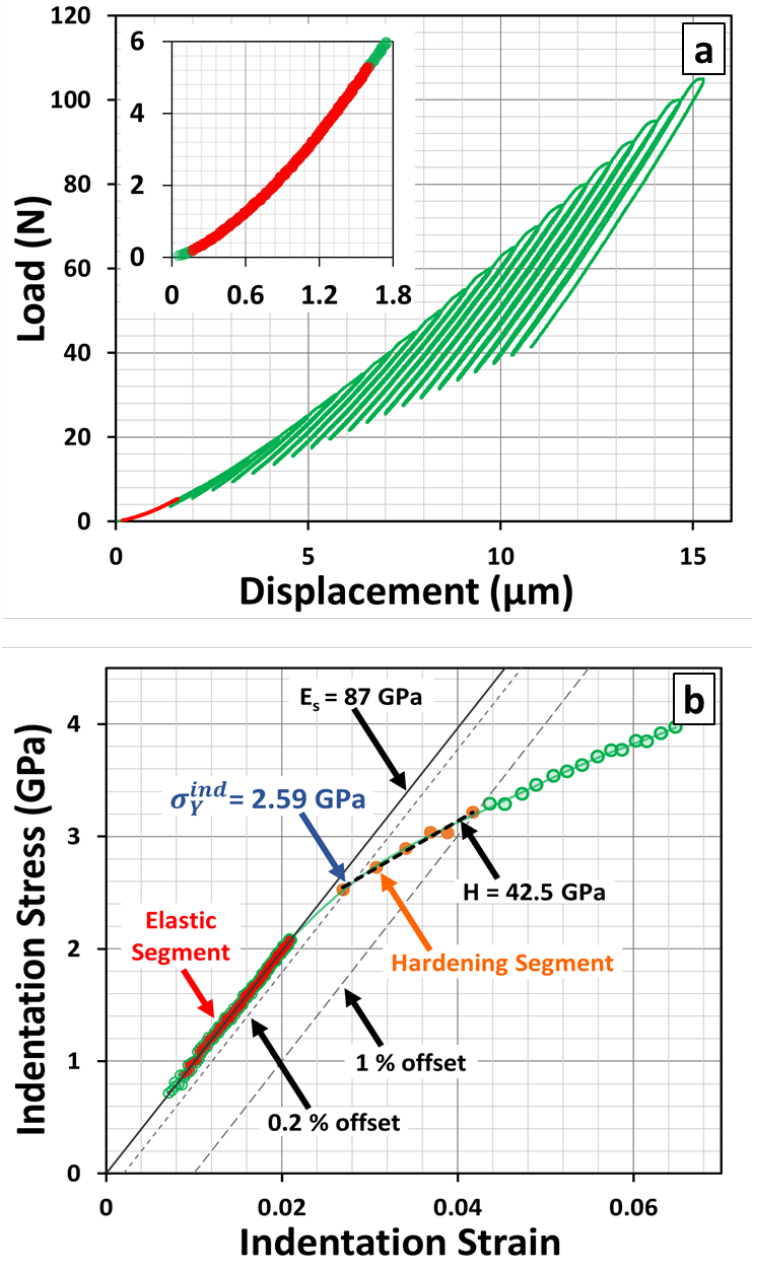

Figure 5.5: Example of microindentation load-displacement curve and its corresponding indentation stress-strain plots form sample DV1 The red data corresponds to the initial elastic segment used to determine the effective modulus.

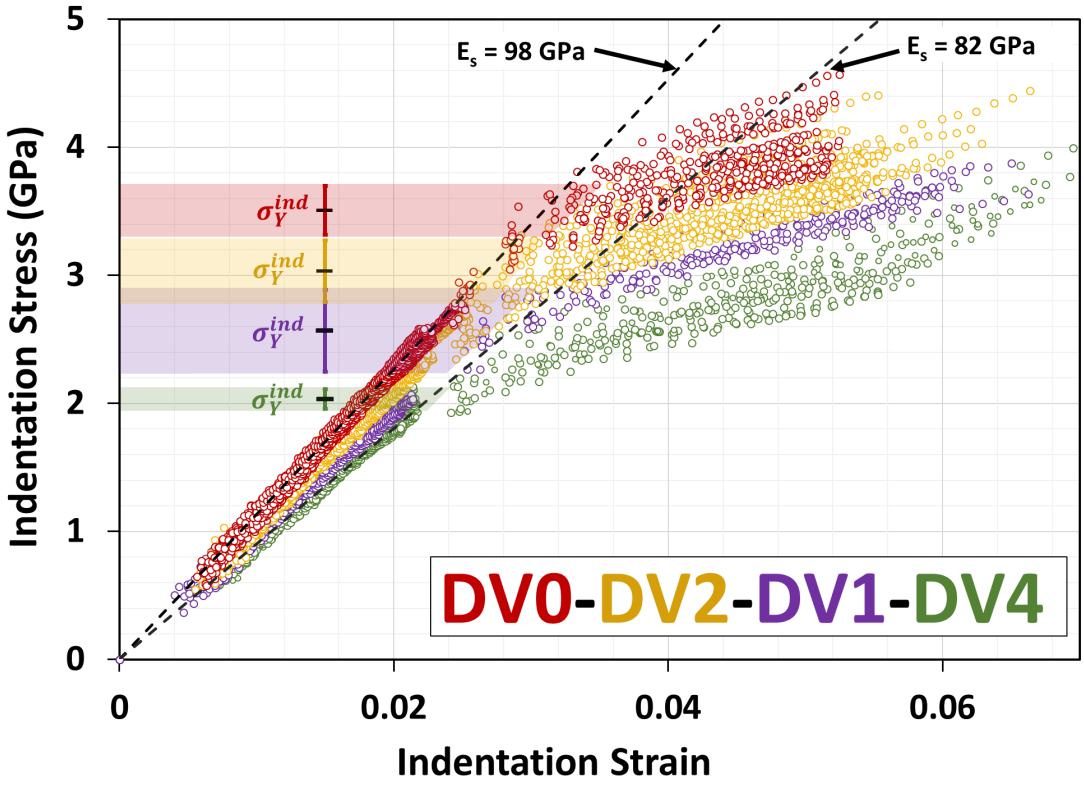

Figure 5.6: Indentation Stress-strain results for multiple microindentation tests on DV0, DV2, DV1, and DV4 samples. The average values for indentation yield and their variations from multiple tests are highlighted in different colors.

Comparing indentation yield strength measurements with tensile yield strength (0.2 % offset strain on both cases) on the same materials [274] indicates an consistent scaling factor of 1.85-1.9 for all tested BMG MCs. A similar scaling factor has been reported in prior experiments and simulations on other materials [95, 97]. As it was explained in Section 2.5, the scaling factor is attributed to the expected higher hydrostatic stress component in the indentation test compared to the simple uniaxial tests. Since it is important to know if the collected microindentation measurement can represent the bulk property of the material, the contact area at yield (0.2% offset) and at 1% plastic strain offset are reported in the Table 5-2.

Table 5-2: Summary of extracted properties from multiple indentation tests from microindentation on DV0, DV2, DV1, and DV4 samples

Sample	Glass Volume fraction, %	Indentation Modulus (E_s), GPa	Indentation Yield Strength (Yind), 0.2% offset, Gpa	Contact Diameter at Y_{ind} (2a)	Indentation Work Hardening rate (H), 0.2-1% offset, GPa	Contact Diameter at H (2a)
DV0	100	98.17± 1.70	3.51 ± 0.19	91.2 ± 6.2 (μm)	35.39 ± 3.17	152.2 ± 6.6 (μm)
DV2	43.5 ± 4.4	91.41 ± 4.51	3.03 ± 0.24	82.0 ± 7.9 (μm)	36.63 ± 3.11	143.2 ± 7.3 (μm)
DV1	36.0 ± 1.9	88.17 ± 4.57	2.52 ± 0.27	67.7 ± 11.5 (μm)	37.73 ± 6.13	130.3 ± 8.5 (μm)
DV4	14.8 ± 1.5	82.79 ± 3.25	2.03 ± 0.07	56.6 ± 1.8 (μm)	41.68 ± 4.54	127.8 ± 10.0 (μm)

The variances reported in Table 5-2 for the different properties carry important information. This variance is correlated to the variance in the material state in the indentation probed material volume (known as the primary indentation zone) in the multiple tests conducted on each sample. As explained in the indentation protocol's section (Section 2.3.3), the contact radius at any of the points on the indentation stress-strain curves can be estimated by Equation (2.18). The red grids on Figure 5.4 (approximately 80μm×80μm for the case of DV1 alloy) represent an approximate size of indentation zone at yield point. As evident, the indentation zone at yield is large enough to include large number of both phases. However, local heterogeneity in the microstructure exists at this scale, and as a result sample with highest heterogeneity (DV1) and lowest heterogeneity (DV4) are expected to have largest and smallest variation in measured indentation yield strength values. The same trend is observed for the measured microindentation results. Nevertheless, the average values from multiple tests at different locations represent bulk mechanical responses of the studied materials.

For example, the percentage variance (normalized by the mean) is the highest in the hardening rates and lowest in the modulus values. This is because the hardening rates are much

more sensitive to the distribution of defects in the indentation zone compared to the strength values, which in turn are more sensitive compared to the modulus values. It is also observed that DV1 exhibited higher values of variance compared to the other three samples. This is because the microstructure features in this sample show a higher level of heterogeneity (see Figure 5.1).

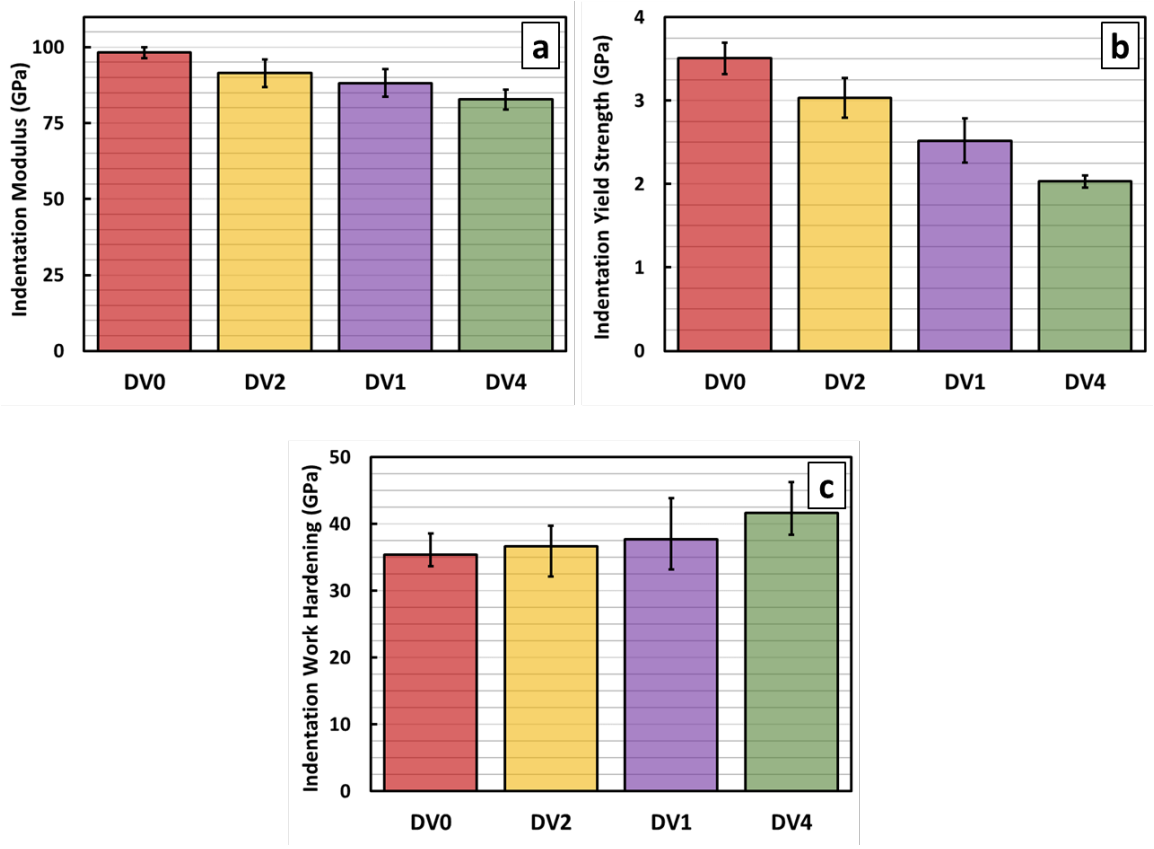

Figure 5.7: Extracted properties (a) indentation elastic modulus, (b) indentation yield strength, (c) indentation work hardening form multiple microindentation tests.

Next, we turn our attention to mechanical responses of individual phases using the smaller indenter tips. The main challenge in this step is to locate indentation on each phase and assure the indentation primary zone will not be affected by the other phase. In order to get the response solely from one phase, we identified largest islands of that phase in the microstructure, and performed the test in the center of the island. Therefore, it is highly possible that indentation primary zone does

not extend to the other phase. Also, we used high resolution SEM images with conjunction of optical images to precisely place the indenter tip. Examples of these measurements are presented in Figure 5.8 for both crystalline and amorphous phases. The load-displacement curves (Figure 5.8(a)) show different responses for the glass and the crystalline phases which are depicted in red and blue colors respectively. Although the transition from elastic to plastic regimes is not well-defined from the indentation load-displacement data, it is rather obvious in the indentation stress-strain curves. In the example curves shown in Figure 5.8(b), the indentation moduli were established as 111 and 71 GPa for glass and crystalline phases, respectively. Similar to previous chapter, the 0.2% strain offset has been used for defining the indentation yield strength in these measurements. In addition, to be consistent with data in microindentation, indentation work hardening were extracted from the slope of a line fitted to the data after yield point up to 1% plastic strain.

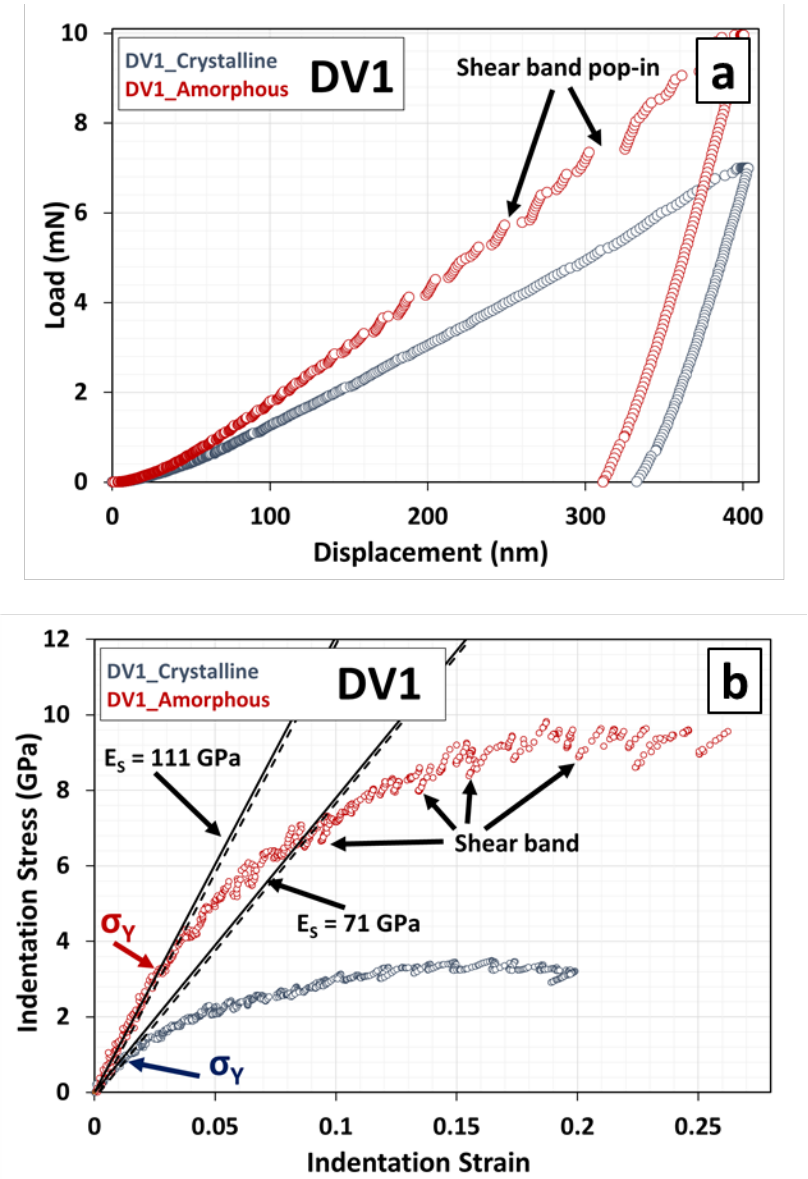

Figure 5.8: Example nanoindentation tests on crystalline and amorphous regions and their corresponding indentation stress-strain curves.

An important observation from the nanoindentation measurements was that the load-displacement curves measured in the glass phase consistently showed serrations, which are attributed to the formation of microscale shear bands. Similar observations were reported in prior indentation studies on different metallic glass alloys [276-284]. However, majority of the previously reported studies reported hardness values. In the protocols employed in this work, the

serrations appear as drops in the indentation stress (see Figure 5.8(b)) allowing a more direct and meaningful comparison of the responses from the different samples which will be discussed later in this section.

As one can see in Figure 5.8(b), there is indeed a significant difference in the mechanical responses of the crystalline and the glass phases. The difference is also reflected in the residual imprints of the indentations in Figure 5.9 (a) and (b) for crystalline and glass phases respectively. The indentations in the crystalline phase show slip traces around indentation imprint, while in the case of glass phase different features, known as shear bands, appear at the indentation area. From the observation, shear bands in the glass phase do not show any preferred directions as there is no atomic order in the amorphous phases. It is also evident from Figure 5.9(a) and (9b) that the plastic deformation does not expand far away from the indentation imprint for glass phase compared to those in the crystalline phase.

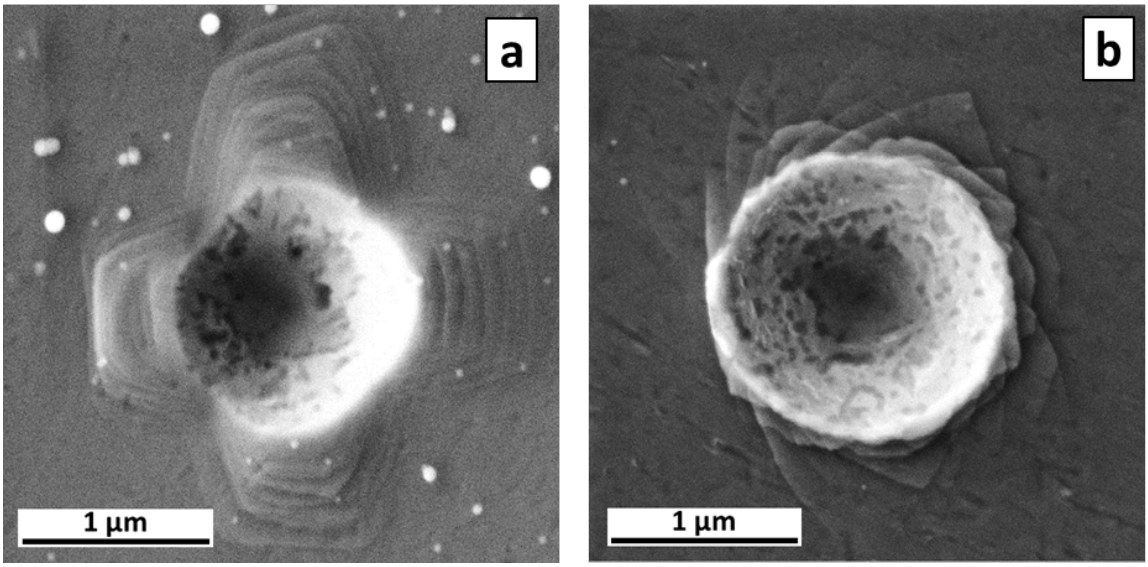

Figure 5.9: SEM images of indentation imprints on (a) crystalline phase and (b) glass phase using 1 µm indenter size. The indentation imprints are surrounded by slip traces at certain directions in the crystalline phase and shear bands with no orientation preferences in the glass phase.

In order to get statistical assessments on mechanical responses of each individual constituent, multiple nanoindentation tests (15-30 tests) were carried out on each phase. The means and standard deviations of the measured indentation elastic modulus, indentation yield strength, and the indention work hardening for both amorphous and crystalline phases in all alloys are summarized in the Table 5-3. In addition, the indentation contact diameter at 0.2% offset strain as well as 1% plastic strain are included in the table.

Table 5-3: Extracted indentation properties from 1μm indentation tests on each individual constituent in DV0, DV2, DV1, and DV4 alloys

Sample	Indentation Modulus (E_s) , Gpa	Indentation Yield Strength (Yind), 0.2% offset, GPa	Contact Diameter at Y_{ind} (2a), nm	Indentation Work Hardening rate (H), 0.2-1% offset, GPa	Contact Diameter at H (2a), nm	Indentation Stress at First Pop-in, GPa
DV0 -Amorphous	106.8 ± 4.2	3.09 ± 0.30	217.9 ± 58.8	73.81 ± 9.09	298.7 ± 74.9	5.94 ± 0.70
DV2 - Amorphous	101.95 ± 4.19	3.01 ± 0.43	160.1 ± 24.9	73.654 ± 9.64	240.5 ± 37.9	5.74 ± 1.05
DV2 - Crystalline	70.51 ± 2.87	1.18 ± 0.24	157.0 ± 39.1	39.50 ± 4.87	243.2 ± 55.7	-
DV1 - Amorphous	112.11 ± 6.33	3.40 ± 0.28	129.6 ± 16.4	75.14 ± 11.71	169.8 ± 17.9	6.57 ± 1.36
DV1 - Crystalline	69.09 ± 4.27	1.05 ± 0.18	137.4 ± 44.9	37.80 ± 7.03	206.1 ± 51.5	-
DV4 - Amorphous	113.22 ± 5.91	3.24 ± 0.32	136.4 ± 14.9	77.88 ± 10.7	201.9 ± 24.1	7.67 ± 1.17
DV4 - Crystalline	73.75 ± 4.26	1.15 ± 0.24	118.7 ± 52.7	47.16 ± 5.4	225.8 ± 75.6	-

The extracted mechanical properties of each phase are compared in Figure 5.10 where the indentation data for amorphous and crystalline phases in DV2, DV1, and DV4 alloys are normalized with the values measured from the fully glass alloy (DV0). For different compositions, the ratios are very similar showing that the composition does not have major influence on the mechanical properties of each constituent. These ratios are 0.95-1.05, 0.97-1.09, and 0.99-1.05 for indentation elastic modulus, indentation yield strength and indentation work hardening. Another way to see the data is by looking at average and standard deviation of all indention results on

crystalline and amorphous phases separately. The statistics are 107.26 ± 6.48 GPa, 3.14 ± 0.37 GPa, 74.66 ± 9.93 GPa for indentation elastic modulus, indentation yield strength and indentation work hardening of amorphous phase altogether. Similarly, the corresponding values are 71.02 ± 4.06 GPa, 1.14 ± 0.23 GPa, 41.17 ± 6.77 GPa for all nanoindentation tests on crystalline phase. Small standard deviation (less than 10% of mean values) indicates that the local composition does not have significant influence on the mechanical response of each constituent. On the other hand, the atomic arrangements seem to have large impact on the mechanical responses. For the glass phase, the indentation elastic modulus, indentation yield strength and indentation work hardening are about 1.51, 2.75, 1.81 are higher than corresponding properties in crystalline phase. The higher yield strength of amorphous phase compared to crystalline one is because of the absence of defects that exist in crystalline materials, such as dislocations and grain boundaries. However, unexpected higher indentation work hardening values in glass phase compared to crystalline one should be related to the deformation mechanisms in amorphous phase at the early stage of deformation which will be discussed later.

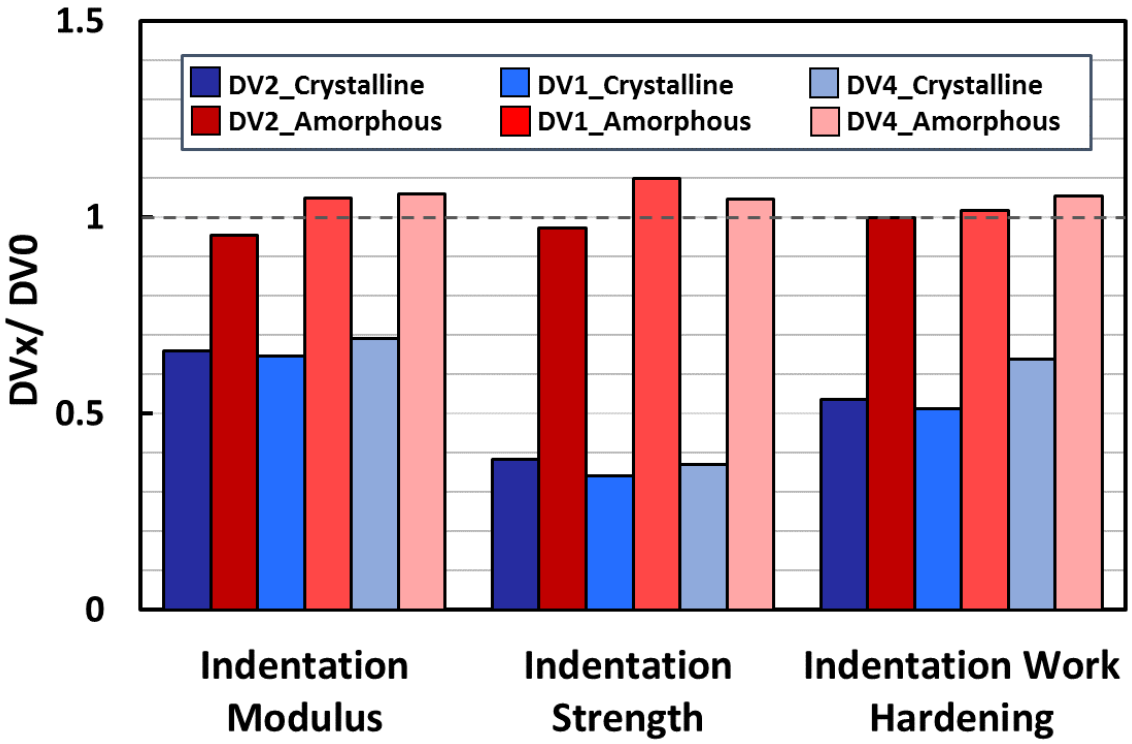

Figure 5.10: Indentation modulus, indentation yield strength, and indentation work hardening from crystalline and amorphous phases in BMG MCs (DV2, DV1, and DV4) normalized by the similar properties from BMG alloy (DV0).

In order to see how individual phase properties contributes in overall bulk properties, the indentation measurements for both indenter tip sizes are plotted together for all four compositions in Figure 5.11(a-d). In each plot, nanoindentation tests on glass phase (red), and on crystalline phase (blue) are plotted with all microindentation tests (black) on the same alloy. To assist reading the plot, the average and standard deviation of the indentation yield strength for each phase and the bulk measurements are included as horizontal bands.

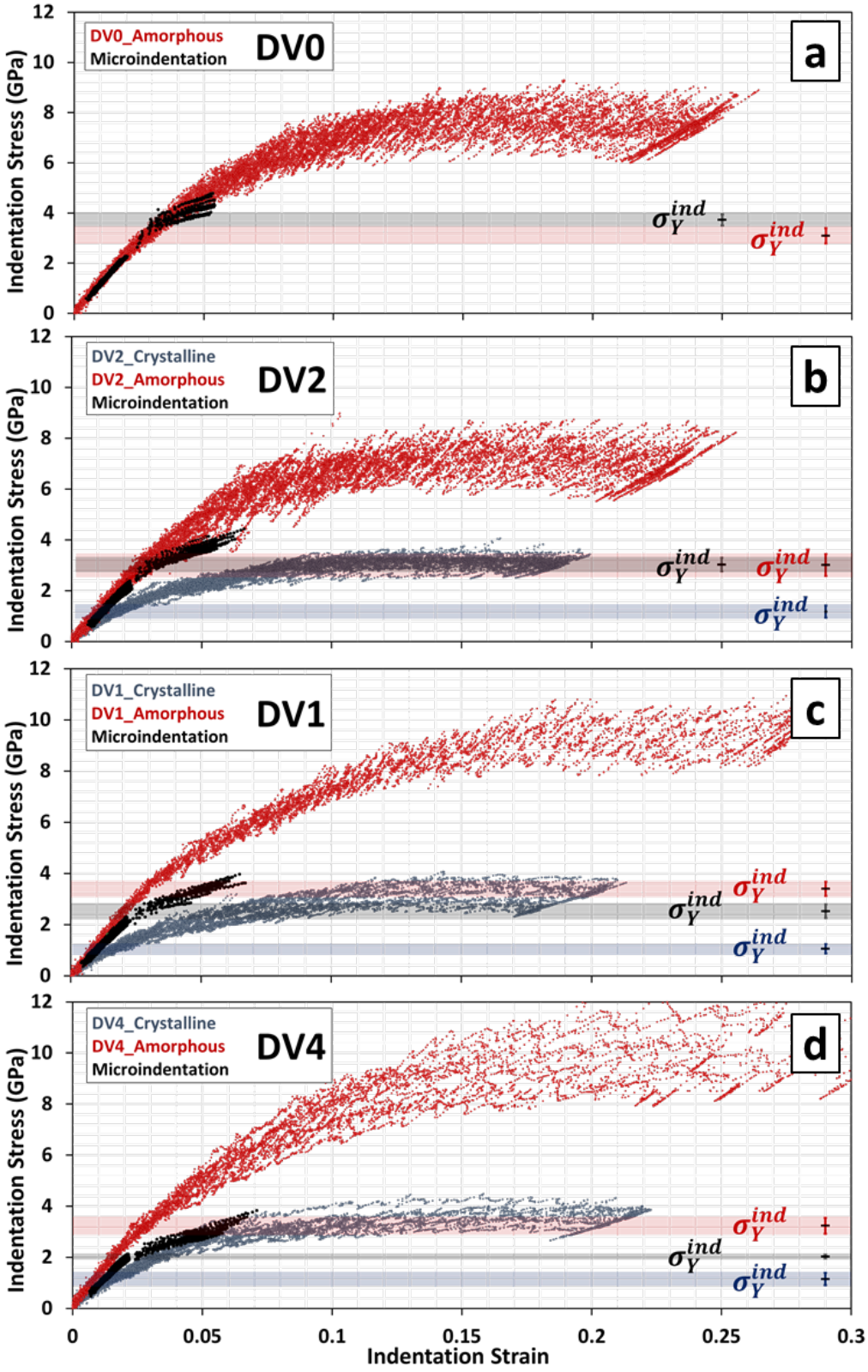

Figure 5.11: Comparison mechanical responses of individual crystalline and amorphous phases from nanoindentation with mechanical bulk responses from microindentation

From this figure two observation can be highlighted, 1) increasing volume fraction of amorphous phase increases the bulk strength of the material. From DV4 which contains ~15% glass phase to DV0 with ~100% glass phase the bulk indentation yield strength increases from 2.03 ±0.07 GPa to 3.51 ± 0.19 GPA. The corresponding black curves remain between nanoindentation curves of glass and crystalline phase. The higher glass content the closer the black curves to the red ones. 2) In fully glass sample, DV0, indentation curves from 1 and 500 μm tip radius are very similar but the average indentation yield strength from microindentation are ~10% higher than the average values form nanoindentation which can indicate a size effect phenomenon. This will be discussed later when the deformation mechanism in amorphous phase is described.

The BCC crystal structure has been studied in the past for different material systems, and deformation mechanism is well known. Since the past study shows small anisotropy in BCC crystal system, no attempts were made to evaluate orientation anisotropy in the crystalline regions. However, we tried to conduct indentation tests on several locations on the sample with minimum distance of few millimeters to assure indentation results are from different and random orientations of crystalline phase.

Hence, our focus in this part is on glass phase to provide detailed insight on the deformation mechanism in amorphous materials. Since amorphous materials lack long-range atomic orders, the common slip system mechanism in crystalline material is not applicable. Instead, the glass phase is expected to deform plastically by local rearrangement of atoms to accommodate shear strain. Two potential models have been laid out to facilitate this shear strain: shear transformation zone (STZ) [260, 285-287] and free-volume model [260, 279, 288]. The STZ assumes an inelastic shear distortion in the matrix by sudden movement of a group of atoms from one minimum low energy configuration to another one. The free-volume model is based on discrete jumps of atoms into the sites with high free volume. In both cases, the metallic glass deformation is influenced by the local distribution of free-volume, the higher free-volume in the glass structure, the easier accommodation of local shear strain [254, 276, 285, 289, 290]. More details of these two

models have been discussed widely in literature [254, 261, 262, 267, 268, 276, 286, 287, 291-296]. As a result of these deformation mechanism, microscale local deformation known as shear bands are observed in metallic glasses which attributes to decrease of local viscosity. Summarizing these mechanisms as a) flow dilation which results in local formation of free volume, b) shear transformation zone (STZ) which changes local structural atomic order, and distribution of internal stress, and c) local heating.

Several prior studies have reported nanoindentation measurements on metallic glass and analyzed the serrations in the load displacement curves to estimate the size and the activation energy of STZs [254, 276, 297]. Most of these studies employed a sharp Berkovich tip. Consequently, one should expect plasticity to initiate locally, immediately after contact. However, in most previously reported studies [276], the first observable serration (also called pop-in) is assumed to correspond to the initiation of plasticity in the form of microscale shear bands. This assumption seems to be widely adopted by the community on all length scales without any supporting evidence.

The protocols employed in the present study allow rigorous analyses of the indentation measurements. As is already clear, the use of a spherical indenter allows us to extract a clear elastic regime in the indentation stress-strain curve, which then follows with a clear transition to the plastic regime. However, our measurements indicate clearly that the plastic flow initiates in the sample well before the start of the serrations. Employing a criterion of a minimum 1 nm displacement burst as an indicator of shear band formation, we identified individually all the pop-ins (i.e., serrations; see Figure 5.12 (a)) and recorded the corresponding indentation stress value (see Figure 5.12(b)). Three observations can be seen from the indentation stress-strain plots in the glass phase: (i) the first pop-in with 1 nm size criterion appears to form at a stress level much higher than the yield strength, (ii) plastic deformation after yield is accompanied with a significant amount of strain hardening, and c) pop-ins occur extensively after the first one suggesting that this is now the main mechanism of plastic deformation and dramatically reduces the strain hardening rates. It is

emphasized that the first two observations contradict directly the prevailing assumptions in literature.

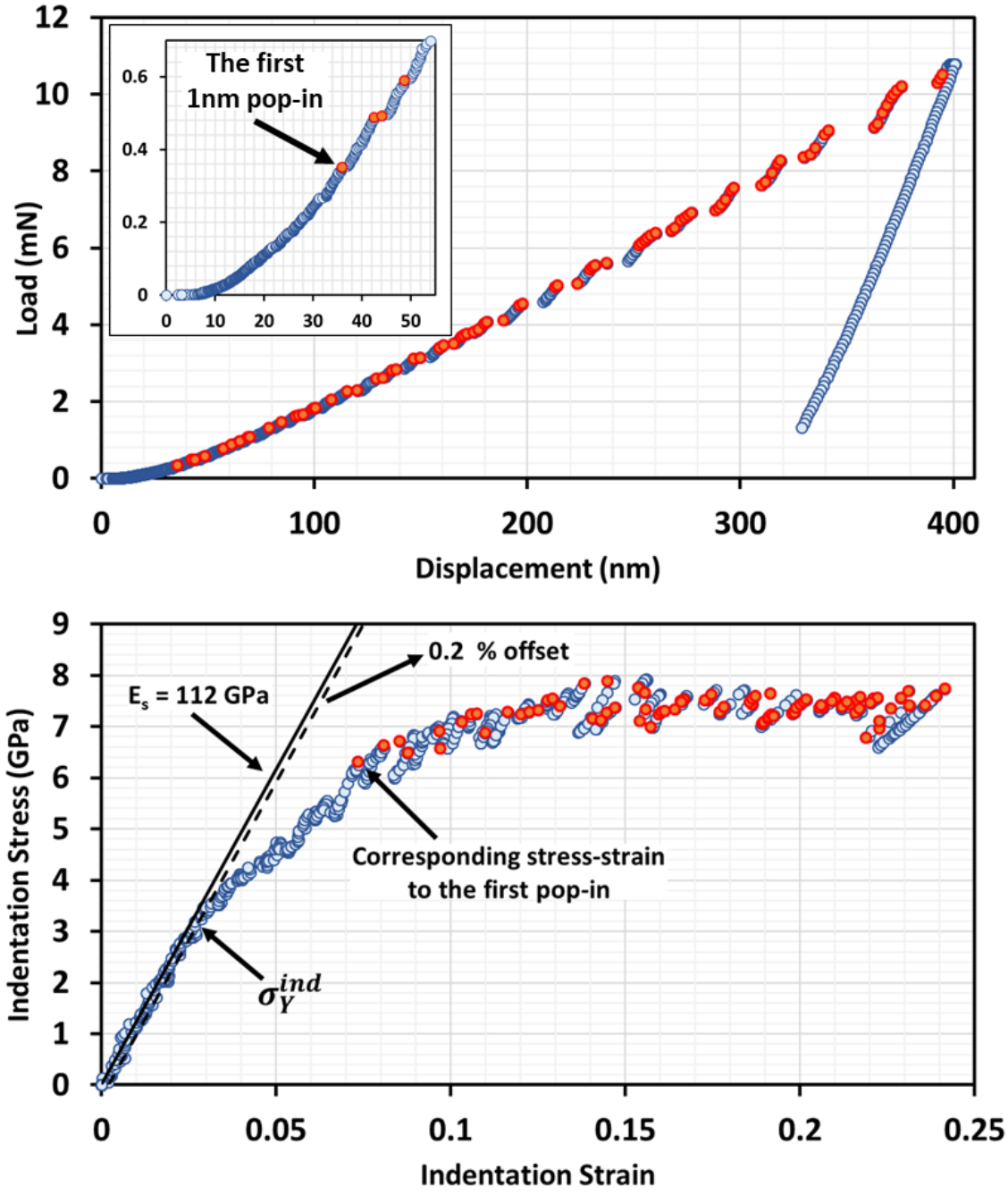

Figure 5.12: Example indentation load-displacement curve (a) from amorphous phase and its corresponding indentation stress-strain plot (b). The displacement burst larger than 1nm are considered as pop-ins in this study. The Red dots represent individual pop-in events throughout the indentation test both in load-displacement and indentation stress-strain plots.

Statistical analyses of the shear banding events provide a deeper understanding of the measurements. For this purpose, a total of 7800 pop-in events was investigated in this study. Following analyses protocols used in current literature, the size of the displacement burst (referred as pop-in length) for all shear band events were plotted with respect to the pop-in load for all four tested materials in Figure 5.13 (a-d). There is no clear correlation in these plots, suggesting that the pop-in event is completely stochastic and can happen at any indentation load level. However, when the pop-in statistics are analyzed in the form of indentation stresses, the correlations hidden in the raw data are revealed (see Figure 5.13(e-h)). Note that no pop-in has been observed below 4 GPa over the very large number of pop-ins analyzed. The average indentation yield strength for each of the four samples is plotted as a dashed line (located on the left side of the pop-in data points) with the shaded region identifying one standard deviation. In the same plots, the average indentation stress at which the first pop-in occurs is plotted as solid lines, with the shaded regions depicting one standard deviation again. These results prove clearly that the observation of indentation pop-in is not an indicator of yield in amorphous material. In another word, contrary to what has been widely accepted in current literature, shear band formation does not correspond to the onset of plastic deformation in the glass phase in these samples.

As one can see in the Figure 5.13 (g and h), the indentation stress for pop-in events spreads to higher indentation stress levels. In other words, the indentation stress-strain curves for these samples were not showing a plateau, and the indentation stress increases as indentation progresses. Even though, we tried to perform indentation on the center of glass islands to assure the glass phase extents far enough underneath, the possibility of being influenced by the neighboring crystalline phase and its interface is more likely in the case of DV1 and DV4 samples where smaller volume fractions of glass phase exist.

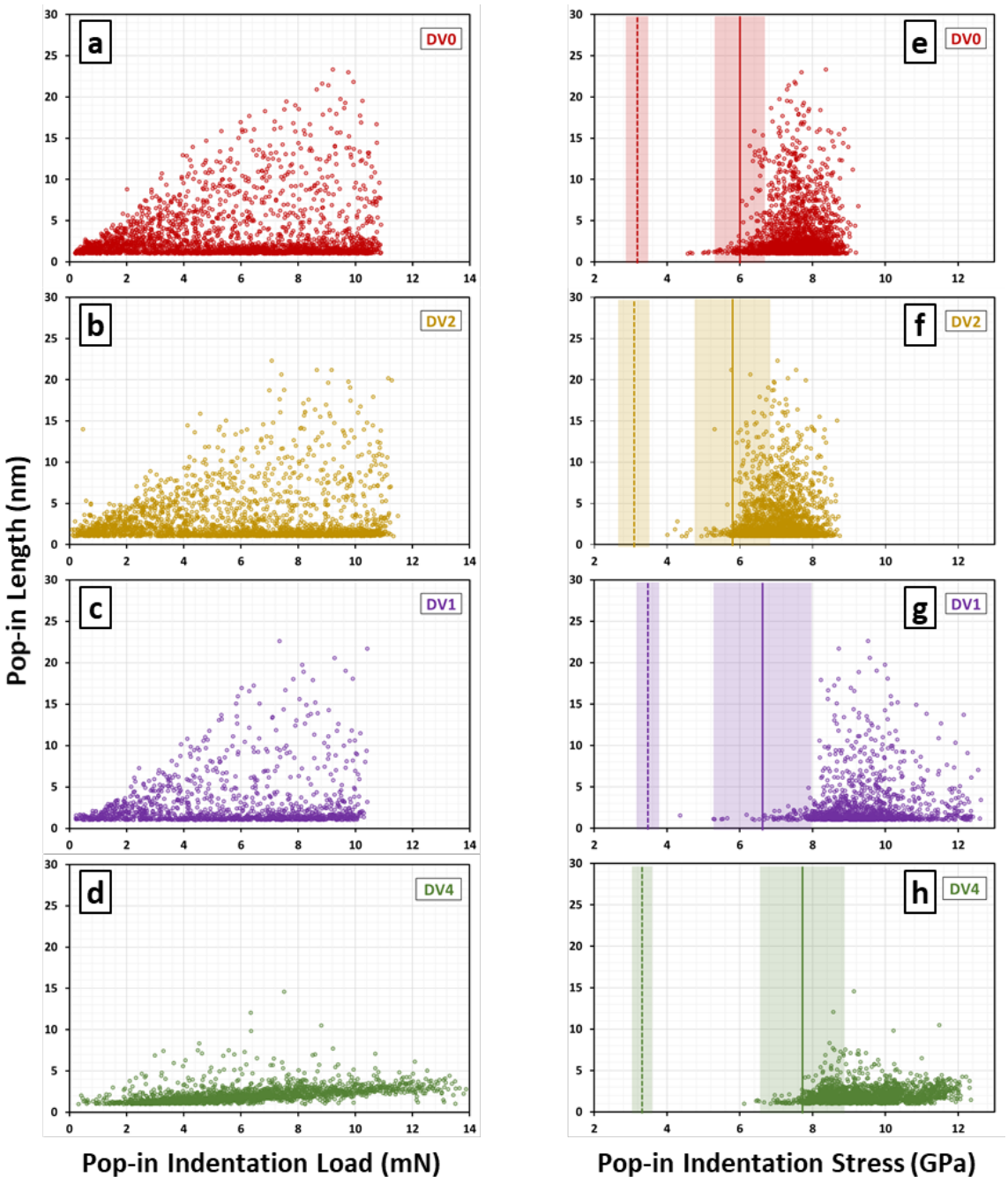

Figure 5.13: The length of the pop-in events occurred during indentation tests respect to their corresponding indentation load (a-d) and indentation stress (e-h). The vertical dashed lines represent the average indentation yield strength with shaded surroundings as one standard deviation. The vertical solid lines represent the average value of the indentation stress of the first pop-in and the first standard deviation as the shaded areas.

The other way of presenting pop-in data is by calculating the cumulative distribution function (CDF) for the pop-in stress and normalized stress (by the indentation yield strength) are presented in Figure 5.14 (a and b) for all 7800 pop-in events. For the purpose of better illustration, the plots were diluted to show only 5% of the data points. It is seen the distributions of pop-in stress for DV0 and DV2 (high glass volume fraction samples) are very similar to each other, as are the distributions for samples DV1 and DV4 (low glass volume fraction samples).

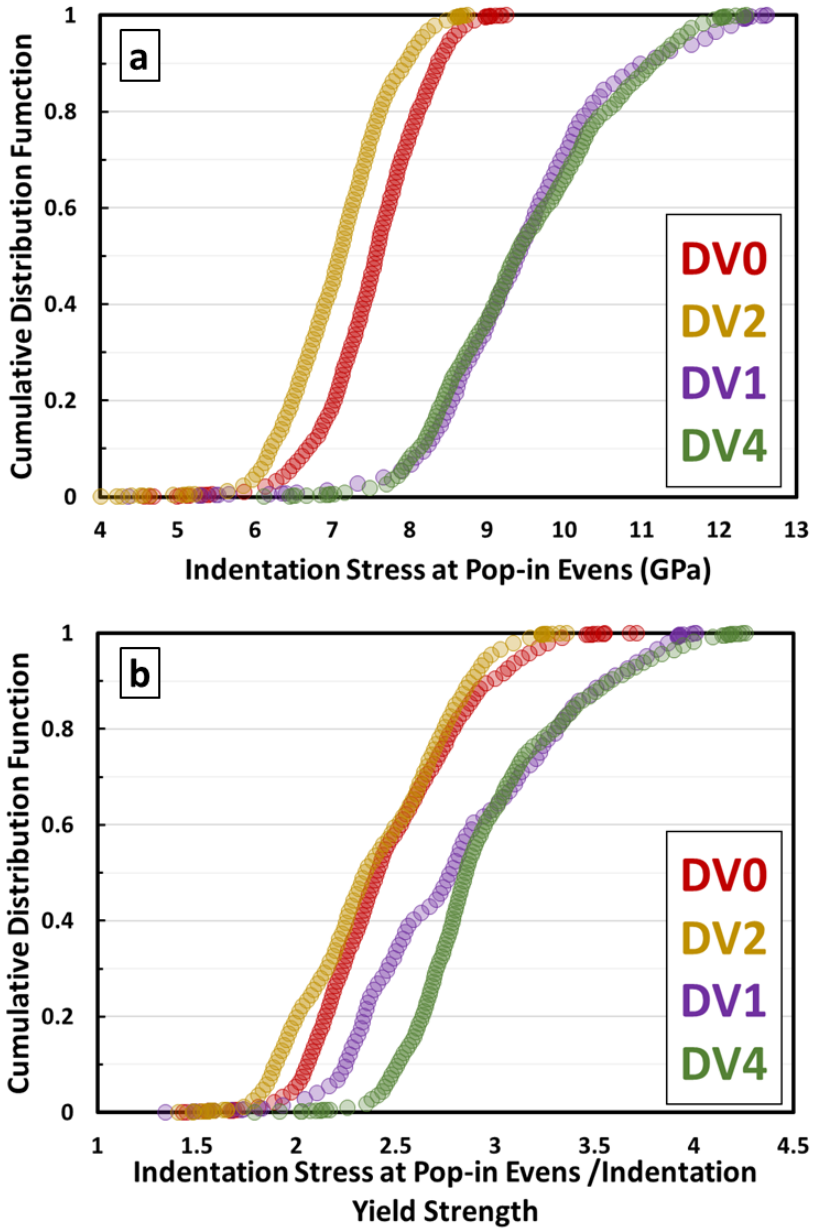

Figure 5.14: Cumulative plots showing statistics of pop-in events occurred during nanoindentation tests.

Indentation stress-strain plots presented here provide deeper insights into the plastic deformation mechanisms in amorphous materials. As described earlier, the plastic deformation of amorphous materials depends on the characteristics (such as amount and spatial distribution) of free volume. The free volume continuously evolves during the imposed loading. In the initial loading in the elastic regime, one does not expect significant changes in the free volume, resulting in the linear response. As higher stresses are applied, the shear stress on the atoms forces them to find "close" lower energy morphological configurations (this might include filling any available neighboring vacancies). However, the shear field is not sufficient to result in massive movement of atoms to form shear transformation zone (STZ). At this stage of the deformation, discrete jumps of individual atom into the sites with high free volume is more likely and results in decreasing free volume. Continuing increase in load, more free volume annihilates and makes a small possibility for atoms to find a free volume in their neighborhood thus high work hardening is expected. Another possible mechanism for observed strain hardening is formation of local nano-crystalline phase during loading [263, 269, 271, 298, 299]. This observation is more significant in nanoindentation where very small volume of material is probed. The effects of the discrete atomic jumps into free volume is very negligible in the material volume undergoing deformation in uniaxial testing therefore it is not surprising not seeing the strain hardening on large scale testing. In contrary, the probe materials in indentation is much smaller and therefore effect of the discrete atomic jumps becomes more significant in the indentation response. This response has been never observed on previous indentation studies because of high level of plastic deformation and lack of a robust detecting protocol in finding effective surface contact.

At a stress threshold where the rate of formation of free volume exceeds the annihilation rate, extensive free volumes form in the matrix and results in shear band formation where local rearrangements of groups of atoms take place to accommodate shear strain. As a result, STZs are activated in the volume of probed material under indenter and thus causes stress relaxation that

appears as stress drops on stress-strain curves. Any time that rise in stress reaches the threshold again, more STZs form and result in successive shear band formations. This process causes a plateau in the stress-strain plot (almost zero work hardening).

5.4. Establishing process-structure-property linkages in multiphase metals: Application to BMG MCs

Similar to previous study on DP steel, in this section we explore the application of the high throughput indentation testing and microstructure quantification (2-point statistics and the PCA analysis) to establish PSP linkages for BMG MCs materials. As shown in previous section, microindentation tests deliver bulk response of the Ti-based BMG-MC system form very small volume of material and in a high throughput fashion. Another obstacle in development of bulk metallic glass composite is utilizing outdated standards in quantifying the microstructure despite availability of advanced tools in collecting and quantifying microstructure. In all current protocols, simple measures of the microstructure such as averaged elemental composition, volume fraction of glass phase, dendrite size and spacing are used. The most common approach in quantifying cast structure is measuring interdendritic space [300-305]. However, this simple descriptor is inadequate in quantifying the very complex microstructure of cast samples. In contrary, as discussed in Section 3.2, techniques such as 2-point correlations provide full description of a microstructure and can capture all salient features.

In selecting a microstructure characterization technique, we need to consider two criteria: (i) ability to capture important microstructural features at desired spatial resolution, and (ii) ability to collect data in the shortest possible time (i.e., high throughput). Considering dimensions of features in Figure 5.1 and uniform distributions of the elements in both crystalline and glass phases (see Figure 5.2), we decided to use the backscattered electron (BSE) signal in SEM in order to establish a reliable PSP linkages. Therefore, selecting glass and crystalline phases as two local states is the logical choice since they carry all microstructural attributes required to produce

reduced-order linkages between the microstructure and the local properties. Similar to the discussion in case of the DP-steel, including the lattice orientations of the crystalline regions as a local state variable will result in dramatic increase in computational cost in microstructure quantification. The main reason that lattice orientations of crystalline phase are not considered in the 2-point statistics calculation is because of the fact that cast samples does not have crystallographic textures and in addition, no further plastic deformations were applied that make the contribution of crystal orientation necessary.

As evident in SEM images shown in Figure 5.1, a high contrast exists between crystalline and glass phases because of segregation of heavier elements into glass phase. The contrast between glass and crystalline regions in BSE images are high enough that a simple thresholding results in a very good segmentation shown in Figure 5.15 (d-f). Since in this section we are establishing PSP linkages by using microindentation results, the dimensions of the image correspond to the estimated indentation contact diameter at the yield point reported in the Table 5-2. As mentioned and explained in previous section, images are collected from much larger area around the indentation sites. The images from the indentation sites (highlighted in yellow in Figure 5.4) and the corresponding indentation yield strength will be used for establishing PSP linkages. However, the rest of the surrounding area was divided into many images with same dimensions as the one in center. These images are also segmented and analyzed by 2-point statistics. Using this approach, the short and long- distance variation in the microstructure will be considered in the calculation and as a result the bases of the final PC space are less sensitive to adding a new micrograph from these alloys.

Figure 5.15(a-c) shows examples of BSE images of DV2, DV1, and DV4 alloys with their corresponding images after segmentation (as described above, each voxel in the microstructure is assigned to one of two local states: crystalline (colored as black) and glass (colored as yellow) shown in Figure 5.15 (d-f). After segmentation, we employed the framework of 2-point statistics on each image. The corresponding computed 2-point statistic of the example images are presented

in Figure 5.15 (g-i) as autocorrelation of crystalline phase (colored black). These 2-point correlation maps contain a large amount of morphological information of each phase that are hidden in the dataset. This information can be analyzed to extract distribution parameters such as volume fraction, size, and spacing. For example, the peak value at the center of the autocorrelation maps is the volume fraction of the crystalline phase in that micrograph. As it can be seen the volume fraction of crystalline phase is 52, 64, and 85% for DV2, DV1, and DV4 alloy respectively. In addition, more details about the shape and morphology of the crystalline phase can be found in the contours in the center of the autocorrelation plots.

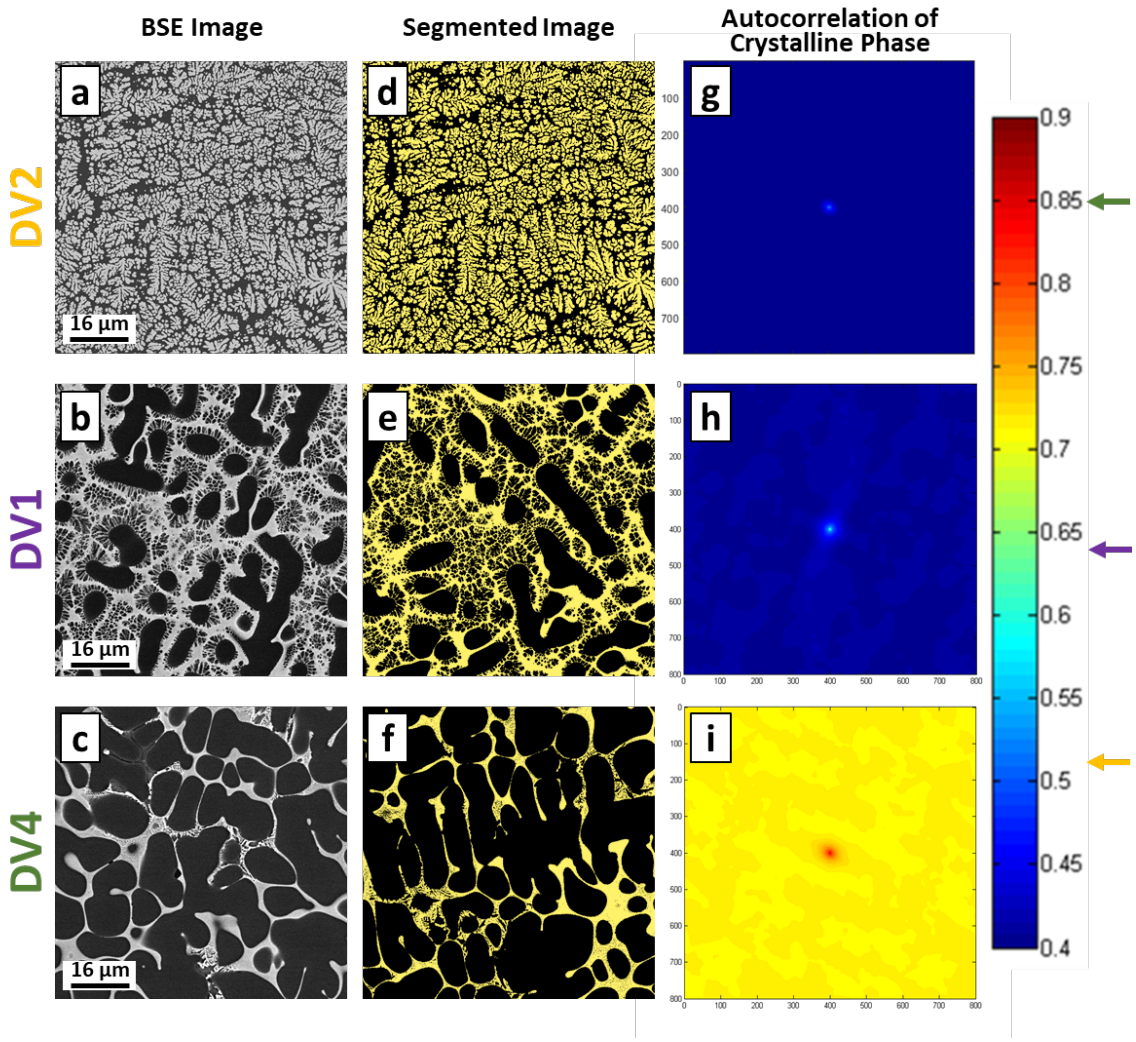

Figure 5.15: Example BSE-SEM images from the sample DV2, DV1, and DV4 (a-c), the corresponding segmented images with crystalline phase colored in black and glass phase colored in yellow (d-f). Corresponding computed 2-poin autocorrelation of black regions (g-i).

As demonstrated before, the computed 2-pint statistics results in a very large vector of descriptors for each microstructure (considering the size of 1170×1170 pixels for an image with dimensions of 80 µm×80µm). For the present case study, with the procedure described, a total number of 3,594 images are considered in our analysis for the alloy DV2, DV1, and DV4. After 2-point statistics were calculated on all images, the PCA was performed to sort microstructure features from high to low contribution in the microstructure variation.

Figure 5.16 shows all the 3,594 microstructures in this study in the reduced dimensionality space for the first three PC scores, PC1, PC2, PC3. As it can be seen in this figure, each class of DV alloys are separated in different clusters while conventional approaches based on volume fraction fail to distinguish these differences (see Figure 5.17). Indeed, there exists variance in each class. In this plot, the closer two points to each other, the more similar microstructure they have. Furthermore, as one should expect from PC analysis, the PC1 has the highest variance and then the PC2 has the second highest variance, and the variance decreases for higher PC scores. Also, one should note that we defined the fully amorphous sample (DV0) as the origin of the PC space. Therefore, generally it is true that a point (a microstructure) located further from the origin contains more crystalline phase.

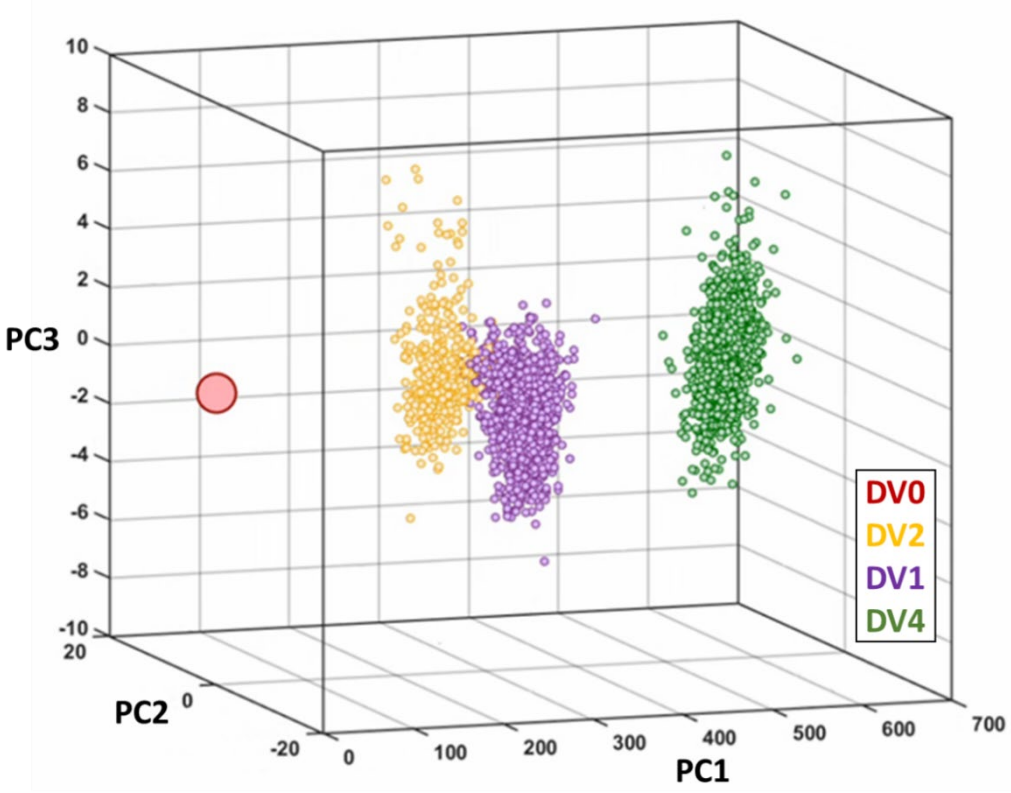

Figure 5.16: Low-dimensional representation of the entire 3,594 micrographs obtained from PCA, colored by the different processing histories.

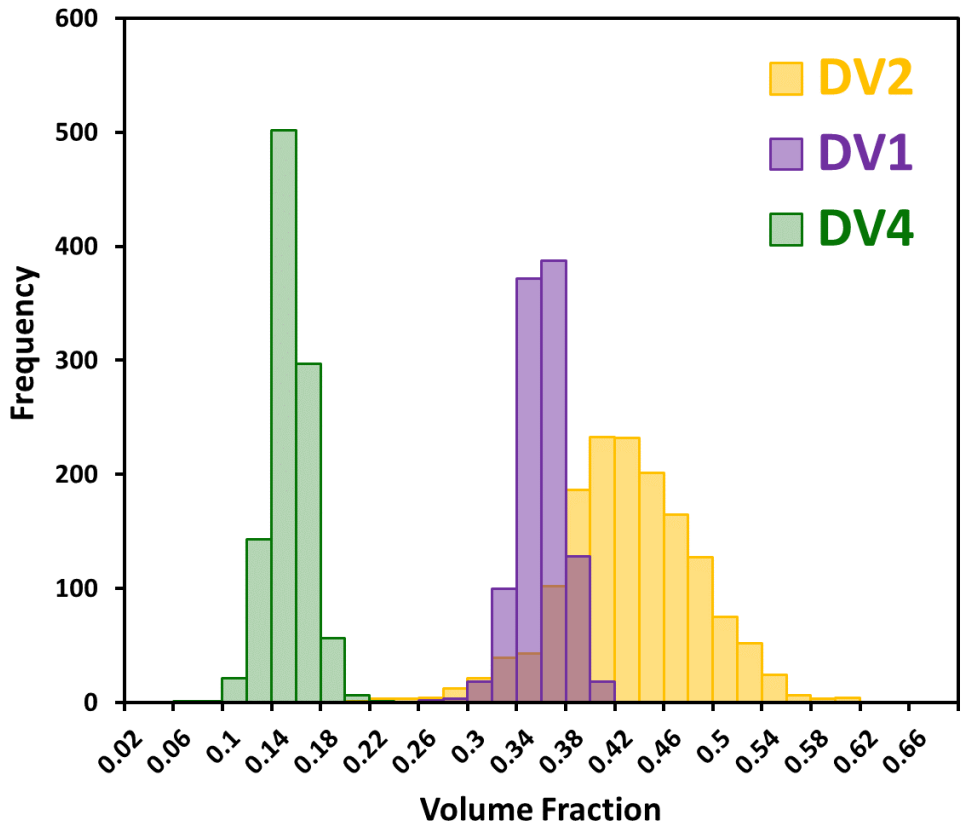

Figure 5.17: Volume fraction distribution for all 3,594 micrographs from DV4, DV1, and DV2 alloys showing poor separation between two last classes.

After dimensionality reduction by PC analysis, about 99.9% of the variance between all the different microstructures used in this study can be captured by first 5 PCs. Our next step is to build the PSP linkages based on the low dimensional structure representation. For this case study, the processing parameters are taken as the initial compositions. Therefore, the at% of Zr, V, Cu, and Be are used as process parameters (listed in Table 5-1).

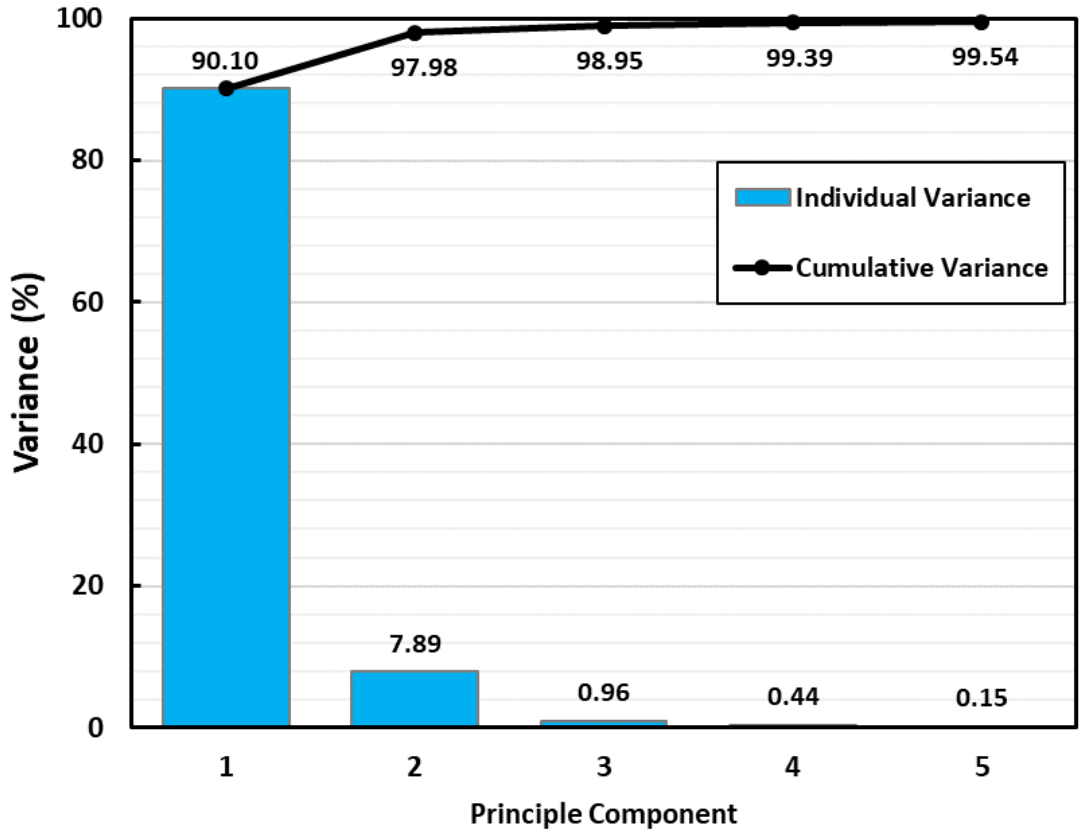

Figure 5.18: The individual and cumulative variances from the PCA for the first 5 principal components shows that PC1 and PC2 carry 98% of the total variance in the dataset.

To establish the process-structure linkages, we need processing parameters as inputs and then using least squares regression and cross-validation techniques to make prediction of the PC scores. In this study, the processing parameters are the atomic percentage of four alloying elements; zirconium (Zr), vanadium (V), copper (Cu) and beryllium (Be) elements. Since only the overall composition of each sample is collected, not the local composition within each image, the linkages must be established on the average value of the property and the ensemble average of the microstructure for each class of alloy. The number of provided samples are 3 while the number of predictors in the linkage is 4 (4 alloying elements), therefore there is a rank deficiency problem. Even if we try making the linkage because of this problem, the linkage will remain only mathematical equations with no accuracy and reliability. The only way to overcome this problem

is by having more sample composition or collecting individual EDS map for all 3,594 small images in this work. Similar process can be used in stablishing a structure-property linkage. The predicted property can be expressed as following linkage whose accuracy is presented in a parity plot in Figure 5.19.

$$\begin{aligned}\sigma_Y^{ind} = {} & 2747.216 - 1.134(PC1) - 166.959(PC2) \\ & - 1.985(PC1)(PC2) + 0.0246(PC1)^2 \\ & + 14.236(PC2)^2 + 0.009(PC1)^2(PC2) \\ & + 0.152(PC1)(PC2)^2 - 0.0001(PC1)^3 \\ & - 2.421(PC1)^3\end{aligned} \tag{5.2}$$

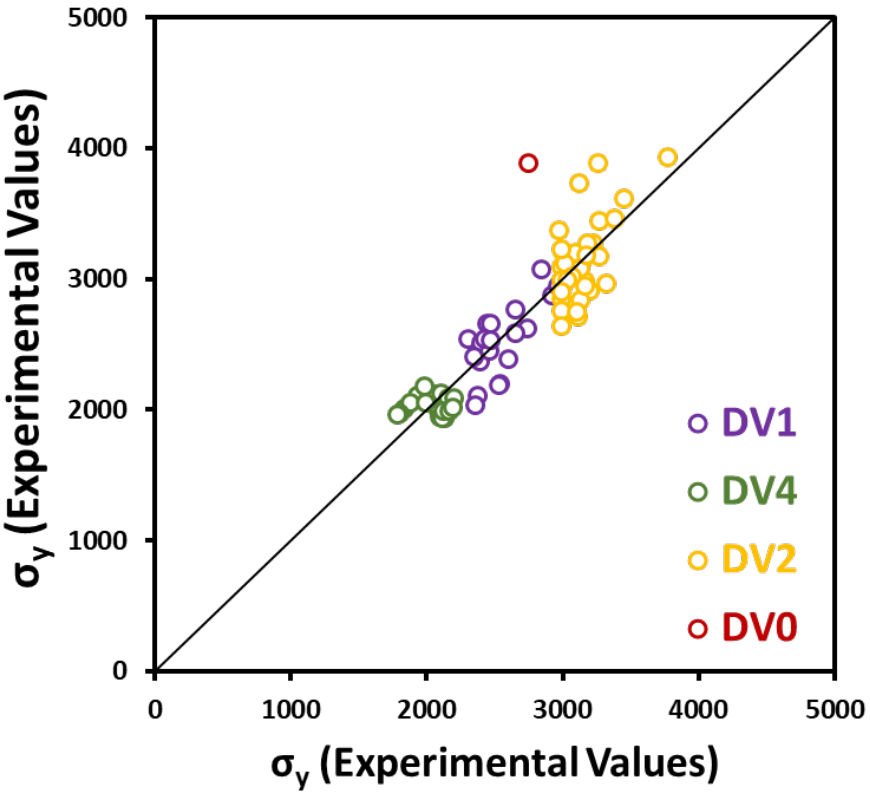

Figure 5.19: The accuracy of the structure–property linkage established in this work using data science approaches showing the measured and predicted indentation yield strength for different classes of the studied Ti-based BMG MC alloys.

The reader should note that the presented models here are data-driven. When new processing parameters are considered that results in very different microstructures, another PC analyses may need to be performed to update the new coordinate frame bases. Once sufficient numbers of data points from different processing parameters and different microstructures are considered in the analysis, the bases of the PC space will remain insensitive to new data points.

5.5. Summary

This chapter presents multi-length scale mechanical characterization of the newly developed Ti-Based BMG MCs alloys in a high throughput fashion. We have demonstrated the application of spherical indentation protocols in conjunction with 2-point statistics and PCA analysis protocol in establishing the process-structure-property linkages in this class of two phase materials. In addition, small length scale measurements were conducted by means of nanoindentation instrument on each individual constituent, amorphous and crystalline, phases in these alloys. This current work is indeed the first study of its kind that obtains statistically significant data at multi-length scales on actual structural composite alloys from very small coupons of material and with minimum amount of preparation time which tackle the costly process of statistical evaluation of the mechanical response for a new material.

The length scale study presented in this chapter provides new insight into plastic deformation of amorphous materials, while also providing enriched datasets for design, development, and deployment of BMG-MC alloys. Unlike other studies that employed expensive protocols, we have conducted large numbers of indentation experiments and utilized indentation stress-strain protocol to extract indentation stress at yield as well as pop-in events. Using this approach, we observed that the amorphous materials show very high hardening rate after yielding up to the first pop-in event. In addition, we found out that the first pop-in (using 1nm size criterion on displacement burst) appears to form at stress levels of about 1.8-2.1 times higher than the yield

strength. Pop-ins occur extensively after the first one suggesting that this is now the main mechanism of plastic deformation and dramatically reduces the strain hardening rates.

In addition to length scale effect, we have shown in this chapter that the spherical microindentation is a reliable high throughput tool for probing the changes in the bulk mechanical responses of Ti-based BMG MCs that is consistent with results from expensive conventional tensile test protocols. The application of microstructure quantification (2-point correlations and PC analysis) in conjunction with bulk mechanical responses from the high throughput microindentation protocol, provides a rigorous framework in establishing PSP linkages for Ti-Based BMG MCs. This framework in this chapter is extensible for a variety of other composite material systems.

Chapter 6 Conclusions

The case studies in the previous two chapters point mainly to the tremendous potential for developing and implementing high throughput assays in the exploration of PSP linkages in structural alloys. It is fully acknowledged that the term “high throughput” is being used here to signify the acceleration when compared to conventional approaches. We now review the main elements of the envisioned high throughput assays, and identify specific opportunities for future development.

One of the key elements of the high throughput assays described in the paper is in the use of instrumented indentation techniques for local measurements of mechanical response and their expression as normalized stress-strain curves. Indeed, the expression of the local mechanical response in the form of stress-strain curves is critically important for ensuring reliability and reproducibility of the measurements. Furthermore, the ability to conduct a large number of these tests at different length scales (by simply changing the indenter tip radius) even in a single sample, is clearly of major significance to multiscale modeling efforts. At the present time, this is the most practical approach for producing the large amount of experimental observations needed to calibrate the numerous parameters in multiscale modeling efforts [92, 93, 98]. However, in order to realize its full potential, additional work is needed in automation of this technique across all length scales of interest. As mentioned earlier, the experimental protocols are already fairly automated for the indentations conducted at the very small length scales. However, the experimental protocols for the indentations conducted at the larger length scales (indentation zone sizes covering multiple grains) are yet to be automated. The indentation stress-strain analyses protocols used in this work have been coded and are being prepared for broad dissemination as an open source software. While this software speeds up the analyses significantly, it still needs further development and automation. One other significant benefit of the indentation protocols is that they allow for parallelization. Indeed, several of the commercial vendors for instrumented indenters are currently exploring

concepts that allow for simultaneous indentation measurements on a grid (using multiple indenters simultaneously). Success in one or more of the concepts mentioned above will contribute significantly to the further development of the high throughput assays presented in this work.

A second key element of the high throughput assays described here is in the use of the emerging data science techniques for formulating the reduced-order PSP linkages. The efficacy is derived from the ability to template the workflows in ways that they can be applied to a broad range of material systems over a multitude of length/structure scales [68, 158, 306-309]. However, the use of a common template does not imply lack of flexibility. On the contrary, the modular approach comprising a specific sequence of steps involving a (i) digital representation of the microstructure, (ii) evaluation of microstructure statistics, (iii) low dimensional representation of the microstructure, and (iv) extraction of a reduced-order model allows for the development of highly efficient (high performance) computer codes leading to a systematic evaluation and objective identification of the best protocols. This is because the modern data science approaches allow one to establish a large number of possible workflow pipelines (utilizing the best available codes), push a large amount of data through these pipelines in parallelized efforts, and disseminate the findings in open source and open access repositories. As examples, in the case study presented in this work, one could evaluate a series of other choices for the digital representation of the microstructure (e.g., use other measures of local lattice misorientation or even the full information of the lattice orientation in the local state descriptors employed, use information gathered by other microscopy techniques), microstructure statistics (e.g., use chord-length distributions [310] instead of 2-point statistics), low dimensional representations (e.g., factor analysis [311], projection pursuit [312], independent component analysis [313]), and machine learning approaches (e.g., M5 model trees [314], support vector machines [315]). A further complicating factor in arriving at the most robust and reliable PSP linkages comes from the fact that the models produced in this approach are, to a significant extent, dependent on how much data is available (this is why these have been referred as data-driven throughout this paper). In other words, one should expect the best protocols and the

models to change as more data is added to the analyses (one can hope that the models stabilize after a critical amount of data has been employed – but in the interim one can still use the best available models at any time). Because of the very large number of choices one faces as well the significant cross-disciplinary expertise required for such a systematic evaluation, it is necessary to transition this pursuit from individuals, or even small groups of individuals, to a community-level curation effort. The data science workflows of the type presented in this work can lead this important transformation, and really accelerate the collection and curation of the PSP linkages for a broad range of materials systems of general interest to the entire materials science community [32, 33, 316, 317].

Chapter 7 References

[1] Materials Genome Initiative for Global Competitiveness., in: N.S.a.T. Council (Ed.) 2011.

[2] T.M. Pollock, J.E. Allison, D.G. Backman, M.C. Boyce, M. Gersh, E.A. Holm, R. LeSar, M. Long, A.C.P. IV, J.J. Schirra, D.D. Whitis, C. Woodward, Integrated Computational Materials Engineering: A Transformational Discipline for Improved Competitiveness and National Security, The National Acamedies Press, Washington DC, 2008.

[3] A National Strategic Plan for Advanced Manufacturing, in: N.S.a.T.C. Executive Office of the President (Ed.) Feb 2012.

[4] M. Drosback, Materials Genome Initiative: Advances and Initiatives, JOM 66(3) (2014).

[5] G.J. Schmitz, U. Prahl, ICMEg–the Integrated Computational Materials Engineering expert group–a new European coordination action, Integrating Materials and Manufacturing Innovation 3(1) (2014) 2.

[6] D. Jarvis, Metallurgy Europe: A Renaissance Programme for 2012-2022, Adv. Phys. 61 (2012) 665-743.

[7] W.F. Maier, K. Stowe, S. Sieg, Combinatorial and high-throughput materials science, Angew. Chem.-Int. Edit. 46(32) (2007) 6016-6067.

[8] R. Potyrailo, K. Rajan, K. Stoewe, I. Takeuchi, B. Chisholm, H. Lam, Combinatorial and High-Throughput Screening of Materials Libraries: Review of State of the Art, ACS Comb. Sci. 13(6) (2011) 579-633.

[9] C.G. Simon, S. Lin-Gibson, Combinatorial and High-Throughput Screening of Biomaterials, Adv. Mater. 23(3) (2011) 369-387.

[10] J.C. Zhao, High-throughput experimental tools for the materials genome initiative, Chin. Sci. Bull. 59(15) (2014) 1652-1661.

[11] M.L. Green, I. Takeuchi, J.R. Hattrick-Simpers, Applications of high throughput (combinatorial) methodologies to electronic, magnetic, optical, and energy-related materials, J. Appl. Phys. 113(23) (2013).

[12] H. Springer, D. Raabe, Rapid alloy prototyping: Compositional and thermo-mechanical high throughput bulk combinatorial design of structural materials based on the example of 30Mn–1.2C–xAl triplex steels, Acta Materialia 60(12) (2012) 4950-4959.

[13] F. Warchomicka, C. Poletti, M. Stockinger, T. Henke, Microstructure Evolution During Hot Deformation of Ti-6Al-4v Double Cone Specimens, International Journal of Material Forming 3 (2010) 215-218.

[14] D.B. Miracle, J.D. Miller, O.N. Senkov, C. Woodward, M.D. Uchic, J. Tiley, Exploration and Development of High Entropy Alloys for Structural Applications, Entropy 16(1) (2014) 494-525.

[15] J.C. Zhao, M.R. Jackson, L.A. Peluso, L.N. Brewer, A diffusion-multiple approach for mapping phase diagrams, hardness, and elastic modulus, Jom-Journal of the Minerals Metals & Materials Society 54(7) (2002) 42-45.

[16] J.C. Zhao, A combinatorial approach for efficient mapping of phase diagrams and properties, J Mater Res 16(6) (2001) 1565-1578.

[17] O.L. Warren, T.J. Wyrobek, Nanomechanical property screening of combinatorial thin-film libraries by nanoindentation, Measurement Science & Technology 16(1) (2005) 100-110.

[18] V.V. Shastry, V.D. Divya, M.A. Azeem, A. Paul, D. Dye, U. Ramamurty, Combining indentation and diffusion couple techniques for combinatorial discovery of high temperature shape memory alloys, Acta Materialia 61(15) (2013) 5735-5742.

[19] S.M. Han, R. Shah, R. Banerjee, G.B. Viswanathan, B.M. Clemens, W.D. Nix, Combinatorial studies of mechanical properties of Ti-Al thin films using nanoindentation, Acta Materialia 53(7) (2005) 2059-2067.

[20] E. Menendez, C. Templier, G. Abrasonis, J.F. Lopez-Barbera, J. Nogues, K. Temst, J. Sort, A combinatorial study of the mechanical and magnetic properties of a gradually nitrided austenitic stainless steel single crystal, Crystengcomm 16(17) (2014) 3515-3520.

[21] C.A. Tweedie, D.G. Anderson, R. Langer, K.J. Van Vliet, Combinatorial material mechanics: High-throughput polymer synthesis and nanomechanical screening, Adv. Mater. 17(21) (2005) 2599-+.

[22] D.L. McDowell, G.B. Olson, Concurrent Design of Hierarchical Materials and Structures, Scientific Modeling and Simulation 15 (2008) 207-240.

[23] C.E. Campbell, G.B. Olson, Systems design of high performance stainless steels I. Conceptual and computational design, Journal of Computer-Aided Materials Design 7 (2001) 145–170.

[24] C.E. Campbell, G.B. Olson, Systems design of high performance stainless steels II. Prototype characterization, Journal of Computer-Aided Materials Design 7 (2001) 171–194.

[25] G.B. Olson, Pathways of Discovery Designing a new material world, Science 228(12) (2000) 933-998.

[26] G.B. Olson, Computational Design of Hierarchically Structured Materials, Science 277(29) (1997) 1237-1242.

[27] G.B. Olson, Systems design of hierarchically structured materials: Advanced steels, Journal of Computer-Aided Materials Design 4 (1997) 143–156.

[28] J.H. Panchal, S.R. Kalidindi, D.L. McDowell, Key computational modeling issues in integrated computational materials engineering, Computer-Aided Design 45(1) (2013) 4-25.

[29] D.L. McDowell, J.H. Panchal, H.-J. Choi, C.C. Seepersad, J.K. Allen, F. Mistree, Integrated Design of Multiscale, Multifunctional Materials and Products, Elsevier2009.

[30] B.L. Adams, S.R. Kalidindi, D. Fullwood, Microstructure Sensitive Design for Performance Optimization, Butterworth-Heinemann2012.

[31] D.T. Fullwood, S.R. Niezgoda, B.L. Adams, S.R. Kalidindi, Microstructure sensitive design for performance optimization, Progress in Materials Science 55(6) (2010) 477-562.

[32] D.L. McDowell, S.R. Kalidindi, The materials innovation ecosystem: A key enabler for the Materials Genome Initiative, MRS Bulletin 41(04) (2016) 326-337.

[33] S.R. Kalidindi, Data science and cyberinfrastructure: critical enablers for accelerated development of hierarchical materials, International Materials Reviews 60(3) (2015) 150-168.

[34] S.R. Kalidindi, Hierarchical Materials Informatics, Butterworth Heinemann2015.

[35] Standard Test Methods and Definitions for Mechanical Testing of Steel Products, ASTM International, 2016.

[36] H.K. Zeytin, C. Kubilay, H. Aydin, Investigation of dual phase transformation of commercial low alloy steels: Effect of holding time at low inter-critical annealing temperatures, Materials Letters 62(17–18) (2008) 2651-2653.

[37] V.H. Baltazar Hernandez, S.K. Panda, M.L. Kuntz, Y. Zhou, Nanoindentation and microstructure analysis of resistance spot welded dual phase steel, Materials Letters 64(2) (2010) 207-210.

[38] X. Xu, S. van der Zwaag, W. Xu, The effect of ferrite–martensite morphology on the scratch and abrasive wear behaviour of a dual phase construction steel, Wear 348–349 (2016) 148-157.

[39] L. Zhang, T. Ohmura, A. Shibata, K. Tsuzaki, Characterization of local deformation behavior of Fe–Ni lenticular martensite by nanoindentation, Materials Science and Engineering: A 527(7–8) (2010) 1869-1874.

[40] R.D.K. Misra, P. Venkatsurya, K.M. Wu, L.P. Karjalainen, Ultrahigh strength martensite–austenite dual-phase steels with ultrafine structure: The response to indentation experiments, Materials Science and Engineering: A 560 (2013) 693-699.

[41] S.S. Ghasemi Banadkouki, E. Fereiduni, Effect of prior austenite carbon partitioning on martensite hardening variation in a low alloy ferrite–martensite dual phase steel, Materials Science and Engineering: A 619 (2014) 129-136.

[42] Y. Mazaheri, A. Kermanpur, A. Najafizadeh, Nanoindentation study of ferrite–martensite dual phase steels developed by a new thermomechanical processing, Materials Science and Engineering: A 639 (2015) 8-14.

[43] G. Cheng, K.S. Choi, X. Hu, X. Sun, Determining individual phase properties in a multi-phase Q&P steel using multi-scale indentation tests, Materials Science and Engineering: A 652 (2016) 384-395.

[44] F.K. Yan, B.B. Zhang, H.T. Wang, N.R. Tao, K. Lu, Nanoindentation characterization of nano-twinned grains in an austenitic stainless steel, Scripta Materialia 112 (2016) 19-22.

[45] V.L. de la Concepción, H.N. Lorusso, H.G. Svoboda, Effect of Carbon Content on Microstructure and Mechanical Properties of Dual Phase Steels, Procedia Materials Science 8 (2015) 1047-1056.

[46] T. Ohmura, K. Tsuzaki, S. Matsuoka, Evaluation of the matrix strength of Fe-0.4 wt% C tempered martensite using nanoindentation techniques, Philosophical Magazine A 82(10) (2002) 1903-1910.

[47] C.C. Tasan, M. Diehl, D. Yan, M. Bechtold, F. Roters, L. Schemmann, C. Zheng, N. Peranio, D. Ponge, M. Koyama, K. Tsuzaki, D. Raabe, An Overview of Dual-Phase Steels: Advances in Microstructure-Oriented Processing and Micromechanically Guided Design, Annual Review of Materials Research 45(1) (2015) 391-431.

[48] K. Mukherjee, S.S. Hazra, M. Militzer, Grain Refinement in Dual-Phase Steels, Metallurgical and Materials Transactions A 40(9) (2009) 2145-2159.

[49] L.E. Samuels, Tempering of Martensite, Metallography, Microstructure, and Analysis 3(1) (2014) 70-90.

[50] W.C. Jeong, Relationship between mechanical properties and microstructure in a 1.5% Mn–0.3% Mo ultra-low carbon steel with bake hardening, Materials Letters 61(11–12) (2007) 2579-2583.

[51] P. Tsipouridis, Mechanical Properties of Dual Phase Steels, Hieronymus2006.

[52] L. Schemmann, S. Zaefferer, D. Raabe, F. Friedel, D. Mattissen, Alloying effects on microstructure formation of dual phase steels, Acta Materialia 95 (2015) 386-398.

[53] S. Pathak, S.R. Kalidindi, Spherical nanoindentation stress–strain curves, Materials Science and Engineering: R: Reports 91 (2015) 1-36.

[54] S.R. Kalidindi, S. Pathak, Determination of the effective zero-point and the extraction of spherical nanoindentation stress-strain curves, Acta Materialia 56(14) (2008) 3523-3532.

[55] S.R. Kalidindi, S.J. Vachhani, Mechanical characterization of grain boundaries using nanoindentation, Current Opinion in Solid State and Materials Science 18(4) (2014) 196-204.

[56] S. Pathak, S.R. Kalidindi, N.A. Mara, Investigations of orientation and length scale effects on micromechanical responses in polycrystalline zirconium using spherical nanoindentation, Scripta Materialia 113 (2016) 241-245.

[57] S. Pathak, J. Shaffer, S.R. Kalidindi, Determination of an effective zero-point and extraction of indentation stress–strain curves without the continuous stiffness measurement signal, Scripta Materialia 60(6) (2009) 439-442.

[58] S. Pathak, D. Stojakovic, S.R. Kalidindi, Measurement of the local mechanical properties in polycrystalline samples using spherical nanoindentation and orientation imaging microscopy, Acta Materialia 57(10) (2009) 3020-3028.

[59] S.J. Vachhani, R.D. Doherty, S.R. Kalidindi, Studies of grain boundary regions in deformed polycrystalline aluminum using spherical nanoindentation, International Journal of Plasticity 81 (2016) 87-101.

[60] S.J. Vachhani, S.R. Kalidindi, Grain-scale measurement of slip resistances in aluminum polycrystals using spherical nanoindentation, Acta Materialia 90 (2015) 27-36.

[61] J.S. Weaver, A. Khosravani, A. Castillo, S.R. Kalidindi, High throughput exploration of process-property linkages in Al-6061 using instrumented spherical microindentation and microstructurally graded samples, Integrating Materials and Manufacturing Innovation 5(1) (2016) 1-20.

[62] S.Y.P. Allain, O. Bouaziz, I. Pushkareva, C.P. Scott, Towards the microstructure design of DP steels: A generic size-sensitive mean-field mechanical model, Materials Science and Engineering: A 637 (2015) 222-234.

[63] S.K. Paul, N. Stanford, T. Hilditch, Effect of martensite volume fraction on low cycle fatigue behaviour of dual phase steels: Experimental and microstructural investigation, Materials Science and Engineering: A 638 (2015) 296-304.

[64] B. Demir, M. Erdoğan, The hardenability of austenite with different alloy content and dispersion in dual-phase steels, Journal of Materials Processing Technology 208(1–3) (2008) 75-84.

[65] N.K. P.D. Sudersanan , S. Aprameyan and Dr.U.N. Kempaiah, The Effect of Carbon Content in Martensite on the Strength of Dual Phase Steel
Bonfring International Journal of Industrial Engineering and Management Science 2(2) (2012) 01-04.

[66] M. Asadi, B.C. De Cooman, H. Palkowski, Influence of martensite volume fraction and cooling rate on the properties of thermomechanically processed dual phase steel, Materials Science and Engineering: A 538 (2012) 42-52.

[67] H. Seyedrezai, Thermo-Mechanical Processing of Dual-Phase Steels and Its Effects on the Work Hardening Behaviour, Mechanical and Materials Engineering, Queen's University, 2014.

[68] A. Gupta, A. Cecen, S. Goyal, A.K. Singh, S.R. Kalidindi, Structure–property linkages using a data science approach: Application to a non-metallic inclusion/steel composite system, Acta Materialia 91 (2015) 239-254.

[69] S.R. Kalidindi, Hierarchical Materials Informatics: Novel Analytics for Materials Data, Elsevier2015.

[70] S. Torquato, Random Heterogeneous Materials, Springer-Verlag, New York, 2002.

[71] S.R. Niezgoda, A.K. Kanjarla, S.R. Kalidindi, Novel microstructure quantification framework for databasing, visualization, and analysis of microstructure data, Integrating Materials and Manufacturing Innovation 2:3 (2013).

[72] S.R. Niezgoda, D.T. Fullwood, S.R. Kalidindi, Delineation of the space of 2-point correlations in a composite material system, Acta Materialia 56(18) (2008) 5285-5292.

[73] B.L. Adams, G. Xiang, S.R. Kalidindi, Finite approximations to the second-order properties closure in single phase polycrystals, Acta Materialia 53(13) (2005) 3563-3577.

[74] S.R. Niezgoda, Y.C. Yabansu, S.R. Kalidindi, Understanding and visualizing microstructure and microstructure variance as a stochastic process, Acta Materialia 59(16) (2011) 6387-6400.

[75] S.R. Kalidindi, S.R. Niezgoda, A.A. Salem, Microstructure informatics using higher-order statistics and efficient data-mining protocols, JOM 63(4) (2011) 34-41.

[76] X. Gao, C.P. Przybyla, B.L. Adams, Methodology for Recovering and Analyzing Two-Point Pair Correlation Functions in Polycrystalline Materials, Metallurgical and Materials Transactions A 37(8) (2006) 2379-2387.

[77] T.A. Mason, B.L. Adams, Use of microstructural statistics in predicting polycrystalline material properties, Metallurgical and Materials Transactions A: Physical Metallurgy and Materials Science 30(4) (1999) 969-979.

[78] S.M. Qidwai, D.M. Turner, S.R. Niezgoda, A.C. Lewis, A.B. Geltmacher, D.J. Rowenhorst, S.R. Kalidindi, Estimating response of polycrystalline materials using sets of weighted statistical volume elements (WSVEs), Acta Materialia 60 (2012) 5284–5299.

[79] D.E.J. Armstrong, A.J. Wilkinson, S.G. Roberts, Measuring anisotropy in Young's modulus of copper using microcantilever testing, Journal of Materials Research 24(11) (2011) 3268-3276.

[80] A. Kunz, S. Pathak, J.R. Greer, Size effects in Al nanopillars: Single crystalline vs. bicrystalline, Acta Materialia 59(11) (2011) 4416-4424.

[81] D. Kiener, C. Motz, M. Rester, M. Jenko, G. Dehm, FIB damage of Cu and possible consequences for miniaturized mechanical tests, Materials Science and Engineering: A 459(1) (2007) 262-272.

[82] D. Kiener, C. Motz, G. Dehm, R. Pippan, Overview on established and novel FIB based miniaturized mechanical testing using in-situ SEM, International Journal of Materials Research 100(8) (2009) 1074-1087.

[83] S. Shim, H. Bei, M.K. Miller, G.M. Pharr, E.P. George, Effects of focused ion beam milling on the compressive behavior of directionally solidified micropillars and the nanoindentation response of an electropolished surface, Acta Materialia 57(2) (2009) 503-510.

[84] J. Mayer, L.A. Giannuzzi, T. Kamino, J. Michael, TEM Sample Preparation and FIB-Induced Damage, MRS Bulletin 32(5) (2011) 400-407.

[85] R. Maaβ, D. Grolimund, S.V. Petegem, M. Willimann, M. Jensen, H.V. Swygenhoven, T. Lehnert, M.A.M. Gijs, C.A. Volkert, E.T. Lilleodden, R. Schwaiger, Defect structure in micropillars using x-ray microdiffraction, Applied Physics Letters 89(15) (2006) 151905.

[86] J.P. McCaffrey, M.W. Phaneuf, L.D. Madsen, Surface damage formation during ion-beam thinning of samples for transmission electron microscopy, Ultramicroscopy 87(3) (2001) 97-104.

[87] H. Bei, S. Shim, G.M. Pharr, E.P. George, Effects of pre-strain on the compressive stress–strain response of Mo-alloy single-crystal micropillars, Acta Materialia 56(17) (2008) 4762-4770.

[88] H. Bei, S. Shim, M.K. Miller, G.M. Pharr, E.P. George, Effects of focused ion beam milling on the nanomechanical behavior of a molybdenum-alloy single crystal, Applied Physics Letters 91(11) (2007) 111915.

[89] S.R. Kalidindi, S. Pathak, Determination of the effective zero-point and the extraction of spherical nanoindentation stress–strain curves, Acta Materialia 56(14) (2008) 3523-3532.

[90] J.S. Weaver, S. Pathak, A. Reichardt, H.T. Vo, S.A. Maloy, P. Hosemann, N.A. Mara, Spherical nanoindentation of proton irradiated 304 stainless steel: A comparison of small scale mechanical test techniques for measuring irradiation hardening, Journal of Nuclear Materials 493 (2017) 368-379.

[91] S. Pathak, J. Michler, K. Wasmer, S.R. Kalidindi, Studying grain boundary regions in polycrystalline materials using spherical nano-indentation and orientation imaging microscopy, Journal of Materials Science 47(2) (2012) 815-823.

[92] J.S. Weaver, M.W. Priddy, D.L. McDowell, S.R. Kalidindi, On capturing the grain-scale elastic and plastic anisotropy of alpha-Ti with spherical nanoindentation and electron back-scattered diffraction, Acta Materialia 117 (2016) 23-34.

[93] J.S. Weaver, S.R. Kalidindi, Mechanical characterization of Ti-6Al-4V titanium alloy at multiple length scales using spherical indentation stress-strain measurements, Materials & Design 111 (2016) 463-472.

[94] A. Khosravani, A. Cecen, S.R. Kalidindi, Development of high throughput assays for establishing process-structure-property linkages in multiphase polycrystalline metals: Application to dual-phase steels, Acta Materialia 123 (2017) 55-69.

[95] J.S. Weaver, A. Khosravani, A. Castillo, S.R. Kalidindi, High throughput exploration of process-property linkages in Al-6061 using instrumented spherical microindentation and microstructurally graded samples, Integrating Materials and Manufacturing Innovation 5(1) (2016) 10.

[96] D.K. Patel, S.R. Kalidindi, Estimating the slip resistance from spherical nanoindentation and orientation measurements in polycrystalline samples of cubic metals, International Journal of Plasticity 92 (2017) 19-30.

[97] D.K. Patel, S.R. Kalidindi, Correlation of spherical nanoindentation stress-strain curves to simple compression stress-strain curves for elastic-plastic isotropic materials using finite element models, Acta Materialia 112 (2016) 295-302.

[98] D.K. Patel, H.F. Al-Harbi, S.R. Kalidindi, Extracting single-crystal elastic constants from polycrystalline samples using spherical nanoindentation and orientation measurements, Acta Materialia 79 (2014) 108-116.

[99] J. Brinell, Mémoire sur les épreaves á bille en acier, II, Cong. Int. Methodes d Essai, A. Wahlberg, Paris (1900) 243.

[100] J.S. Weaver, A. Khosravani, A. Castillo, S.R. Kalidindi, High Throughput Exploration of Process-Property Linkages in Al-6061 using Instrumented Spherical Microindentation and Microstructurally Graded Samples, Integrating Materials and Manufacturing Innovation In press (2016).

[101] ASTM E8 / E8M-15a (2015) Standard Test Methods for Tension Testing of Metallic Materials. ASTM International, West Conshohocken, PA. www.astm.org.

[102] E. Meyer, Untersuchungen über Harteprufung und Härte, Zeitschr, VDI, 1908.

[103] D. Tabor, The hardness of metals, Oxford university press2000.

[104] J.S. Field, M.V. Swain, Determining the mechanical properties of small volumes of material from submicrometer spherical indentations, J Mater Res 10 (1995).

[105] J.S. Field, M.V. Swain, A simple predictive model for spherical indentation, J Mater Res 8 (1993).

[106] H. Hertz, Miscellaneous Papers, MacMillan and Co. Ltd.1896.

[107] W.C. Oliver, G.M. Pharr, Measurement of hardness and elastic modulus by instrumented indentation: Advances in understanding and refinements to methodology, Journal of Materials Research 19(01) (2004) 3-20.

[108] W.C. Oliver, G.M. Pharr, An improved technique for determining hardness and elastic-modulus using load and displacement sensing indentation experiments, J Mater Res 7 (1992).

[109] S. Basu, A. Moseson, M.W. Barsoum, On the determination of spherical nanoindentation stress-strain curves, J Mater Res 21 (2006).

[110] E.G. Herbert, On the measurement of stress-strain curves by spherical indentation, Thin Solid Films 398 (2001).

[111] D. Lorenz, A. Zeckzer, U. Hilpert, P. Grau, H. Johansen, H.S. Leipner, Pop-in effect as homogeneous nucleation of dislocations during nanoindentation, Physical Review B 67(17) (2003) 172101.

[112] T.-H. Ahn, C.-S. Oh, K. Lee, E.P. George, H.N. Han, Relationship between yield point phenomena and the nanoindentation pop-in behavior of steel, Journal of Materials Research 27(1) (2012) 39-44.

[113] S. Pathak, J.L. Riesterer, S.R. Kalidindi, J. Michler, Understanding pop-ins in spherical nanoindentation, Applied Physics Letters 105(16) (2014) 161913.

[114] T. Ohmura, K. Tsuzaki, Analysis of grain boundary effect of bulk polycrystalline materials through nanomechanical characterization, Journal of Physics D: Applied Physics 41(7) (2008) 074015.

[115] W.A. Soer, K.E. Aifantis, J.T.M. De Hosson, Incipient plasticity during nanoindentation at grain boundaries in body-centered cubic metals, Acta Materialia 53(17) (2005) 4665-4676.

[116] M.G. Wang, A.H.W. Ngan, Indentation strain burst phenomenon induced by grain boundaries in niobium, Journal of Materials Research 19(8) (2004) 2478-2486.

[117] K.E. Aifantis, W.A. Soer, J.T.M. De Hosson, J.R. Willis, Interfaces within strain gradient plasticity: Theory and experiments, Acta Materialia 54(19) (2006) 5077-5085.

[118] T.B. Britton, D. Randman, A.J. Wilkinson, Nanoindentation study of slip transfer phenomenon at grain boundaries, Journal of Materials Research 24(3) (2009) 607-615.

[119] W.A. Soer, J.T.M. De Hosson, Detection of grain-boundary resistance to slip transfer using nanoindentation, Materials Letters 59(24) (2005) 3192-3195.

[120] Q. Furnémont, M. Kempf, P.J. Jacques, M. Göken, F. Delannay, On the measurement of the nanohardness of the constitutive phases of TRIP-assisted multiphase steels, Materials Science and Engineering: A 328(1) (2002) 26-32.

[121] T.H. Ahn, C.S. Oh, D.H. Kim, K.H. Oh, H. Bei, E.P. George, H.N. Han, Investigation of strain-induced martensitic transformation in metastable austenite using nanoindentation, Scripta Materialia 63(5) (2010) 540-543.

[122] B.B. He, M.X. Huang, Z.Y. Liang, A.H.W. Ngan, H.W. Luo, J. Shi, W.Q. Cao, H. Dong, Nanoindentation investigation on the mechanical stability of individual austenite grains in a medium-Mn transformation-induced plasticity steel, Scripta Materialia 69(3) (2013) 215-218.

[123] S. Kang, Y.-S. Jung, B.-G. Yoo, J.-i. Jang, Y.-K. Lee, Orientation-dependent indentation modulus and yielding in a high Mn twinning-induced plasticity steel, Materials Science and Engineering: A 532 (2012) 500-504.

[124] R.D.K. Misra, Z. Zhang, Z. Jia, P.K.C.V. Surya, M.C. Somani, L.P. Karjalainen, Nanomechanical insights into the deformation behavior of austenitic alloys with different stacking fault energies and austenitic stability, Materials Science and Engineering: A 528(22) (2011) 6958-6963.

[125] C.A. Schuh, T.G. Nieh, A nanoindentation study of serrated flow in bulk metallic glasses, Acta Materialia 51(1) (2003) 87-99.

[126] C.E. Packard, C.A. Schuh, Initiation of shear bands near a stress concentration in metallic glass, Acta Materialia 55(16) (2007) 5348-5358.

[127] B. Moser, J. Kuebler, H. Meinhard, W. Muster, J. Michler, Observation of Instabilities during Plastic Deformation by in-situ SEM Indentation Experiments, Advanced Engineering Materials 7(5) (2005) 388-392.

[128] J.E. Bradby, J.S. Williams, J. Wong-leung, S.O. Kucheyev, M.V. Swain, P. Munroe, Spherical indentation of compound semiconductors, Philosophical Magazine A 82(10) (2002) 1931-1939.

[129] J.S. Field, M.V. Swain, R.D. Dukino, Determination of fracture toughness from the extra penetration produced by indentation-induced pop-in, Journal of Materials Research 18(6) (2003) 1412-1419.

[130] N. Gane, F. Bowden, Microdeformation of solids, Journal of Applied Physics 39(3) (1968) 1432-1435.

[131] W.W. Gerberich, J.C. Nelson, E.T. Lilleodden, P. Anderson, J.T. Wyrobek, Indentation induced dislocation nucleation: The initial yield point, Acta Materialia 44(9) (1996) 3585-3598.

[132] W. Gerberich, S. Venkataraman, J. Nelson, H. Huang, E. Lilleodden, W. Bonin, Yield Point Phenomena and Dislocation Velocities Underneath Indentations Into BCC Crystals, MRS Online Proceedings Library Archive 356 (1994).

[133] W.W. Gerberich, S.K. Venkataraman, H. Huang, S.E. Harvey, D.L. Kohlstedt, The injection of plasticity by millinewton contacts, Acta Metallurgica et Materialia 43(4) (1995) 1569-1576.

[134] A.E. Giannakopoulos, S. Suresh, Determination of elastoplastic properties by instrumented sharp indentation, Scripta Materialia 40(10) (1999) 1191-1198.

[135] A. Gouldstone, H.J. Koh, K.Y. Zeng, A.E. Giannakopoulos, S. Suresh, Discrete and continuous deformation during nanoindentation of thin films, Acta Materialia 48(9) (2000) 2277-2295.

[136] S. Suresh, T.G. Nieh, B.W. Choi, Nano-indentation of copper thin films on silicon substrates, Scripta Materialia 41(9) (1999) 951-957.

[137] W.D. Nix, H. Gao, Indentation size effects in crystalline materials: A law for strain gradient plasticity, Journal of the Mechanics and Physics of Solids 46(3) (1998) 411-425.

[138] J.G. Swadener, E.P. George, G.M. Pharr, The correlation of the indentation size effect measured with indenters of various shapes, Journal of the Mechanics and Physics of Solids 50(4) (2002) 681-694.

[139] G.M. Pharr, E.G. Herbert, Y. Gao, The Indentation Size Effect: A Critical Examination of Experimental Observations and Mechanistic Interpretations, Annual Review of Materials Research 40(1) (2010) 271-292.

[140] Y. Huang, F. Zhang, K.C. Hwang, W.D. Nix, G.M. Pharr, G. Feng, A model of size effects in nano-indentation, Journal of the Mechanics and Physics of Solids 54(8) (2006) 1668-1686.

[141] S. Pathak, Studying grain boundary regions in polycrystalline materials using spherical nano-indentation and orientation imaging microscopy, J Mater Sci 47 (2012).

[142] S. Pathak, S. Kalidindi, H. Courtland, K. Jepsen, H. Goldman, Improved analysis of bone nano-mechanical properties using a novel nanoindentation technique, Journal of Bone and Mineral Research, AMER SOC BONE & MINERAL RES 2025 M ST, NW, STE 800, WASHINGTON, DC 20036-3309 USA, 2007, pp. S480-S480.

[143] M. Koopman, Z.Z. Fang, X. Wang, P.K. Mehrotra, Properties and Selection of Cemented Carbides, Powder Metallurgy, ASM International, ASM Handbook, 2015, pp. 705–710.

[144] F. Ozturk, Influence of aging treatment on mechanical properties of 6061 aluminum alloy, Mater Des 31 (2010).

[145] J. Buha, Secondary precipitation in an Al-Mg-Si-Cu alloy, Acta Mater 55 (2007).

[146] G.A. Edwards, The precipitation sequence in Al-Mg-Si alloys, Acta Mater 46 (1998).

[147] J.S. Field, M.V. Swain, Determining the mechanical properties of small volumes of material from submicrometer spherical indentations, Journal of Materials Research 10(1) (1995) 101-112.

[148] S. Basu, A. Moseson, M.W. Barsoum, On the determination of spherical nanoindentation stress–strain curves, Journal of Materials Research 21(10) (2006) 2628-2637.

[149] A.C. Fischer-Cripps, A review of analysis methods for sub-micron indentation testing, Vacuum 58 (2000).

[150] W.C. Oliver, G.M. Pharr, An improved technique for determining hardness and elastic modulus using load and displacement sensing indentation experiments, Journal of Materials Research 7(06) (1992) 1564-1583.

[151] B.R. Donohue, A. Ambrus, S.R. Kalidindi, Critical evaluation of the indentation data analyses methods for the extraction of isotropic uniaxial mechanical properties using finite element models, Acta Mater 60 (2012).

[152] D.K. Patel, S.R. Kalidindi, Correlation of spherical nanoindentation stress-strain curves to simple compression stress-strain curves for elastic-plastic isotropic materials using finite element models, Acta Mater 112 (2016).

[153] S.R. Niezgoda, A.K. Kanjarla, S.R. Kalidindi, Novel microstructure quantification framework for databasing, visualization, and analysis of microstructure data, Integrating Materials and Manufacturing Innovation 2(1) (2013) 1-27.

[154] A. Cecen, T. Fast, S.R. Kalidindi, Versatile algorithms for the computation of 2-point spatial correlations in quantifying material structure, Integrating Materials and Manufacturing Innovation 5(1) (2016) 1-15.

[155] D.T. Fullwood, S.R. Kalidindi, S.R. Niezgoda, A. Fast, N. Hampson, Gradient-based microstructure reconstructions from distributions using fast Fourier transforms, Materials Science and Engineering a-Structural Materials Properties Microstructure and Processing 494(1-2) (2008) 68-72.

[156] D.T. Fullwood, S.R. Niezgoda, S.R. Kalidindi, Microstructure reconstructions from 2-point statistics using phase-recovery algorithms, Acta Materialia 56(5) (2008) 942-948.

[157] D.M. Turner, S.R. Kalidindi, Statistical construction of 3-D microstructures from 2-D exemplars collected on oblique sections, Acta Materialia 102 (2016) 136-148.

[158] A. Choudhury, Y.C. Yabansu, S.R. Kalidindi, A. Dennstedt, Quantification and classification of microstructures in ternary eutectic alloys using 2-point spatial correlations and principal component analyses, Acta Materialia 110 (2016) 131-141.

[159] T. Fast, O. Wodo, B. Ganapathysubramanian, S.R. Kalidindi, Microstructure taxonomy based on spatial correlations: Application to microstructure coarsening, Acta Materialia 108 (2016) 176-185.

[160] A. Agrawal, P.D. Deshpande, A. Cecen, G.P. Basavarsu, A.N. Choudhary, S.R. Kalidindi, Exploration of data science techniques to predict fatigue strength of steel from composition and processing parameters, Integrating Materials and Manufacturing Innovation 3(1) (2014) 1-19.

[161] A. Çeçen, T. Fast, E.C. Kumbur, S.R. Kalidindi, A data-driven approach to establishing microstructure–property relationships in porous transport layers of polymer electrolyte fuel cells, Journal of Power Sources 245 (2014) 144-153.

[162] A. Cecen, Y.C. Yabansu, S.R. Kalidindi, A new framework for rotationally invariant two-point spatial correlations in microstructure datasets, Acta Materialia 158 (2018) 53-64.

[163] E. Kröner, Bounds for effective elastic moduli of disordered materials, Journal of the Mechanics and Physics of Solids 25(2) (1977) 137-155.

[164] E. Kröner, Statistical Modelling, in: J. Gittus, J. Zarka (Eds.), Modelling Small Deformations of Polycrystals, Springer Netherlands, Dordrecht, 1986, pp. 229-291.

[165] N.H. Paulson, M.W. Priddy, D.L. McDowell, S.R. Kalidindi, Reduced-order structure-property linkages for polycrystalline microstructures based on 2-point statistics, Acta Materialia 129 (2017) 428-438.

[166] T. Waterschoot, K. Verbeken, B.C. De Cooman, Tempering Kinetics of the Martensitic Phase in DP Steel, ISIJ International 46(1) (2006) 138-146.

[167] A. Hüseyin, K.Z. Havva, K. Ceylan, Effect of Intercritical Annealing Parameters on Dual Phase Behavior of Commercial Low-Alloyed Steels, Journal of Iron and Steel Research, International 17(4) (2010) 73-78.

[168] T. Hilditch, H. Beladi, P. Hodgson, N. Stanford, Role of microstructure in the low cycle fatigue of multi-phase steels, Materials Science and Engineering: A 534 (2012) 288-296.

[169] A. Ramazani, S. Bruehl, T. Gerber, W. Bleck, U. Prahl, Quantification of bake hardening effect in DP600 and TRIP700 steels, Materials & Design 57 (2014) 479-486.

[170] C.F. Kuang, J. Li, S.G. Zhang, J. Wang, H.F. Liu, A.A. Volinsky, Effects of quenching and tempering on the microstructure and bake hardening behavior of ferrite and dual phase steels, Materials Science and Engineering: A 613 (2014) 178-183.

[171] C.-s. Li, Z.-x. Li, Y.-m. Cen, B. Ma, G. Huo, Microstructure and mechanical properties of dual phase strip steel in the overaging process of continuous annealing, Materials Science and Engineering: A 627 (2015) 281-289.

[172] I.B. Timokhina, P.D. Hodgson, E.V. Pereloma, Transmission Electron Microscopy Characterization of the Bake-Hardening Behavior of Transformation-Induced Plasticity and Dual-Phase Steels, Metallurgical and Materials Transactions A 38(10) (2007) 2442-2454.

[173] K. LINDQVIST, Bake hardening effect in advanced high-strength steels, Department of Applied Mechanics, CHALMERS UNIVERSITY OF TECHNOLOGY, 2013.

[174] Y. Cao, J. Ahlström, B. Karlsson, The influence of temperatures and strain rates on the mechanical behavior of dual phase steel in different conditions, Journal of Materials Research and Technology 4(1) (2015) 68-74.

[175] A. Weidner, U.D. Hangen, H. Biermann, Nanoindentation measurements on deformation-induced α'-martensite in a metastable austenitic high-alloy CrMnNi steel, Philosophical Magazine Letters 94(8) (2014) 522-530.

[176] T. Ohmura, K. Tsuzaki, S. Matsuoka, Nanohardness measurement of high-purity Fe–C martensite, Scripta Materialia 45(8) (2001) 889-894.

[177] T. Ohmura, T. Hara, K. Tsuzaki, H. Nakatsu, Y. Tamura, Mechanical characterization of secondary-hardening martensitic steel using nanoindentation, Journal of Materials Research 19(1) (2011) 79-84.

[178] B. Hutchinson, J. Hagström, O. Karlsson, D. Lindell, M. Tornberg, F. Lindberg, M. Thuvander, Microstructures and hardness of as-quenched martensites (0.1–0.5%C), Acta Materialia 59(14) (2011) 5845-5858.

[179] B.B. He, K. Zhu, M.X. Huang, On the nanoindentation behaviour of complex ferritic phases, Philosophical Magazine Letters 94(7) (2014) 439-446.

[180] C.E.I.C. Ohlund, E. Schlangen, S. Erik Offerman, The kinetics of softening and microstructure evolution of martensite in Fe–C–Mn steel during tempering at 300°C, Materials Science and Engineering: A 560 (2013) 351-357.

[181] T. Ohmura, T. Hara, K. Tsuzaki, Evaluation of temper softening behavior of Fe–C binary martensitic steels by nanoindentation, Scripta Materialia 49(12) (2003) 1157-1162.

[182] T. Ohmura, T. Hara, K. Tsuzaki, Relationship between nanohardness and microstructures in high-purity Fe–C as-quenched and quench-tempered martensite, Journal of Materials Research 18(6) (2011) 1465-1470.

[183] B.B. He, M.X. Huang, Revealing the Intrinsic Nanohardness of Lath Martensite in Low Carbon Steel, Metallurgical and Materials Transactions A 46(2) (2015) 688-694.

[184] G. Cheng, K.S. Choi, X. Hu, X. Sun, Determining individual phase properties in a multi-phase Q&P steel using multi-scale indentation tests, Materials Science and Engineering: A 652 (2016) 384-395.

[185] M. Delincé, P.J. Jacques, T. Pardoen, Separation of size-dependent strengthening contributions in fine-grained Dual Phase steels by nanoindentation, Acta Materialia 54(12) (2006) 3395-3404.

[186] P. Haušild, J. Nohava, P. Pilvin, Characterisation of strain-induced martensite in a metastable austenitic stainless steel by nanoindentation, Strain 47 (2011) 129-133.

[187] L. Morsdorf, C.C. Tasan, D. Ponge, D. Raabe, 3D structural and atomic-scale analysis of lath martensite: Effect of the transformation sequence, Acta Materialia 95 (2015) 366-377.

[188] W.N. Sharpe, K.M. Jackson, K.J. Hemker, Z. Xie, Effect of specimen size on Young's modulus and fracture strength of polysilicon, Journal of Microelectromechanical Systems 10(3) (2001) 317-326.

[189] T. Tsuchiya, O. Tabata, J. Sakata, Y. Taga, Specimen size effect on tensile strength of surface-micromachined polycrystalline silicon thin films, Journal of Microelectromechanical Systems 7(1) (1998) 106-113.

[190] T. Namazu, Y. Isono, T. Tanaka, Evaluation of size effect on mechanical properties of single crystal silicon by nanoscale bending test using AFM, Journal of Microelectromechanical Systems 9(4) (2000) 450-459.

[191] O. Kraft, P.A. Gruber, R. Mönig, D. Weygand, Plasticity in Confined Dimensions, Annual Review of Materials Research 40(1) (2010) 293-317.

[192] J.R. Greer, J.T.M. De Hosson, Plasticity in small-sized metallic systems: Intrinsic versus extrinsic size effect, Progress in Materials Science 56(6) (2011) 654-724.

[193] S. Pathak, S.J. Vachhani, K.J. Jepsen, H.M. Goldman, S.R. Kalidindi, Assessment of lamellar level properties in mouse bone utilizing a novel spherical nanoindentation data analysis method, Journal of the Mechanical Behavior of Biomedical Materials 13(Supplement C) (2012) 102-117.

[194] S. Zaefferer, N.-N. Elhami, Theory and application of electron channelling contrast imaging under controlled diffraction conditions, Acta Materialia 75 (2014) 20-50.

[195] I. Gutierrez-Urrutia, S. Zaefferer, D. Raabe, Coupling of Electron Channeling with EBSD: Toward the Quantitative Characterization of Deformation Structures in the SEM, JOM 65(9) (2013) 1229-1236.

[196] I. Gutierrez-Urrutia, S. Zaefferer, D. Raabe, Electron channeling contrast imaging of twins and dislocations in twinning-induced plasticity steels under controlled diffraction conditions in a scanning electron microscope, Scripta Materialia 61(7) (2009) 737-740.

[197] G.E. Lloyd, Atomic number and crystallographic contrast images with the SEM: a review of backscattered electron techniques, Mineralogical Magazine 51(359) (1987) 3-19.

[198] D.J. Prior, P.W. Trimby, U.D. Weber, D.J. Dingley, Orientation contrast imaging of microstructures in rocks using forescatter detectors in the scanning electron microscope, De Gruyter, 1996.

[199] G. Krauss, Martensite in steel: strength and structure, Materials Science and Engineering: A 273 (1999) 40-57.

[200] L. Morsdorf, O. Jeannin, D. Barbier, M. Mitsuhara, D. Raabe, C.C. Tasan, Multiple mechanisms of lath martensite plasticity, Acta Materialia 121 (2016) 202-214.

[201] S. Morito, T. Ohba, A.K. Das, T. Hayashi, M. Yoshida, Effect of Solution Carbon and Retained Austenite Film on Development of Deformation Structure of Low Carbon Lath Martensite, Tetsu-to-Hagane 98(6) (2012) 245-252.

[202] F.H. Samuel, Effect of dual-phase treatment and tempering on the microstructure and mechanical properties of a high strength, low alloy steel, Materials Science and Engineering 75(1) (1985) 51-66.

[203] W.-S. Lee, T.-T. Su, Mechanical properties and microstructural features of AISI 4340 high-strength alloy steel under quenched and tempered conditions, Journal of Materials Processing Technology 87(1) (1999) 198-206.

[204] H. Yoshida, S. Takagi, S. Sakai, S. Morito, T. Ohba, Crystallographic Analysis of Lath Martensite in Ferrite-Martensite Dual Phase Steel Sheet Annealed after Cold-Rolling, ISIJ International 55(10) (2015) 2198-2205.

[205] K. Wakasa, C.M. Wayman, The morphology and crystallography of ferrous lath martensite. Studies of Fe-20%Ni-5%Mn—I. Optical microscopy, Acta Metallurgica 29(6) (1981) 973-990.

[206] G.R. Speich, W.C. Leslie, Tempering of steel, Metallurgical Transactions 3(5) (1972) 1043-1054.

[207] K.A. Taylor, L. Chang, G.B. Olson, G.D.W. Smith, M. Cohen, J.B.V. Sande, Spinodal decomposition during aging of Fe-Ni-C martensites, Metallurgical Transactions A 20(12) (1989) 2717-2737.

[208] L. Morsdorf, D. Raabe, S. Korte-Kerzel, C.U. Scheu, Fundamentals of ferrous low-carbon lath martensite: from the as-quenched, to tempered and deformed states, RWTH Aachen Aachen, Germany, 2017.

[209] A. Shibata, T. Nagoshi, M. Sone, S. Morito, Y. Higo, Evaluation of the block boundary and sub-block boundary strengths of ferrous lath martensite using a micro-bending test, Materials Science and Engineering: A 527(29) (2010) 7538-7544.

[210] T.A. Michalske, J.E. Houston, Dislocation nucleation at nano-scale mechanical contacts, Acta Materialia 46(2) (1998) 391-396.

[211] S. Pathak, D. Stojakovic, R. Doherty, S.R. Kalidindi, Importance of surface preparation on the nano-indentation stress-strain curves measured in metals, Journal of Materials Research 24(3) (2009) 1142-1155.

[212] J.R. Morris, H. Bei, G.M. Pharr, E.P. George, Size Effects and Stochastic Behavior of Nanoindentation Pop In, Physical Review Letters 106(16) (2011) 165502.

[213] P. Sudharshan Phani, K.E. Johanns, E.P. George, G.M. Pharr, A stochastic model for the size dependence of spherical indentation pop-in, Journal of Materials Research 28(19) (2013) 2728-2739.

[214] M. Šebek, P. Horňak, P. Zimovčák, Effect of Annealing on the Microstructure Evolution and Mechanical Properties of Dual Phase Steel, Materials Science Forum 782 (2014) 111-116.

[215] L.T. Robertson, T.B. Hilditch, P.D. Hodgson, The effect of prestrain and bake hardening on the low-cycle fatigue properties of TRIP steel, International Journal of Fatigue 30(4) (2008) 587-594.

[216] C.-f. Kuang, S.-g. Zhang, J. Li, J. Wang, P. Li, Effect of temper rolling on the bake-hardening behavior of low carbon steel, International Journal of Minerals, Metallurgy, and Materials 22(1) (2015) 32-36.

[217] S. Berbenni, V. Favier, X. Lemoine, M. Berveiller, A micromechanical approach to model the bake hardening effect for low carbon steels, Scripta Materialia 51(4) (2004) 303-308.

[218] C.-f. Kuang, J. Wang, J. Li, S.-g. Zhang, H.-f. Liu, H.-l. Yang, Effect of Continuous Annealing on Microstructure and Bake Hardening Behavior of Low Carbon Steel, Journal of Iron and Steel Research, International 22(2) (2015) 163-170.

[219] H. Wang, W. Shi, Y.-l. He, X.-g. Lu, L. Li, Effect of Overaging on Solute Distributions and Bake Hardening Phenomenon in Bake Hardening Steels, Journal of Iron and Steel Research, International 19(1) (2012) 53-59.

[220] L. Durrenberger, X. Lemoine, A. Molinari, Effects of pre-strain and bake-hardening on the crash properties of a top-hat section, Journal of Materials Processing Technology 211(12) (2011) 1937-1947.

[221] S. Kilic, F. Ozturk, T. Sigirtmac, G. Tekin, Effects of Pre-strain and Temperature on Bake Hardening of TWIP900CR Steel, Journal of Iron and Steel Research, International 22(4) (2015) 361-365.

[222] A.A. Vasilyev, H.-C. Lee, N.L. Kuzmin, Nature of strain aging stages in bake hardening steel for automotive application, Materials Science and Engineering: A 485(1–2) (2008) 282-289.

[223] I.B. Timokhina, E.V. Pereloma, S.P. Ringer, R.K. Zheng, P.D. Hodgson, Characterization of the Bake-hardening Behavior of Transformation Induced Plasticity and Dual-phase Steels Using Advanced Analytical Techniques, ISIJ International 50(4) (2010) 574-582.

[224] D.A. Korzekwa, D.K. Matlock, G. Krauss, Dislocation substructure as a function of strain in a dual-phase steel, Metallurgical Transactions A 15(6) (1984) 1221-1228.

[225] M. Calcagnotto, D. Ponge, E. Demir, D. Raabe, Orientation gradients and geometrically necessary dislocations in ultrafine grained dual-phase steels studied by 2D and 3D EBSD, Materials Science and Engineering: A 527(10–11) (2010) 2738-2746.

[226] E.V. Nesterova, S. Bouvier, B. Bacroix, Microstructure evolution and mechanical behavior of a high strength dual-phase steel under monotonic loading, Materials Characterization 100 (2015) 152-162.

[227] A.H. Cottrell, B.A. Bilby, Dislocation Theory of Yielding and Strain Ageing of Iron, Proceedings of the Physical Society. Section A 62(1) (1949) 49.

[228] S. Ghanei, A. Saheb Alam, M. Kashefi, M. Mazinani, Nondestructive characterization of microstructure and mechanical properties of intercritically annealed dual-phase steel by magnetic Barkhausen noise technique, Materials Science and Engineering: A 607 (2014) 253-260.

[229] N. Shukla, S. Das, S. Maji, S.R. Chowdhury, B.K. Show, Effect of Pre-intercritical Annealing Treatments on the Microstructure and Mechanical Properties of 0.33% Carbon Dual-Phase Steel, Journal of Materials Engineering and Performance 24(12) (2015) 4958-4965.

[230] C.-f. Kuang, S.-g. Zhang, J. Li, J. Wang, H.-f. Liu, Effects of pre-strain and baking parameters on the microstructure and bake-hardening behavior of dual-phase steel, International Journal of Minerals, Metallurgy, and Materials 21(8) (2014) 766-771.

[231] M. Asadi, Influence of the Hot Rolling Process on the Mechanical Behavior of Dual Phase Steels, Fakultät für Natur- und Materialwissenschaftlichen, Technischen Universität Clausthal, 2010.

[232] V. Colla, M. Sanctis, A. Dimatteo, G. Lovicu, A. Solina, R. Valentini, Strain Hardening Behavior of Dual-Phase Steels, Metallurgical and Materials Transactions A 40(11) (2009) 2557-2567.

[233] Overview of materials for Low Alloy Steel, MatWeb, http://www.matweb.com/.

[234] C.C. Tasan, J.P.M. Hoefnagels, M. Diehl, D. Yan, F. Roters, D. Raabe, Strain localization and damage in dual phase steels investigated by coupled in-situ deformation experiments and crystal plasticity simulations, International Journal of Plasticity 63 (2014) 198-210.

[235] F. Zhang, A. Ruimi, P.C. Wo, D.P. Field, Morphology and distribution of martensite in dual phase (DP980) steel and its relation to the multiscale mechanical behavior, Materials Science and Engineering: A 659 (2016) 93-103.

[236] B. Hutchinson, L. Ryde, E. Lindh, K. Tagashira, Texture in hot rolled austenite and resulting transformation products, Materials Science and Engineering: A 257(1) (1998) 9-17.

[237] T. Waterschoot, L. Kestens, B.C. De Cooman, Hot rolling texture development in CMnCrSi dual-phase steels, Metallurgical and Materials Transactions A 33(4) (2002) 1091-1102.

[238] S. Zaefferer, J. Ohlert, W. Bleck, A study of microstructure, transformation mechanisms and correlation between microstructure and mechanical properties of a low alloyed TRIP steel, Acta Materialia 52(9) (2004) 2765-2778.

[239] S. Wright, Quantification of recrystallized fraction from orientation imaging scans, National Research Council of Canada, Proceedings of the Twelfth International Conference on Textures of Materials(ICOTOM-12). 1999, pp. 104-109.

[240] A. Agnoli, M. Bernacki, R. Logé, J.-M. Franchet, J. Laigo, N. Bozzolo, Understanding and modeling of gain boundary pinning in Inconel718, 2012.

[241] C. Lim, Length scale effect on the microstructural evolution of copper layers in a roll-bonded copper-niobium composite, in: A. Rollett (Ed.) ProQuest Dissertations Publishing, 2008.

[242] A. Kundu, D.P. Field, Influence of plastic deformation heterogeneity on development of geometrically necessary dislocation density in dual phase steel, Materials Science and Engineering: A 667 (2016) 435-443.

[243] J. Kadkhodapour, S. Schmauder, D. Raabe, S. Ziaei-Rad, U. Weber, M. Calcagnotto, Experimental and numerical study on geometrically necessary dislocations and non-homogeneous mechanical properties of the ferrite phase in dual phase steels, Acta Materialia 59(11) (2011) 4387-4394.

[244] K. Kimura, K. Ushioda, E. Ishimaru, A. Takahashi, Role of hard martensite phase prior to cold-rolling on microstructure evolution after annealing in ferritic stainless steel, Materials Science and Engineering: A 663 (2016) 86-97.

[245] M.F. Ashby, A.L. Greer, Metallic glasses as structural materials, Scripta Materialia 54(3) (2006) 321-326.

[246] J. Schroers, G. Kumar, T.M. Hodges, S. Chan, T.R. Kyriakides, Bulk metallic glasses for biomedical applications, JOM 61(9) (2009) 21-29.

[247] W.H. Wang, Bulk Metallic Glasses with Functional Physical Properties, Advanced Materials 21(45) (2009) 4524-4544.

[248] M. Telford, The case for bulk metallic glass, Materials Today 7(3) (2004) 36-43.

[249] A. Inoue, A. Takeuchi, Recent development and application products of bulk glassy alloys, Acta Materialia 59(6) (2011) 2243-2267.

[250] G. Xie, F. Qin, S. Zhu, A. Inoue, Ni-free Ti-based bulk metallic glass with potential for biomedical applications produced by spark plasma sintering, Intermetallics 29 (2012) 99-103.

[251] C.A. Schuh, T.C. Hufnagel, U. Ramamurty, Mechanical behavior of amorphous alloys, Acta Materialia 55(12) (2007) 4067-4109.

[252] Z.L. M. Q. Jiang, J. X. Meng & L. H. Dai, Energy dissipation in fracture of bulk metallic glasses via inherent competition between local softening and quasi-cleavage, Philosophical Magazine 88(3) (2008) 407-426.

[253] M.Q.J. Y. Chen, Y.J. Wei & L.H. Dail, Failure criterion for metallic glasses, Philosophical Magazine 91(36) (2011) 4536-4554.

[254] W.L. Johnson, K. Samwer, A Universal Criterion for Plastic Yielding of Metallic Glasses with a $(T/{T}_{g}{)}^{2/3}$ Temperature Dependence, Physical Review Letters 95(19) (2005) 195501.

[255] B. Yang, C.T. Liu, T.G. Nieh, Unified equation for the strength of bulk metallic glasses, Applied Physics Letters 88(22) (2006) 221911.

[256] D.L. Henann, L. Anand, Fracture of metallic glasses at notches: Effects of notch-root radius and the ratio of the elastic shear modulus to the bulk modulus on toughness, Acta Materialia 57(20) (2009) 6057-6074.

[257] Z. Han, W.F. Wu, Y. Li, Y.J. Wei, H.J. Gao, An instability index of shear band for plasticity in metallic glasses, Acta Materialia 57(5) (2009) 1367-1372.

[258] A. Furukawa, H. Tanaka, Inhomogeneous flow and fracture of glassy materials, Nat Mater 8(7) (2009) 601-609.

[259] F.S. Tsai-Wei Wu, The relation between enbrittlement and structural relaxation of an amorphous metal, Philosophical Magazine Part B 61(4) (1990) 739-750.

[260] F. Spaepen, A microscopic mechanism for steady state inhomogeneous flow in metallic glasses, Acta Metallurgica 25(4) (1977) 407-415.

[261] A.C. Lund, C.A. Schuh, Yield surface of a simulated metallic glass, Acta Materialia 51(18) (2003) 5399-5411.

[262] K.M. D. Srolovitz, V. Vitek & T. Egami, Structural defects in amorphous solids Statistical analysis of a computer model, Philosophical Magazine A 44(4) (1981) 847-866.

[263] Y. Wu, Y. Xiao, G. Chen, C.T. Liu, Z. Lu, Bulk Metallic Glass Composites with Transformation-Mediated Work-Hardening and Ductility, Advanced Materials 22(25) (2010) 2770-2773.

[264] L.F. Liu, L.H. Dai, Y.L. Bai, B.C. Wei, J. Eckert, Behavior of multiple shear bands in Zr-based bulk metallic glass, Materials Chemistry and Physics 93(1) (2005) 174-177.

[265] W.H. Jiang, G.J. Fan, F.X. Liu, G.Y. Wang, H. Choo, P.K. Liaw, Spatiotemporally inhomogeneous plastic flow of a bulk-metallic glass, International Journal of Plasticity 24(1) (2008) 1-16.

[266] N.A.M. A. V. Sergueeva, J. D. Kuntz, E. J. Lavernia & A. K. Mukherjee, Shear band formation and ductility in bulk metallic glass, Philosophical Magazine 85(23) (2005) 2671-2687.

[267] D. Srolovitz, V. Vitek, T. Egami, An atomistic study of deformation of amorphous metals, Acta Metallurgica 31(2) (1983) 335-352.

[268] M.L. Falk, Molecular-dynamics study of ductile and brittle fracture in model noncrystalline solids, Physical Review B 60(10) (1999) 7062-7070.

[269] M. Chen, Mechanical Behavior of Metallic Glasses: Microscopic Understanding of Strength and Ductility, Annual Review of Materials Research 38(1) (2008) 445-469.

[270] J.C.M. Li, Dislocations in amorphous metals, Metallurgical Transactions A 16(12) (1985) 2227-2230.

[271] J. Das, M.B. Tang, K.B. Kim, R. Theissmann, F. Baier, W.H. Wang, J. Eckert, ``Work-Hardenable'' Ductile Bulk Metallic Glass, Physical Review Letters 94(20) (2005) 205501.

[272] W. Wright, nbsp, J, R. Saha, W. Nix, nbsp, D, Deformation Mechanisms of the Zr_{<B>40</B>}Ti_{<B>14</B>}Ni_{<B>10</B>}Cu_{<B>12</B>}Be_{<B>24</B>} Bulk Metallic Glass, MATERIALS TRANSACTIONS 42(4) (2001) 642-649.

[273] J. Schroers, W.L. Johnson, Ductile Bulk Metallic Glass, Physical Review Letters 93(25) (2004) 255506.

[274] D.C. Hofmann, J.-Y. Suh, A. Wiest, M.-L. Lind, M.D. Demetriou, W.L. Johnson, Development of tough, low-density titanium-based bulk metallic glass matrix composites with tensile ductility, Proceedings of the National Academy of Sciences 105(51) (2008) 20136-20140.

[275] A.I.H. Committee, Metals Handbook: Vol. 2, Properties and selection–nonferrous alloys and pure metals, New York: ASM International Handbook, 1990.

[276] M. Zink, K. Samwer, W.L. Johnson, S.G. Mayr, Plastic deformation of metallic glasses: Size of shear transformation zones from molecular dynamics simulations, Physical Review B 73(17) (2006) 172203.

[277] C.A. Schuh, A.C. Lund, Application of nucleation theory to the rate dependence of incipient plasticity during nanoindentation, Journal of Materials Research 19(7) (2011) 2152-2158.

[278] J.H. Perepezko, S.D. Imhoff, M.-W. Chen, J.-Q. Wang, S. Gonzalez, Nucleation of shear bands in amorphous alloys, Proceedings of the National Academy of Sciences 111(11) (2014) 3938-3942.

[279] D.E. Polk, D. Turnbull, Flow of melt and glass forms of metallic alloys, Acta Metallurgica 20(4) (1972) 493-498.

[280] C.A. Schuh, A.S. Argon, T.G. Nieh, J. Wadsworth, The transition from localized to homogeneous plasticity during nanoindentation of an amorphous metal, Philosophical Magazine 83(22) (2003) 2585-2597.

[281] A. Puthucode, R. Banerjee, S. Vadlakonda, R. Mirshams, M.J. Kaufman, Incipient Plasticity and Shear Band Formation in Bulk Metallic Glass Studied Using Indentation, Metallurgical and Materials Transactions A 39(7) (2008) 1552-1559.

[282] Y.M. Lu, B.A. Sun, L.Z. Zhao, W.H. Wang, M.X. Pan, C.T. Liu, Y. Yang, Shear-banding Induced Indentation Size Effect in Metallic Glasses, 6 (2016) 28523.

[283] Y.I. Golovin, V.I. Ivolgin, V.A. Khonik, K. Kitagawa, A.I. Tyurin, Serrated plastic flow during nanoindentation of a bulk metallic glass, Scripta Materialia 45(8) (2001) 947-952.

[284] L.-H. Dai, L.-F. Liu, M. Yan, B.-C. Wei, J. Eckert, Serrated Plastic Flow in a Zr-based Bulk Metallic Glass During Nanoindentation, Chinese Physics Letters 21(8) (2004) 1593.

[285] A.S. Argon, Plastic deformation in metallic glasses, Acta Metallurgica 27(1) (1979) 47-58.

[286] M.L. Falk, J.S. Langer, Dynamics of viscoplastic deformation in amorphous solids, Physical Review E 57(6) (1998) 7192-7205.

[287] M. Heggen, F. Spaepen, M. Feuerbacher, Creation and annihilation of free volume during homogeneous flow of a metallic glass, Journal of Applied Physics 97(3) (2004) 033506.

[288] M.H. Cohen, D. Turnbull, Molecular Transport in Liquids and Glasses, The Journal of Chemical Physics 31(5) (1959) 1164-1169.

[289] L.T.S. A. S. Argon, Analysis of plastic flow in an amorphous soap bubble raft by the use of an inter-bubble potential, Philosophical Magazine A 46(2) (1982) 275-294.

[290] S.G. Mayr, Activation Energy of Shear Transformation Zones: A Key for Understanding Rheology of Glasses and Liquids, Physical Review Letters 97(19) (2006) 195501.

[291] D. Pan, A. Inoue, T. Sakurai, M.W. Chen, Experimental characterization of shear transformation zones for plastic flow of bulk metallic glasses, Proceedings of the National Academy of Sciences 105(39) (2008) 14769-14772.

[292] P. Schall, D.A. Weitz, F. Spaepen, Structural Rearrangements That Govern Flow in Colloidal Glasses, Science 318(5858) (2007) 1895-1899.

[293] S. Kobayashi, K. Maeda, S. Takeuchi, Computer simulation of deformation of amorphous Cu57Zr43, Acta Metallurgica 28(12) (1980) 1641-1652.

[294] J. Rottler, M.O. Robbins, Shear yielding of amorphous glassy solids: Effect of temperature and strain rate, Physical Review E 68(1) (2003) 011507.

[295] T. Tomida, T. Egami, Molecular-dynamics study of structural anisotropy and anelasticity in metallic glasses, Physical Review B 48(5) (1993) 3048-3057.

[296] C. Suryanarayana, A. Inoue, Bulk metallic glasses, CRC press2017.

[297] W. Li, H. Bei, Y. Tong, W. Dmowski, Y.F. Gao, Structural heterogeneity induced plasticity in bulk metallic glasses: From well-relaxed fragile glass to metal-like behavior, Applied Physics Letters 103(17) (2013) 171910.

[298] S. Pauly, S. Gorantla, G. Wang, U. Kühn, J. Eckert, Transformation-mediated ductility in CuZr-based bulk metallic glasses, Nat Mater 9(6) (2010) 473-477.

[299] B. Sarac, Y.P. Ivanov, A. Chuvilin, T. Schöberl, M. Stoica, Z. Zhang, J. Eckert, Origin of large plasticity and multiscale effects in iron-based metallic glasses, Nature Communications 9(1) (2018) 1333.

[300] C.M. Pekor, P. Kisa, I. Nettleship, Effect of Polyethylene Glycol on the Microstructure of Freeze-Cast Alumina, Journal of the American Ceramic Society 91(10) (2008) 3185-3190.

[301] M. Flemings, T. Bower, T. Kattamis, H. Brody, EFFECTS OF SOLIDIFICATION VARIABLES ON INGOT STRUCTURE, MASSACHUSETTS INST OF TECH CAMBRIDGE CASTING AND SOLIDIFICATION SECTION, 1966.

[302] G. Nereo, M. Flemings, Effects of Solidification Variables on the Structure of Aluminum Base Ingots, MASSACHUSETTS INST OF TECH CAMBRIDGE DEPT OF METALLURGY AND MATERIALS SCIENCE, 1966.

[303] D.H. Kirkwood, A simple model for dendrite arm coarsening during solidification, Materials Science and Engineering 73 (1985) L1-L4.

[304] M. Kahlweit, On the ageing of dendrites, Scripta Metallurgica 2(5) (1968) 251-254.

[305] T.F. Bower, Measurement of solute redistribution in dendritic solidification, Transactions of Metallurgical Society of AIME 236 (1966) 624-634.

[306] P. Steinmetz, Y.C. Yabansu, J. Hötzer, M. Jainta, B. Nestler, S.R. Kalidindi, Analytics for microstructure datasets produced by phase-field simulations, Acta Materialia 103 (2016) 192-203.

[307] S.R. Kalidindi, J.A. Gomberg, Z.T. Trautt, C.A. Becker, Application of data science tools to quantify and distinguish between structures and models in molecular dynamics datasets, Nanotechnology 26(34) (2015) 344006.

[308] A. CeCen, T. Fast, E.C. Kumbur, S.R. Kalidindi, A Data-driven Approach to Establishing Microstructure-Property Relationships in Porous Transport Layers of Polymer Electrolyte Fuel Cells, Journal of Power Sources 245 (2014) 144-153.

[309] X. Dong, D.L. McDowell, S.R. Kalidindi, K.I. Jacob, Dependence of mechanical properties on crystal orientation of semi-crystalline polyethylene structures, Polymer 55(16) (2014) 4248-4257.

[310] M.T. David, R.N. Stephen, R.K. Surya, Efficient computation of the angularly resolved chord length distributions and lineal path functions in large microstructure datasets, Modelling and Simulation in Materials Science and Engineering 24(7) (2016) 075002.

[311] K.V. Mardia, J.T. Kent, J.M. Bibby, Multivariate analysis, (1980).

[312] I.K. Fodor, A survey of dimension reduction techniques, Technical Report UCRL-ID-148494, Lawrence Livermore National Laboratory, 2002.

[313] A. Hyvärinen, Survey on independent component analysis, (1999).

[314] J.R. Quinlan, Learning with continuous classes, 5th Australian joint conference on artificial intelligence, Singapore, 1992, pp. 343-348.

[315] M.A. Hearst, S.T. Dumais, E. Osman, J. Platt, B. Scholkopf, Support vector machines, IEEE Intelligent Systems and their Applications 13(4) (1998) 18-28.

[316] S.R. Kalidindi, A.J. Medford, D.L. McDowell, Vision for Data and Informatics in the Future Materials Innovation Ecosystem, JOM (2016) 1-12.

[317] S.R. Kalidindi, M.D. Graef, Materials Data Science: Current Status and Future Outlook, Annual Review of Materials Research 45(1) (2015) 171-193.